New Demodulation Techniques

for Gearbox Bearing Fault Detection

By:

Shazali Osman

A thesis

presented to the Lakehead University

in fulfillment of the

thesis requirement for the degree of

Doctor of Philosophy

in

Engineering

Lakehead University, Thunder Bay, Ontario, Canada

Abstract

Nowadays, modern rotating machinery industries such as automotive, aerospace, turbo machinery, chemical plants, and power generation stations are rapidly increasing in complexity and in their everyday operations, which demand their systems to operate at higher reliability, extreme safety, and with lower production and maintenance costs. Therefore, accurate fault diagnosis of machine failure is vital to the operation of the related industries. The majority of machine imperfections has been related to gearbox faults (e.g., gears, shafts and bearings), which are subject to damage modes such as fatigue, impacts, and overloading. Faults not detected in time can result in severe damage to machinery, catastrophic injuries, and substantial financial losses. On the other hand, if a fault is detected in its early stages, corrective and preventive action can be taken to avoid any significant machine failure. Vibration monitoring, a method that is widely used to determine the condition of various mechanical systems, will be applied in this work. In data acquisition, a transducer is attached to the structure under investigation and the vibration signal is recorded. This signal is then processed to extract representative features for fault detection. Signal processing techniques are therefore required to extract representative features to assess the health condition of gearbox components. However, in practice, the theoretical frequencies and characteristic features of gearbox faults may be modulated and masked by parasitical frequencies due to numerous noisy vibrations, as well as by the complexity of the transmission mechanics. To solve the related problems, the objective of this research work is to propose new signal processing technologies to evaluate gearbox health conditions. This work will focus on fixed-axis gearboxes, in which all gears are designed to rotate around their perspective fixed centers. Firstly, an enhanced morphological filtering (eM) technique is proposed to improve signal-to-noise ratio. Secondly, under controlled operating conditions, an integrated Hilbert Huang transform (iHT) method is suggested for bearing fault detection. Thirdly, a leakage-free resonance sparse decomposition (LRSD)-based technique is developed for advanced vibration signal analysis to eliminate random noise and to recognize characteristic features for bearing in gearboxes health conditions. The effectiveness of the proposed techniques is verified by a series of experimental tests corresponding to different bearing and gearbox conditions.

Dedications

This thesis is dedicated to my wife, son, daughter, family, and friends.

Acknowledgements

I would like to express my greatest gratitude to my supervisor, Professor Wilson Wang, for his continuous support, enthusiastic supervision, and patient guidance. His always-cheerful conversations, friendly behavior, and unique way of making his students realize their hidden research talents are extraordinary. I heartily acknowledge his constant encouragement and genuine efforts to explore possible funding routes for the continuation of my research studies. I cannot imagine having any better advisors for my doctoral study in terms of his knowledge, perceptiveness, and encouragement.

I am also grateful to my PhD committee members, the external examiner Professor Chris Mechefske, Professor Abdelhamid Tayebi, Professor Ayan Sadhu, and Professor Hao Bai for their instructive guidance and assistance.

Many thanks to my friends and many others for their friendship and help.

I wish to extend my utmost thanks to my relatives in Sudan, especially my parents and parents-in-law for their love and continuous support.

Finally, I am forever indebted to my beloved wife Mozn Abdalla, to my son Muhammad, and to my daughter Nour, for their unconditional and continuous encouragement, support and love, which has made this extensive research task a pleasant journey.

Table of Contents

List of Figures

List of Tables

List of Acronyms

Acronym	Original Phrase
DP	d'Agostino-Pearson Normality Test
EMD	Empirical Mode Decomposition
EEMD	Ensemble EMD
MED	Minimum Entropy Deconvolution
eM	Enhanced Morphological Filter
FAM	Fuzzy Associative Memory
FT	Fourier Transform
HT	Hilbert transform
HHT	Hilbert Haung Transform
HFRT	High Frequency Resonance Technique
IMF	Intrinsic Mode Function
iHT	Integrated Hilbert Haung Transform
f_{IR}	Inner Race Defect Characteristic Frequency
JB	Jarque-Bera Goodness-of-fit Test
LRSD	Leakage-free Resonance Sparse Decomposition
MI	Mutual information
MCA	Morphological Components Analysis
NHHT	Normalized Hilbert Haung Transform
f_{OR}	Outer Race Defect Characteristic Frequency
RE	Renyi Entropy
RSD	Resonance Sparse Decomposition
RE	Renyi Entropy
RSD	Resonance Sparse Decomposition

f_{BD}	Rolling Element (ball) Defect Characteristic Frequency
f_{BD}	Rolling Element (ball) Defect Characteristic Frequency
SALSA	Split Augmented Lagrangian Shrinkage Algorithm
SE	Structural Element
TQWT	Tunable Q factor WT
TSA	Time Synchronous Averaging
STFT	Short Time FT
WDP	Weighted d'Agostino-Pearson Normality Test
WT	Wavelet Transform
WVD	Wigner-Ville distribution
VMD	Variational Mode Decomposition

Chapter 1

Introduction

1.1 Overview

Rotary machines are widely used in various types of modern industrial applications, such as automobile, aerospace, chemical plants, and power stations in their everyday operations. Gearboxes are commonly used in rotary machinery to scale torque and angular velocity. A typical gearbox includes gears, shafts, and bearings, as shown in Figure 1.1.
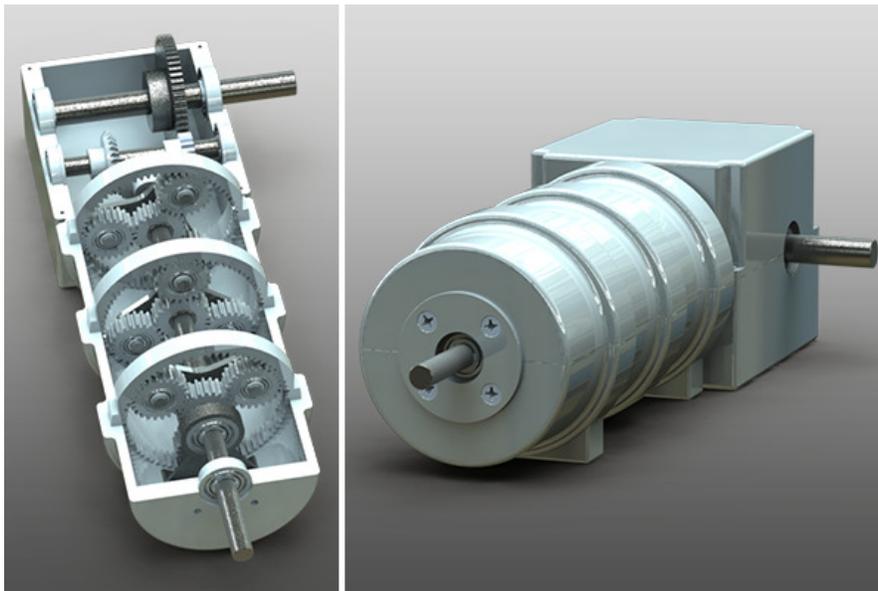
Figure 1.1. Machinery gearbox [1].

Presently, fault detection has become an important problem associated with rotating machinery. In rotating machinery, the main defects could be related to transmission systems, especially gearboxes [2,3]. Diagnosis theory makes it possible to detect and isolate faults at the early stages so as to prevent machinery performance degradation, operation malfunction, or even catastrophic failures. In recent years, the increase in computing power has made it possible to develop and implement advanced diagnosis systems operating online or in real-time.

1.2 Gear System Fault Detection

There are several types of gearboxes. The simplest form of gear train is a fixed center parallel shaft gearbox using spur or helical gears [4]. In spur gears, tooth flanks run parallel to the shaft axes, and do not impart any axial force on the gear. A given gear tooth meshes with a mating tooth in another gear periodically. This leads to varying stresses and deflections in the teeth, which result in gear vibrations. Gear tooth failures are generally classified as "distributed" and "localized" faults. Distributed faults such as adhesive or abrasive defects are mainly caused by inadequate lubrication. In contrast, localized gear surface failures are generally caused by excessive tooth stress and fatigue that can cause pitting, cracking, and scoring. Although both gear failure modes can deteriorate transmission accuracy and increase noise and vibration in the gearbox, from a gear health condition monitoring perspective, more interest focuses on initial localized fault detection because most distributed defects are generally initiated with a localized fault [4,6]. Hence, this research work will focus on incipient localized fault detection.

Gearbox health condition monitoring can be undertaken based on the analysis of different information carriers such as temperature, lubrication, or vibration [6,7]. Thermal analysis is based on the measurement of overheating of the gearbox housing. The temperature information can be used to study the temperature gradient of the gearbox components [8]; however, thermal analysis is not appropriate for identifying incipient defects in a gear system. In addition, thermal analysis is sensitive to the environmental effects that may cause temperature fluctuation.

Lubricant-based monitoring focuses on the analysis of debris in the lubricant, which is generated by gear system defects. It consists of several steps such as oil sampling, analytical tests, and data interpretation. Although oil debris analysis could be efficient to detect defects such as distributed defects (e.g., severe wear), it requires not only a closed loop oil supply system, but also specific expert knowledge to process and explain the results.

Each rotating component in the gearbox generates vibrations, even though it is in its normal/healthy condition. Vibration analysis is based on the comparison of a baseline vibration signature; any subsequent change in its operating parameters or material condition will be reflected by a change in its vibration signature. Vibration diagnostics are usually focused on the extraction of features from a signal and associates these features with the health condition of the

gearbox. This concept is well-established both in theory and in practice [7,8]. A Vibration signature is sensitive and can be used as an early predictor of a developing fault. Vibration-based analysis is non-intrusive and cost-effective, and can be employed for the diagnosis of both localized or distributed defects [9], which make it more attractive for early defect detection [10]. It is for these reasons that vibration analysis is widely employed in the industry and it is also used in this work.

1) Gear fault detection techniques

Defects in gear systems can be classified into distributed and localized faults. A gear that suffers from distributed damage experiences two types of wear: 1) adhesive wear caused by metal transfer from one tooth to its mating tooth by welding action; and 2) abrasive wear in the meshing area caused by abrasion. Localized gear faults can be classified according to the type of defect: 1) breakage of tooth is due to reasons such as bending fatigue (Figure 1.2), impact or overloading on the gear tooth; 2) scoring (Figure 1.3) is induced by metal-to-metal contact, which is caused by lubrication film breakdown due to inappropriate lubrication, overloading, or localized high temperature on mating surfaces; and 3) pitting (Figure 1.4) occurs when the contact stress exceeds the fatigue endurance limit, which results in a small spalls that fall off the tooth surface [11,12]. Gear fault detection is used to analyze the vibration data using appropriate methods to compare the extracted features to those of known faults [10,13].

Figure 1.2. Broken gear tooth defect [15].

3

Figure 1.3. Sever scoring defect in gears [16].
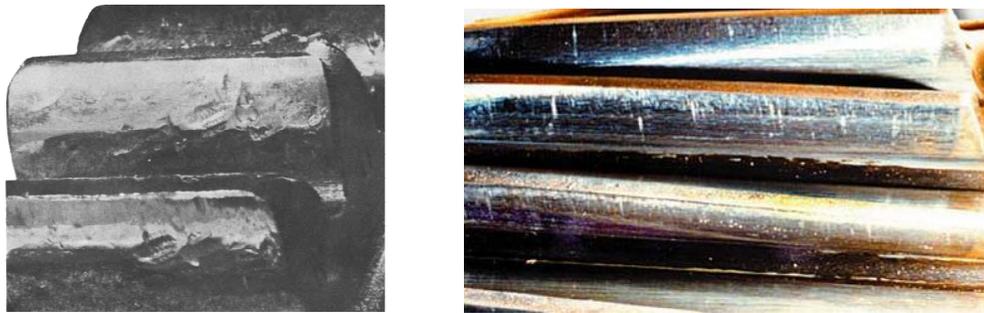
Figure 1.4. Severe pitting defect in gears [17].

Vibration-based gear fault detection techniques can be established in the time, the frequency, or the time-frequency domains [18,19], as briefly discussed as follows.

2) Time-domain techniques

In time-domain analysis, common diagnostic indicators include the probability density distribution analysis, signal averaging, and demodulation methods [19,20]. Most of these indicators analyze the differences in vibration amplitude and/or phase due to the damage of the gear system. Another approach used in gearbox fault detection is the synchronous time-domain averaging (TSA) filter [11,21]; the vibration signal of a specific gear can be recognized. The signal average shows the pattern of the gear tooth meshing vibration, including a perturbation produced by the faulty gear tooth [9]. A simple visual inspection of the gear vibration average may sometimes reveal some pronounced gear tooth faults [20]. However, these time-domain fault features are not always noticeable, particularly if the fault is still in its early stage due to modulation of other strong vibration signals [20-23]. These aforementioned limitations could be partly overcome by using frequency domain analysis.

3) Frequency domain techniques

The vibration generated by a gear system usually contains a number of frequencies that are specific to thr gear meshing frequency (MF): $f_M = f_r z$, and its harmonics, where z is the number of teeth on the gear of interest, and f_r is the rotational speed of the gears. The most important components in gear vibration spectra are the gear MF and its harmonics (Figure 1.5(a)). along with the modulation sidebands (Figure 1.5(b)). Amplitude modulations are present for reasons such as shaft eccentricity, bending, or misalignment. In general, if a gear tooth is damaged, both amplitude and frequency modulations are present. The increase in the number and amplitude of sidebands often indicates faulty conditions. On the other hand, the appearance of sidebands around the gear mesh harmonics can also be for reasons such as bearing defect, accompanied by movement of the gear shaft. Sidebands are usually caused by amplitude or frequency modulation of a vibration signal. Pronounced localized gear failures cause localized amplitude distortion of the vibration signal, and their effects are regarded as low-level sidebands spaced at the rotational frequency of the defective gear, extending across a wide frequency range. In contrast, distributed faults, such as misalignment and eccentricity, tend to result in higher-level sidebands that are more closely grouped around the gear MF and its harmonics. Low frequency harmonics of the shaft speed are mainly caused by additive impulses [12], whereas frequency harmonics of other components stem from errors induced during the gear's machining process [6,10].
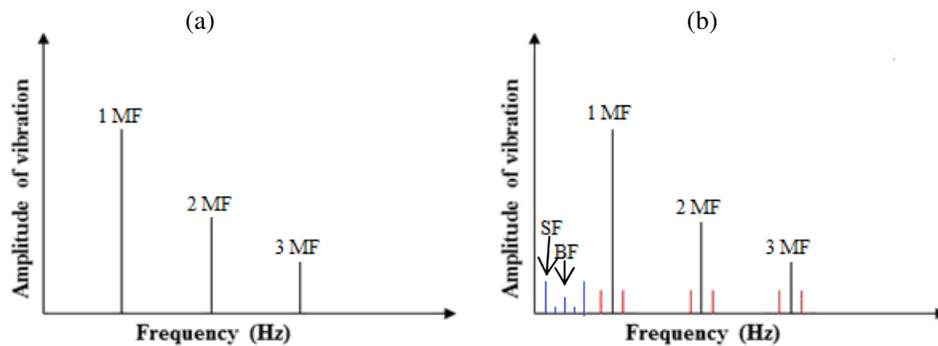
Figure 1.5. Gear vibration spectra at (a) the tooth-meshing frequency and its harmonics (a) and (b) the tooth-meshing frequency, its harmonics, shaft frequency (SF), bearing characteristic frequency (BF), and sidebands of shaft frequency [25].

Another common frequency domain technique is the envelope analysis, which is a method of extracting the periodic excitation due to the presence of a defect [24]. However, the

successful application of envelope analysis requires knowledge and experience in locating the carrier frequencies. Although the kurtosis value can be used to assist identifying a suitable carrier frequency [26], the machine being monitored might not contain clear carrier frequencies. Moreover, envelope analysis is not suitable for detecting more severe gearbox damage, which will exhibit a more random dynamic response to impacts [3,6]. When many spectral maps are averaged, modulation sidebands may dominate the envelope spectrum average instead of the related impact frequencies [8,27]. Furthermore, FT averages is used , the resulted spectrum analysis will lose the non-stationary characteristics that can be related to defect signatures. Another major limitation of frequency domain analysis is its inability to process non-stationary waveform signals, which are common when gear faults occur. The time-frequency analysis could provide an alternative for analyzing non-stationary and non-linear signals.

4) Time-frequency domain techniques

Time-frequency techniques analyze signals in both time and frequency domain to extract information for identifying time-dependent variations of frequency components within the signal [28]. The wavelet transform (WT) is one of the time-frequency methods for detecting faults in gears by detecting sudden changes in non-stationary signals [28,29]. The advantage of the continuous WT is that it has a constant relative resolution: good time resolution at high frequencies, and good frequency resolution at low frequencies [30,31]. Another well accepted time-frequency method for detecting gear faults is ensemble empirical mode decomposition (EMD) [32], which decomposes the vibration signal followed by the Hilbert transform (HT), resulting in a diagnostic conclusion in the Hilbert-Huang transform (HHT) spectrum analysis [33].

1.3 Shaft Defect Detection

1) Shaft defect

A shaft is used to transmit power and motion, and to support rotating machinery elements such as gears, impellers, and pulleys. Undetected shaft failure can affect transmission accuracy and production rates, or even cause safety concerns [5,8]. Imbalance and misalignment are the two common shaft defects. Imbalance is an eccentric distribution of rotor mass (Figure1.6). When an imbalanced rotor rotates, the resulting rotating centrifugal force produces additional force on

bearings at rotor frequency [35]. Another common shaft failure is associated with shaft misalignment, which occurs when the shaft of the driven machine and the driving shaft are not coaxial misalignment [36] as illustrated in Figure 1.7. The main cause of the shaft misalignment is due to connected bearings on the same shaft, as ideal alignment is not guaranteed along the shaft especially if hard coupling mechanisms are used to connect multiple shafts.
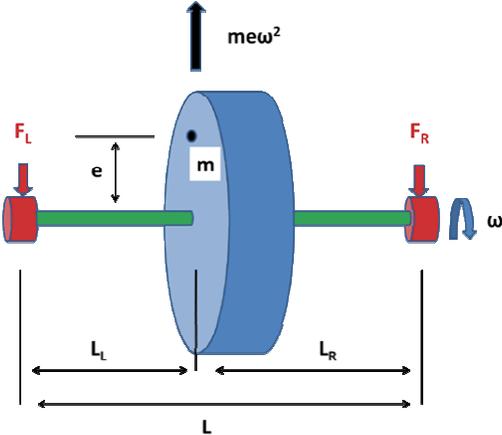
Figure 1.6. Shaft imbalanced forces defect [34].
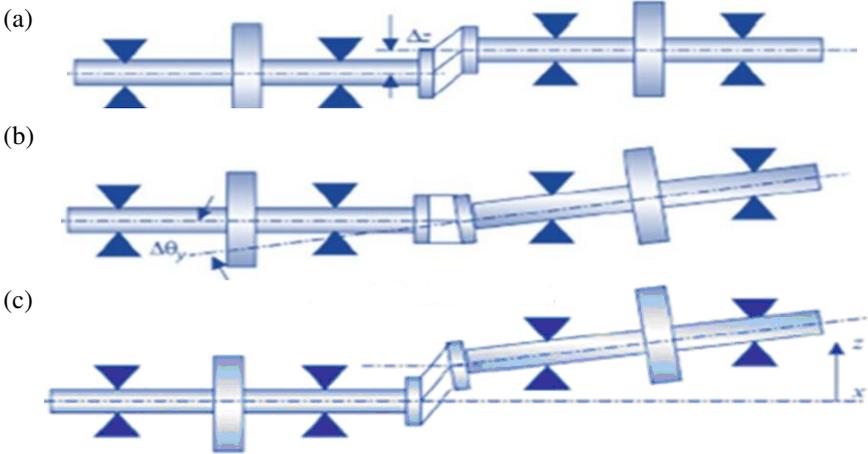
Figure 1.7. Shaft misalignment defect: (a) parallel; (b) angular; (c) combination [37].

2) Time-domain techniques

The impulsive events associated with bearings and gears, the appearance of modulations (which are common in faulty gears and shafts), and the truncation of amplitudes is present are all instances when the time-domain waveform shape or pattern may help lend strong direction to

7

continued analysis efforts [38]. Transient events are also clearly displayed, making time-domain the method of choice for the study of theses conditions [35,39]. Several specific time-domain techniques are of particular importance; for example, crest factor and kurtosis measurements, which can provide meaningful measures of signal peaks due to their relation to the probability density function of the data [39]. The probability density function will be affected at its extrema by peaks occurring in the process, and moments of the data will reflect changes in these portions of the probability density function curve. However, as load and speed vary, these time-domain indicators will produce inaccurate results due to the smearing of signal energy and/or random characteristic of signal contents.

3) Frequency domain techniques

Most of the work on mechanical vibration analysis is executed in the frequency domain, especially when related to rotating machinery, which can be viewed as a collection of periodic events occurring simultaneously. The FT of a time signal provides discrete information about each specific event. The time-domain methods mentioned earlier are geared mostly toward the investigation of specific events that are known to be present, or specifically searched for [5]. The methodologies in the frequency domain, on the other hand, tend to be more investigative in nature; more often than not, they are used to observe any events that are occurring at unacceptable levels as opposed to selectively searching for fine details about events that are known to exist [5,8] Figure 1.8. Eccentric shafts generate in large magnitude low frequency harmonics (generally lower in magnitude than gear and bearing signals unless sever faults exist), and adds sidebands to the gear MF's and consequently modulate bearing vibration signals [35]. Shaft misalignment of directly-coupled machines results primarily in elevated vibration at twice the shaft rotation frequency. If angular misalignment (coupling gap) is predominant, then vibration elevation will be noticeable in the axial measurements [36]. Misalignment causes low-frequency amplitude modulation of the gear vibration signal [3,4,38]. Line spectrum is a well-liked spectral analysis approach for shaft defect detection. Line spectrum is simply the FT of the time signal of the motion, which is by far the prevalent measure applied to shaft system diagnostics [8,39,41]. It incorporates the three basic pieces of information normally evaluated: frequencies showing high amplitudes, amplitude levels, and comparison of each other and with previous records. The vibrations are direction-oriented, which is of great importance when

concluding what faults exist. Therefore, it is usually a standard practice to take readings in three coordinate directions: two radial readings mutually perpendicular, and one axial reading. With this information, the analyst is able to identify the sources of trouble. Line spectrum measurements are obtainable using a single channel (i.e. using a single transducer) with the help of a signal analyzer (or FT processing device), for routine monitoring work [36]. In the case of detailed investigative diagnostics carried out on a particular machine to locate one or more problems that cannot be isolated by the information provided by monitoring data alone, there would normally be a second transducer or a key phasor used to provide phase information.
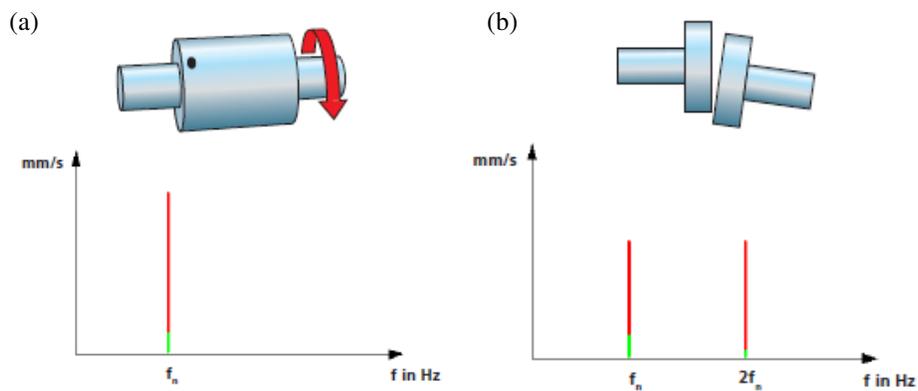
Figure 1.8. Shaft defect frequency response for: (a) imbalanced forces; (b) misalignment [40].

The autospectrum (also known as the power spectrum) measures the power contained in the signal at various frequencies [26,35]. Although not commonly used in shaft diagnostics, it can provide means to quickly locate the problem location where the advanced analysis should be focused. However, when adopted from a single-channel measurement, it does not provide phase information.

1.4 Bearing Fault Detection

The most challenging task in gearbox health condition monitoring could be related to fault detection in rolling element bearings, which remains an open research problem in the R&D field. Rolling element bearings are used extensively in rotating machines to support relative motion between rotors and their housings, and to carry static and dynamic loads [41]. Their performance is of the utmost importance due to their influence on the dynamic behavior of

rotating machinery; they are also a source of vibration and noise in a gearbox even though they are healthy. If a bearing is damaged, on the other hand, it will induce extra noise and vibration in the related machines, and deteriorate transmission accuracy. Surveys have shown that bearing failure accounts for over half of machinery defects [42]. Therefore, reliable bearing fault diagnosis is critical in industries in order to improve operation accuracy and reliability, as well as to reduce maintenance costs [43]. This research focuses on health condition monitoring of rolling element bearings under modulation of gears and shafts.

There are different types of rolling element bearings, for example, based on the structure of thr rolling elements, and the bearings can be classified as roller, cylindrical or tapper bearings and ball bearings. Different from gears and shafts, a rolling element bearing is, in fact, a system that is comprised of an inner ring (or race), an outer ring (or race), rolling elements, and a cage, as illustrated in Figure 1.9. In general, the inner race is fastened to the shaft and rotates with the shaft; the outer ring is mounted in the bearing housing, which is usually fixed.

Bearing components carry dynamic/fatigue loading. Bearing defects can be classified into distributed and localized faults. The dynamic Hertzian contact loading leads to bearing fatigue damage in due course, resulting in micro-cracks and localized defects that include cracks, pits, and spalls on bearing component surfaces. Distributed defects include wear, surface roughness, waviness, and misaligned races. In application, most distributed defects originate from localized defects. Accordingly, this work focuses on analysis of localized rolling element bearing faults.
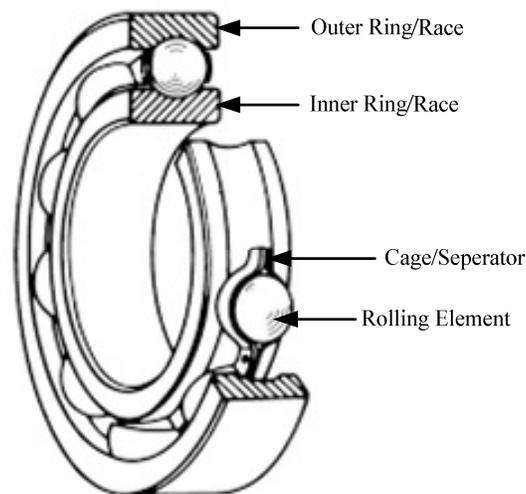
Figure 1.9. The structure of a rolling element bearing (a ball bearing in this case) [44].

10

Bearings generate vibration forces that can excite resonances of the surrounding structures. Although excitation is natural for rolling bearings, these forces can be greatly amplified due to imperfections or defects on the bearing components. Vibration-based fault detection of progressive bearing deterioration during operation could be the most commonly practiced monitoring method [45].

Many techniques have been proposed in the literature to process the vibration signals to extract representative features for bearing fault detection. The features from a vibration signal can be extracted and analyzed in the time, the frequency, and the time-frequency domains, as discussed in the following subsections.

1) Time-domain techniques

If a bearing is damaged (e.g., a defect occurs on the fixed outer race), the repetitive impacts are generated whenever the rolling elements pass (strike) the damaged location on the race, at the same time interval as a ball passing, resulting in rapid acceleration of the bearing components [41,45]. The vibration signals generated from a damaged bearing are usually non-deterministic and non-stationary, especially in situations involving rotating ring/race and rolling element defects, considering rolling element slippage and load zone variations. In addition, other strong vibrations from components, such as gears, could modulate these bearing signatures [43]. Thus, analyzing the vibration signal for reliable and robust indication of the health condition of the bearing remains a challenging task. Unfortunately, as the bearing damage propagates, the impulse signals take on a more random appearance and magnitude, and these classical time-domain indicators (e.g., crest factor and kurtosis) diagnostic accuracy will reduce, and could generate confusing diagnostic information.

2) Frequency domain techniques

Currently, frequency analysis could be the most common approach for bearing defect detection [46]. The FT of the time signals can provide discrete information about each specific event involved. Each component of a bearing has its own characteristic frequency, as does any fault associated with that component. These frequency spectral contents can be used to examine bearing health condition [47].

Consider a bearing of sound condition and no slippage between the rolling elements and the races, as shown in Figure 1.10. Assume that this bearing has a fixed outer race and a rotating inner race (the general case) with the following geometry:

D: outer diameter;

d_m = pitch diameter;

d: bore diameter;

d_b: diameter of a rolling element;

α: the contact angle;

z = number of rolling elements;

w = bearing width;

f_r: shaft speed in Hz.

For an outer race defect, the outer race defect characteristic frequency in Hz is calculated using:

$$f_{OR} = f_r \frac{z}{2}\left(1 - \frac{d_b}{d_m}\cos\alpha\right) \tag{1.1}$$

The inner race defect characteristic frequency is calculated as:

$$f_{IR} = f_r \frac{z}{2}\left(1 + \frac{d_b}{d_m}\cos\alpha\right) \tag{1.2}$$

If a rolling element is damaged, the defect characteristic frequency is computed by:

$$f_{BD} = f_r \frac{z}{2}\left(1 + (\frac{d_b}{d_m}\cos\alpha)^2\right) \tag{1.3}$$
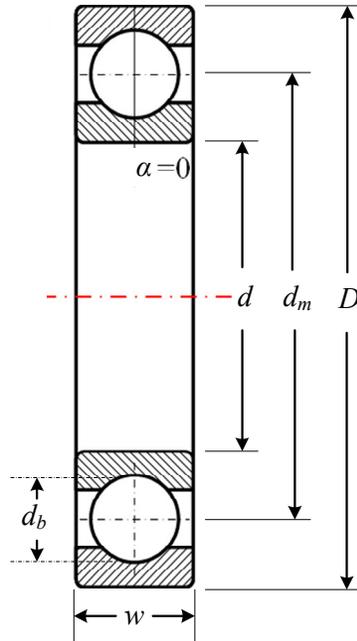
Figure 1.10. Geometry of ball bearing [48].

When a bearing is healthy, the related characteristic frequency is the shaft frequency f_r. As a fault occurs in a bearing component, the corresponding defect characteristic frequency and/or its harmonics will be, in theory, observed in the spectrum.

Other frequency analysis methods include cepstral analysis and higher order spectral analysis. Cepstrum is the spectrum of the logarithm of the power spectrum of the signal, which can be used for detecting the periodicity of spectra spacing between the harmonics [47,49]. Higher order spectral analysis typically refers to bispectrum and trispectrum [35,41], which are also called higher order statistics, since bispectrum and trispectrum are essentially FT of the third and fourth order statistics of the signal. Higher order spectra (i.e., bispectrum or trispectrum) may contain more diagnostic information; the phase correlation between different frequencies [50] as the presence of a defect in a bearing may experience spacing increase between the harmonics of the defect characteristic frequency. Higher order spectra-related methods have been applied for Gaussian noise suppression, non-minimum phase system identification, and non-linear systems detection in machinery [51]. In addition, the bi-coherence analysis is employed to amplify the existing bearing fault frequencies, and to analyze the statistical energies of the corresponding frequency components for bearing fault detection [41,50].

As a matter of fact, the aforementioned frequency analyses at bearing characteristic frequencies is not a simple task, as they require examining specific frequencies, their harmonics and sidebands [51]. Difficulties lie in the fact that the energy of the bearing vibration is spread across a wide range of frequencies of bands and can be easily buried by noise. As a result, resonances of the gearbox components and the surrounding structure will be excited by the defect-induced impulses [52].

Often, incipient damage in a bearing cannot be detected using spectrum analysis, as the energy distribution of fault-related impulses is relatively insignificant compared to that of overall machine component vibration and noise. In addition, direct spectrum analysis is not suitable in this case since it is difficult to establish baseline information. Furthermore, if bearings operate in time-varying operating conditions, spectra of bearing vibrations are dependent upon the load and speed variations. In analysis of higher order spectra, the related estimator requires extensively averaged estimates at several levels of operation procedures. This not only slows down the estimation process substantially, but also reduces the analysis robustness, as stationary assumptions are imposed on a larger segment of the data [46,51]. For non-stationary signals, traditional spectral analysis becomes ineffective since the statistical properties change over time.

3) Time-frequency domain techniques

The popular time-frequency techniques include those such as the short time FT (STFT) [52,53], the Wigner-Ville distribution (WVD) [41,54], the WT [55,56], and the HHT [57,58]. In a STFT plot, we can observe that impacts occur at various times with different frequency spectra [42]. In the case of two defects, two transient impacts can be recognized corresponding to two instances of these defects. The period of time between impacts can be used for fault diagnosis by relating it to the various bearing characteristic frequencies [53]. An inherent drawback with the STFT is its limitations in the time and frequency resolutions. Furthermore, the STFT requires large amounts of computation and storage for displaying the results of the analysis [41,53].

The WVD is a technique to analyze the distribution of signal energy in both the frequency and the time domains. The WVD has an infinite resolution in the time domain due to averaging process over finite time intervals. Moreover, for infinite lag length, it can have an infinite frequency resolution. It is shown that WVD distribution could be applied in bearing fault detection [41]. However, the WVD generates signal deterioration and non-physical (cross-term)

14

interference, which may lead to difficulties in the interpretation of the processing results. Although some improvements in the WVD were made using methods such as Choi-Williams distribution and/or cone-shaped distributions [54], they still require tradeoffs in the cross-terms, which may overlap with auto-terms and make it difficult to interpret the WVD results.

The WT consists of continuous WT, discrete WT, and packet WT. The WT uses variable size windows, allowing for better resolutions [55]. Large time windows are used to obtain precise resolution for low frequencies, while shorter windows provide precise time information for high frequencies. The WT can recognize the leading edge of an impulse and the dampened oscillation across a wide range of frequency bandwidth. The WT has been effectively applied to reduce noise in raw signals [56]. Although the WT can provide some indication of the time response at higher frequencies [55], the corresponding frequency response is not clear due to oscillation around singularities and aliasing. These deteriorations could result in difficulties in detecting the individual structural resonances excited by the bearing defect-induced impact.

The HHT consists of the processes of the EMD and the Hilbert spectral analysis [57]. A non-stationary signal is decomposed into a series of data sequences with different characteristic scales, that is, intrinsic mode functions (IMFs) and residual function [58]. HHT has been used in non-stationary signal modulations. For example, Yan *et al*. [59] have applied the HHT to process vibration signals for machinery health condition monitoring; however, their method could not effectively isolate distinctive condition-related IMFs for signal demodulation and features extraction. Rai and Mohanty have proposed a method to process the IMFs of HHT results using FT spectra, which has redeemed better results than using the FT alone [60]. However, in order to produce acceptable results, the authors have to rely on 18 IMFs to process the data [60], which is considered unconventional due to the lack of representative features in the last IMFs. Peng *et al*. have compared HHT with the WT spectrum using a simulated signal with a rotor model [61]. The processed HHT spectrum could recognize the presence of impacts, but did not produce clear bearing defect characteristic frequencies. Although the paper in [61] has used the first two IMFs, which were believed to hold most of the representative information, its conclusion could not be supported by other researchers who used more than two IMFs. Yang *et al*. [62] have applied the IMF envelope spectrum and support vector machine for bearing fault detection. However, the loss function used for supporting vector regression did not have clear statistical interpretation,

whereas the function (i.e. support vector machine function) could generate over-fitting in model selection.

This author has also proposed a normalized HHT (NHHT) [63] and an enhanced HHT (eHHT) [64] techniques for non-stationary feature analysis and bearing fault detection. In NHHT, the weight of each IMF in terms of its contributions to normality and its correlation to a related condition is first determined. An integration method is then suggested to maximize the output of the IMFs to process the bearing vibration signals. Test results show that the proposed NHHT outperforms the related techniques in processing bearing health conditions. However, in the case with low signal-to-noise ratio and with multiple defects on the same bearing, the accuracy of this method deteriorated due to signal modulation and masking of bearing related characteristic components. The proposed eHHT, on the other hand, applied an information measure method to process bearing signals; it can partly solve the problems in NHHT. Although the eHHT produced promising results in extracting bearing condition-related characteristic features, it still could not automatically select the most distinguishable IMFs for representative feature extraction [63,64].

1.5 Fault Detection in Bearings Modulated by Gear Meshing

In geared systems, especially high-speed gearboxes, a mixture of bearing faults and gear-related signatures are observed over the whole frequency bandwidth extending into the high frequency range. Bearing signals are modulated by gear meshing. This signal modulation occurs due to the close physical contact of the gear and bearing elements [55]. Under these circumstances, the results from these bearing fault diagnostic techniques are not guaranteed to be reliable [3,5]. Understanding the interaction and modulation between the supporting structure and the rotating components of a transmission system is one of the most challenging tasks of designing more advanced gearbox simulation models [8,66]. The property of the structure supporting rolling element bearings and shafts has significant influence on the dynamic response of the system [52]. In addition to sidebands caused by a rotating carrier, a large number of gear manufacturing errors can also cause variations to modulate the dynamic gear mesh forces in the form of amplitude modulation, frequency modulation, and phase modulation [41,52]. However, changes in deformations of the gear train might provide additional mechanisms for sidebands. The gear

load sharing characteristics impact the amplitude modulation as well as the dynamic gear mesh forces [43]. Thus, it is highly desirable to find a strategy that can be used to improve diagnostic accuracy by accounting for the effect of signal transmission path impedance from the fault vibrating source to the measurement sensors. This requirement often drives the sensors/transducers to be placed in an easily accessible location on the machine, such as on an exposed surface of the gearbox casing, or on an exposed and readily accessible structural frame on which the machine is mounted. This work aims to separate gear and bearing signatures from gearbox signal for bearing fault detection.

Bearing fault detection in the presence of strong interfering gear signals in gearboxes has gained new interest in the machine condition monitoring communities around the world [65]. More emphasis is placed on how to differentiate between gear and bearing signals where the two signals may inter-modulate in a complicated manner [66]. The fundamentals of this type of distinction is essentially based on decoupling strategies to recognize gear signals as being periodic, whereas bearing signals experience some randomness and are approximated to be second-order cyclostationary [67]. Such distinction can provide more accurate detection for bearing faults in gearboxes, by separating stochastic (bearing) signals from deterministic (gear) contents [65,67]. There are several vibration-based monitoring techniques currently available for rolling element bearing fault detection in gearboxes, which can be classified, similarly, into time-domain or statistical analysis, frequency or cepstrum analysis, and time-frequency analysis. A brief review of each is provided below.

1) Time-domain techniques

In the time-domain, statistical analysis could be the most commonly used method in fault detection. The information obtained from the gearbox is compared to the characteristics obtained at its healthy state [68]. Other fault detection methods use time synchronous average (TSA) signals [69]. However, to extract the periodic signal, the operating frequency has to be known prior to the analysis. Another limitation to using synchronous averaging-based methods is that the signal statistical properties vary with the varying load and speed conditions, making it unreliable. Another time domain-based technique uses linear prediction such as autoregressive models generally obtained by using the Yule-Walker method [70]. The deterministic or predictable part of the generated autoregressive model is based on previously determined

samples from the immediate past, which is then used to predict the next sample. A major limitation of such autoregressive method is avery large number of components must be removed. As a result, both the resulting mesh harmonics and sidebands in gear spectra can be problematic to detect because the number of components and their interaction is complex, even though such limitations could be overcome to some extent by the frequency or cepstrum analysis.

2) Frequency domain techniques

In the frequency domain, bearing faults are typically diagnosed by analyzing the envelope spectrum of the measured signal [71]. However, the presence of the bearing fault in the envelope spectrum is often masked by high energy deterministic components of gear MF and its harmonics. This will cause an energy smearing of the bearing frequencies in the amplitude spectrum [72]. Cepstrum analysis is referred to as the inverse FT of the estimated spectrum with the purpose of detecting echoes in seismic signals. The Cepstrum analysis is employed in the automated cepstrum editing procedure [73] and cepstrum pre-whitening [74] that use equivalent liftering approach to remove harmonics but not to completely cancel the resonances [75]. Although they are proven to be effective in separating the bearing signal from the gear signal, they are still not suitable to detect a bearing defect if the signature property varies with time without prior baseline information. Some of these problems could be partly solved by the use of multiresolution time and frequency-based analysis, as discussed next.

3) Time-frequency domain techniques

Multiresolution time-frequency information is necessary for the investigation of transient feature properties in vibration signals, such as STFT [76-78], HHT [79,81], and WT [82-84]. These multiresolution methods focus on the analysis of non-stationary signals in the time-frequency domain, whose spectral contents and statistical properties change with time. The STFT is able to extract both frequency and time information from gearbox and bearing vibration signals [76]. It calculates the FT of a time shifted window of the original signal [77]. However, STFT suffers from fixed resolution problem in time or frequency domains as previously discussed, which cannot properly identify different frequencies once the window size is selected in analysis [78].

As stated in subsection 1.4, the HHT uses EMD to extract IMFs and the residual function, and then applies the Hilbert spectral analysis [79] to process the non-stationary signal [80]. Although EMD decomposes the signal according to the frequency [81], the results are only approximate because the EMD cannot obtain the ideal decomposition when noise interference exists. Errors occurring from the decomposition can be overcome to some extent by using the newly proposed Variational Mode Decomposition (VMD) [85]. VMD minimizes errors between the extracted IMFs using a concurrent variational model. Unlike its EMD counterpart, VMD has rigorous mathematical foundations for decoupling different features [86]. Although VMD has potential in practical development, its computation is complex, which can limit its application in real-time.

WT decomposition is a widely used multiresolution technique in vibration analysis for machinery fault detection [82-84]. This type of analysis is suitable for signals that have high-frequency components of short duration, and for low frequency components of long duration, which is generally the nature of fault-related features [87]. A common multiresolution technique is the discrete WT [88], which can be considered a composition of bandpass filters with constant relative bandwidth or constant–Q factor. Q is defined as the ratio of center frequency to bandwidth, where the ratio of the change in the frequency versus the change in time resolution remains constant [89]. Therefore, as the change in frequency varies with frequency responses, the corresponding time resolution also changes to satisfy the uncertainty condition [89,90]. Similar to discrete WT, the dyadic WT has proven to have good time resolution at high frequencies, and good frequency resolution at low frequencies [90]. However, dyadic WT has a low and constant Q factor, which is not tunable according to the frequency content.

To improve dyadic WT, the tunable Q factor WT (TQWT) has been recently introduced in [90,91], in which the Q factor has been tuned according to the oscillatory behavior of the signal. In TQWT, Q factor can also be tuned according to the frequency content of the input, which can make it more flexible than the discrete WT [91]. In principle, a high Q factor transform is suitable for observing oscillatory signals, whereas transient signals are modeled using low Q factor wavelets. The TQWT has been adapted in the works of Selesnick [92] for the separation of high and low resonance components of oscillatory signals using the resonance-based signal sparse decomposition (RSD) method. The RSD is a decomposition method that

combines two procedures: the TQWT for decomposing a gearbox signal, and the morphological component analysis for reconstruction of the signal. Utilizing RSD, the signal can be decomposed into high and low resonance components according to the oscillatory behavior of the signal components [90,92]. Because the characteristic features of the gear and the rolling element bearing have different oscillatory behaviors, it is possible that the RSD can be used to separate both from the vibration signals of gearboxes [92].

On the other hand, most RSD or TQWT based approaches used for gearbox health monitoring require post-processing operations to further process the resulting high and low resonance response frequencies, using methods such as statistical-based analysis, genetic algorithm, artificial intelligence, or filtering processes [93-97]. For example, the gear and bearing fault detection technique in [93] has been based on determining the TQWT denoised signal. Features at each level are extracted using neighboring coefficients. Authors in [94] have used a kurtosis-guided measure to select the appropriate level for post-processing bearing feature. In [95], a smoothness index, kurtosis, and genetic algorithm are combined to select TQWT level(s) first, and next applied the Teager energy-based modulation to post-process the machinery conditions. In [96], IMFs are extracted by using ensemble EMD, and envelope modulation has been applied to the low Q-factor of TQWT signal to recognize bearing faults. In paper [97], an adaptive comb filter has been adopted to remove high energy (shaft signal) from the lowpass resonance response for bearing fault detection. It appears that if the interaction between gearbox system components is complex, some more complex post-processing procedures are required in this approach. This will be of great concern if the vibration signals are non-stationary and non-linear, which will add complexity to the detection process significantly. Thus, one of the objectives of this works is to eliminate post-processing meanwhile extracting meaningful features for gearbox bearing fault detection.

1.6 Objective and Strategy

To tackle the aforementioned problems, the goal of this research is to develop advanced signal processing technologies to achieve more efficient fault detection in rolling element bearings in gearboxes. The first objective of this work is to propose a new technique, namely an enhanced morphological denoising technique, for active signal filtering. This filtering technique is based

on mathematical morphology measures. The second objective is to develop new signal processing techniques to extract more robust features for incipient bearing fault detection in gearboxes. Specifically, an integrated HHT technique will be proposed for non-stationary feature analysis, and an IMF integration strategy will be suggested for bearing feature extraction and analysis. The third objective is to propose a leakage-free RSD technique to remove interference from high-energy periodic signals, and then to process the signal residual to generate characteristic features for bearing fault detection.

The processing procedures for gearbox bearing fault detection are illustrated in Figure 1.11. Gearbox vibration signals are collected by the use of appropriate accelerometers. After preprocessing such as ADC, the collected signal is fed to a computer using a data acquisition card for further processing. The proposed signal processing techniques are applied to extract representative features for bearing fault detection in gearboxes.

(1) A new enhanced Morphology (eM) denoising filter technique will be proposed to denoise vibration signals. The eM filter is based on the information content and the distribution of the incoming signal to enhance the fault's distinguishable features.

(2) A new signal processing technique, integrated HHT (denoted by iHT), will be proposed for non-stationary bearing signal analysis and bearing fault detection under controlled operating conditions. The iHT technique will properly select the most representative IMF(s) based on a unique measure, and extract features for bearing fault detection.

(3) A new leakage-free RSD (namely LRSD) will be suggested to remove gear vibration signals, and then to adaptively decompose the signal residual into transient (bearing) and oscillatory (gear and shaft) components for bearing fault detection.

(4) The effectiveness of the proposed fault detection techniques will be verified experimentally corresponding to different gearbox conditions.
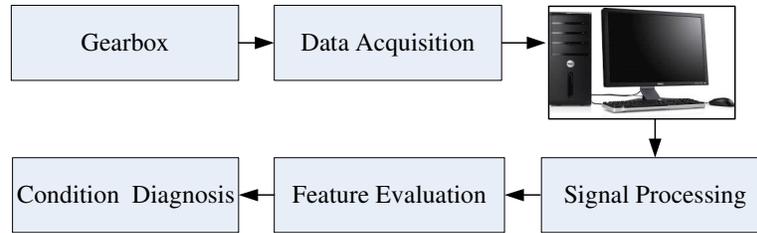
Figure 1.11. Schematic diagram of the gearbox diagnostic system.

1.7 Significance of the Proposed Research

Nowadays, it would be beneficial to have a reliable condition monitoring system that would provide insight into the health condition of gearboxes in real-time. Reliable diagnostic tools for gearbox health condition monitoring can aid in scheduling maintenance efficiently without the need for periodic shutdown for routine inspections. The proposed research work is an interdisciplinary project involving mechanical system analysis, signal processing, electronics, and software engineering. The methodologies of this project can also be used in other applications such as non-linear and non-stationary signal processing, and systems control. The contributions of this work will result in some high quality academic publications in related fields. A list of contributions is listed below.

Contributions list:

Osman, S. and Wang, W.Q., "A leakage-free resonance sparse decomposition technique for bearing fault detection in gearboxes", Measurement Science and Technology, 2017.

S. Osman and W. Wang, "A morphological HHT technique for bearing fault detection," IEEE Transactions on Instrumentation and Measurement (in press), 2016.

S. Osman and W. Wang," An integrated Hilbert-Huang technique for bearing fault detection", Proceedings of the 2016 IEEE International Conference on Prognostics and Health Management, Ottawa, Canada, 2016.

S. Osman and W. Wang, "A normalized Hilbert Huang transform technique for bearing fault detection", Journal of Vibration and Control (in press), 2015.

W. Sui, S. Osman and W. Wang, "An adaptive envelope spectrum technique for bearing fault detection", Measurement Science and Technology, Vol. 25, No. 9, (095004), 2014.

22

W. Sui, S. Osman and W. Wang," An Adaptive MED envelope analysis technique for bearing fault detection," Proceedings of the Canadian Society for Mechanical Engineering International Congress, Toronto, Canada, 2014.

S. Osman and W. Wang, "A Hilbert Huang transform technique for bearing fault detection", Proceedings of the Canadian Society for Mechanical Engineering International Congress, Toronto, Canada, 2014.

1.8 Thesis Outline

The outline of this report is summarized as follows:

Chapter 2 presents the suggested eM filter technique for vibration signal denoising and feature analysis.

Chapter 3 discusses the suggested eM and NHHT technique for bearing fault detection. Its effectiveness will be examined using different bearing test conditions.

Chapter 4 discusses the proposed iHT technique for non-stationary signal processing and bearing fault detection.

Chapter 5 discusses the proposed LRSD technique to process the signal residual for bearing fault detection in gearboxes. Its performance will be evaluated experimentally corresponding to different bearing conditions in a gearbox.

Chapter 6 summarizes the conclusion remarks and ideas for future research.

Chapter 2

Enhanced Morphology (eM) Denoising Filter Technique for Vibration Signal Processing

In general, if the bearing in a gearbox is damaged (e.g., a fatigue pit on the fixed ring/ race), impulses are generated whenever rolling elements strike the damaged region. Bearing fault detection is based on the examination of the impulse responses. Due to the impedance effect of the transmission path, the measured signal using a vibration sensor (e.g., an accelerometer) is a modulated signature of the defect-related impulses. To highlight defect-related impulses, a denoising filter will be useful to improve the signal-to-noise ratio. Several filtering algorithms have been proposed in the literature for vibration signal denoising [38,47,98]. Wiggins originally has proposed a minimum entropy deconvolution (MED) filter for the deconvolution of the impulsive sources from a mixture of signals [98]. The MED has shown its effectiveness to highlight the impulse excitations from complex responses [19,98,99], which has also been used for machinery system condition monitoring. For example, Endo *et al.* have combined the MED, autoregressive models and WT for fault detection in gear systems [19] and bearings [98]. This author has also adopted the MED filter to highlight impulses while minimizing noise (i.e., entropy) associated with the signal transmission path for bearing fault defection [64,99]. Entropy minimization is achieved by maximizing signal kurtosis, which is related to impulse-induced distortion in the tails of the distribution function. However, MED is complex in implementation especially for real-world applications, and its accuracy depends on prior knowledge of the filter initialization, the filter length, and the stopping criterion. In general, most of these filtering techniques share a common weaknesses: they cannot properly process all types of gearbox component signals, especially those modulated by gear signals. This challenge lies in the assumption employed by filter algorithms, that is, there exists certain characteristics to distinguish the defect-related signals from noise. Unfortunately, these assumptions are usually application-specific.

To overcome these limitations, an enhanced morphological denoising (eM) technique is proposed in this chapter to facilitate vibration signal denoising and filter implementation. The suggested eM filter will employed in Chapter 3 with the integration of the HHT to process the

bearing vibration signals for bearing fault detection [63]. Its effectiveness will be verified experimentally and compared to other related techniques in Section 3.3.

2.1 Mathematical Morphology Analysis

Mathematical morphology is a well-accepted tool in signal processing for extracting features and components vibration signatures. Due to its suitability for shape-oriented problems, morphological signal processing has been used in many applications such as computer vision, template matching, pattern recognition, and machinery fault detection. The morphology theory was first introduced in 1964 based on set theory and on certain problems in mineralogy and petrography [100]. In the mid-1980s, it received wider acceptance in image processing and non-linear filtering [101], which was later generalized to arbitrary lattices theories [102]. In morphological decomposition, a complex signal can be separated from the background into various components reserving morphological features of the signal.

In morphology analysis, sets present objects in a signal [100]. In this chapter, the morphological signal processing is used to modify the shape of a signal. The morphology transforms can be divided into two types: the binary morphology transform and the gray-level (multi-value) morphology transform [101,102]. In this work, we will concentrate on binary morphology for ease of implementation and results explanations. The basic operators of morphology transform will be briefly discussed next.

Suppose $z(n)$ is the discrete-time signal over $Z = \{0, 1, \ldots, N\text{-}1\}$, where n is the index variable and N is the length of the signal. $g(n)$ is the discrete-time structural element (SE) over the domain $G = \{0, 1, \ldots, M\text{-}1\}$, where M is the length of the SE (usually $M << N$).

1) Morphological preliminaries

The morphological operation uses SE as probes to analyze the signal properties. A SE set can be either flat or non-flat, depending on the application. Flat SE (i.e., defined by a set) makes morphology easier to explain. Nonetheless, for a more general case it is also possible to define SEs as a non-flat function. The morphological operations will be explained next using flat SEs.

The basic morphological signal analysis is perturbed by transforming the signal through intersection with the SE, which is a probe that scans and modifies the input data by taking into account local information. The SE is a very small set, not only in the number of points, but also in the distance between the points. The general morphology transform assumes that all sets are closed, and signals are continuous. The basic analysis is to transform the signal through intersection with the SE. An important parameter in the construction of a flat SE is its length. If it is shorter, it is easier to extract the impulses by suppressing noise [101-103]; however, it will become more difficult to demodulate the signature, and vice versa.

2) Dilation and erosion

The two basic morphological operators are the *dilation* and the *erosion*, which are defined respectively as the maximum and minimum value of a function z in a neighborhood of the SE g [102,103]. Specifically, the dilation operation, denoted by δ, is defined as:

$$[\delta_g(z, g)](n) = \vee_{m \in G}\, z(n+m) \tag{2.1}$$

where $\vee$ represents the supremum operator and m is the length of the flat SE.

The erosion operation, denoted by ε, is defined as:

$$[\varepsilon_g(z, g)](n) = \wedge_{m \in G}\, z(n+m) \tag{2.2}$$

where $\wedge$ denotes the infimum operator; $\vee$ and $\wedge$ can also be treated as the respective maximum and minimum operators of function z in a neighborhood defined by the SE (i.e., g).

The dilation can expand the peaks in the signal but will shrink the valley. The erosion has the opposite effect. These two operators are related simply by *duality*:

$$\delta(-f) = -\varepsilon(f) \tag{2.3}$$

Therefore applying one to the peaks will produce the same result as applying the other to the valleys. That is, the dilation expands the peak in the same way as the erosion expands the valleys.

Essential properties of the morphology transform

The dilation and the erosion properties are relatively simple (for the proofs and additional properties of the morphology transform, refer to [104-106]). For example, both operators preserve the ordering relation (*increasingness*):

$$g \geq z \Rightarrow \begin{cases} \delta(g) \geq \delta(z) \\ \varepsilon(g) \geq \varepsilon(z) \end{cases} \tag{2.4}$$

If the SE, *g*, contains the origin, there is also the *extensivity* of the dilation and the *anti-extensivity* of the erosion:

$$0 \in G \Rightarrow \delta_G(f) \geq f \geq \varepsilon_G(f) \tag{2.5}$$

This implies that, as long as the origin is included in the SE, the dilation will not lower the values of the signal, or the peaks in the signal are enlarged. If the origin is not included in *G*, the objects are enlarged and translated:

$$y \in G \Rightarrow [\delta_G(z)](g) \geq z(n+m) \geq [\varepsilon_G(z)](m) \tag{2.6}$$

The result of the dilation at a point z is only affected by a local region of the input vibration signal. It also has the following properties:

Distributivity:

$$\delta(z \vee g) = \delta(z) \vee \delta(g) \tag{2.7a}$$

$$\varepsilon(z \wedge g) = \varepsilon(z) \wedge \varepsilon(g) \tag{2.7b}$$

The dilation distributes with the supremum, and the erosion with the infimum.

Associativity:

$$\delta_{\delta_G(N)} = \delta_G \delta_N \tag{2.8a}$$

$$\varepsilon_{\varepsilon_G(N)} = \varepsilon_G \varepsilon_N \tag{2.8b}$$

To simplify expressions, if the Minkowski algebra $\delta_g \sim z \oplus g$ and $\varepsilon_g \sim z \ominus g$ are used [101], Equations (2.1) and (2.2) can be rewritten as:

$$[\delta_g(z, g)](n) = (z \oplus g)(n) \tag{2.9a}$$

$$[\varepsilon_g(z,\, g)](n) = (z \ominus g)\, (n) \tag{2.9b}$$

As a result, the dilation or erosion operation becomes simpler to implement and easier to compute, as illustrated in Figure 2.1. Furthermore, based on the property of *Commutativity*, it is possible to change the order of the operands:

$$\delta_B \delta_C = \delta_C \delta_B \tag{2.10}$$

3) Opening and closing

The closing and opening operations, denoted by "●" and "○", respectively, are made by properly combining the basic dilation and the erosion, such that:

$$(z \bigcirc g)(n) = (z \ominus g \oplus g)(n) \tag{2.11a}$$

$$(z \bullet g)(n) = (z \oplus g \ominus g)(n) \tag{2.11b}$$

As an illustration, consider a simulated signal with two scales of impulses, which is sampled as shown in Figure 2.1(a). It is processed with a flat SE {0, 0, 0, 0, 0, 0, 0}, where the underlined position is the original seed point. Although the dilation will expand the maximum value of the signal, it will reduce the valleys of z, as illustrated in Figure 2.1(b). In contrast, the erosion will reduce the peaks but increase the minima value of z (Figure 2.1(c)). The dilation can diminish the number of local minima, which cannot be restored by subsequent erosion. Thus, the closing will produce a simplification filtering of the signal. It can be seen from Equation (2.11) that the mirroring of the SE in the second operation, $g \ominus g$ or $g \oplus g$, can provide anti-extensivity in the closing and opening [101,103]. The mirroring of the SE can also make the operation independent of the SE origin. In this light, the opening in Figure 2.1(e) will preserve negative impulses and reduce positive impulses, and vice-versa for the closing, as demonstrated in Figure 2.1(d).
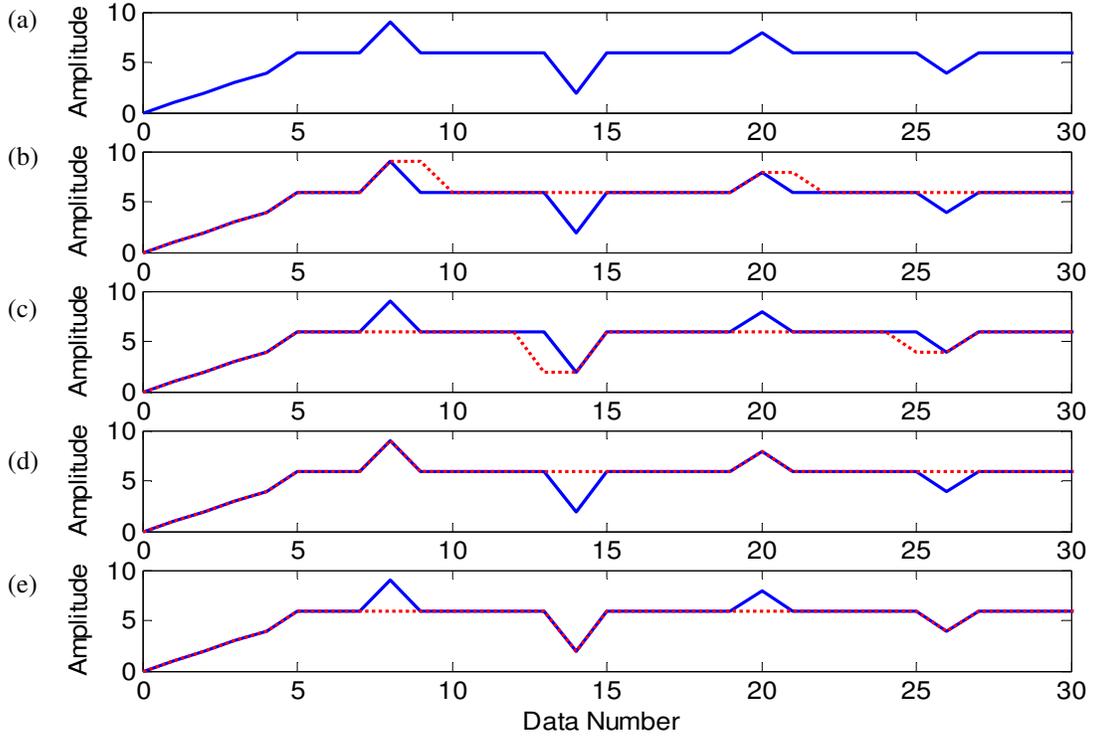
Figure 2.1. Signals produced by using different morphological operators: (a) original signal; (b) after dilation; (c) after erosion; (d) after closing; and (e) after opening. The solid blue line represents original signal and the dotted red line is the modified signal.

In general, it is difficult to obtain the prior knowledge of the positive or negative impulsive features from a signal, such as in the case of bearing impulses. To solve this problem, our proposed approach is to integrate the opening and closing operations of an appropriate SE length to filter out the noise and reconstruct the remaining objects. Correspondingly, the morphological difference filter function, $\hat{f}$, will be formulated as:

$$\hat{f} = f \bullet g - f \circ g \tag{2.12}$$

The $\hat{f}$ filter will be used to extract the impulses, and can be rewritten as:

$$\hat{f} = f \bullet g - f \circ g = (f \bullet g - f) + (f - f \circ g) \tag{2.13}$$

where $(f \bullet g - f)$ is the Black Top-Hat transform used to extract negative impulses, and $(f - f \circ g)$ is the White Top-Hat transform used to extract positive impulses.

29

2.2 Proposed eM Filtering Technique

Before introducing our developed eM technique for signal processing, we will firstly summarize the related applications of the morphology transform in the literature for signal analysis and machinery fault detection.

Zhang *et al*. have used a flat structural element for bearing fault detection using multi-scale fractal dimensions based on morphological covers [107]. This technique has relied on empirical methods for obtaining the maximum scale and the length of the moving window, which cannot be used in general applications. A similar technique has been used for gear fault detection in [108], which also has similar limitations as in [107]. A double-dot SE in a multi-scale morphology analysis has been proposed in [109] for bearing diagnostics, which proved to perform better than a flat SE; however that method lacked an analytical selection procedure of double-dot SE parameters. Dong *et al*. have proposed a blind separation method based on morphological filtering and singular value decomposition [110], but it has a higher level of complexity, which can increase difficulty in implementation and computation. Authors in [111] have used the Bottom-Hat transform in adaptive noise cancellation and multiscale morphology for bearing fault detection. Although the technique worked well for enhancing the bearing characteristic signatures, it still lacked an analytical method for the selection of the SE. Meng *et al*. have used the morphological filter, the invariant wavelet, and improved ensemble EMD for bearing signal analysis [112]. However, the enhancement mechanism could not be explained properly due to the lack of error tracking, which made it impractical for other applications. In [113], Chen *et al*. have used triangular SE and autocorrelation analysis for bearing signal classification. However, the related methodology did not account for effects of scales, shape, and height levels, which can deteriorate the processing results. Hu and Xiang have compared different morphology analysis operators for bearing and gear fault detection [114], using empirical selection of morphology analysis operator and SE length. Currently, it lacks appropriate approach for automatic selection and integration of suitable SE shape and parameters [114-117]. As a general practice, the SE length is selected about 60-70% of the repetition period [116,117]; however, this may not be suitable for many dynamic system analyses such as the case of bearing fault detection, as demonstrated in Section 2.3.

To overcome these aforementioned limitations of current morphology transform-based filters, a new analytical mechanism of selecting morphological thresholds is proposed in this work. The selection of the filter length is based on the information content and the distribution of the input signal. The Renyi entropy is used to measure the correlation between variables [118,119]. The Renyi entropy takes into account a more generalized non-linear correlation, and is relatively easier for implementation on non-linear signal analysis.

1) Renyi Entropy (RE)

The use of RE is motivated by deriving a possible closed-form expression of entropy in order to avoid resorting to non-linear measures. The RE is introduced using the concept of generalized probability distributions and generalized random variables. It is an extension of the ordinary notions to quantify the diversity, uncertainty, and randomness of random experiments [119]. The morphological difference filter function, $\hat{f}$, as defined in Equation (2.13) will be used to extract the positive and negative impulsive features for bearing signal analysis. A new strategy is suggested in the proposed morphological filter to select an appropriate length of the SE. Different from the general autocorrelation functions [118], the proposed method will use RE to process the non-linear correlation in signals. RE, R_α, can quantify the diversity and uncertainty of random observations [119], which is defined as:

$$R_\alpha\left(\hat{f}_q\right) = \frac{1}{1-\alpha}\log_2\left(\sum_{n=1}^{N} p_n^\alpha\left(\hat{f}_q\right)\right) \tag{2.14}$$

where $\hat{f}_q$ is the morphological filter with probability p_n; $n = 1, 2, \ldots, N$, and N is the signal length; and $\alpha > 0$ is the RE order. As R_α decreases, the function randomness decreases. The proposed morphological filter $\hat{f}_q$ corresponds to each SE length q, will be determined by:

$$\hat{f}_q = (f \bullet \Gamma_q - f) + (f - f \circ \Gamma_q) \tag{2.15}$$

where Γ_q is the qth selected length of SE.

2) The proposed eM filter

In the proposed morphological filter, the indicator ϑ_q is formulated by considering kurtosis and entropy (i.e., R_α) of each filtered signal corresponding to a certain SE filter length,

$$\vartheta_q = \frac{\dfrac{K(\hat{f}_q)}{R_\alpha(\hat{f}_q)}}{\displaystyle\sum_{q=1}^{Q} K(\hat{f}_q) \bigg/ \sum_{q=1}^{Q} R_\alpha(\hat{f}_q)} \tag{2.16}$$

where K denotes kurtosis to account for signal peakness properties, and Q is the total number of search filter lengths. ϑ_q is used to determine the appropriate SE filter length. This proposed eM filter will synthesize the outputs of Equation (2.16) to optimize SE filter length in order to enhance the impulses and increase signal-to-noise ratio.

The higher value of ϑ_q in Equation (2.16) corresponds to the sharper impulse using the filter with the chosen SE length. This is because lower R_α and higher kurtosis K will increase ϑ_q, which corresponds to lower signal randomness and higher peakness for the filtered signal.

The most important parameter of the proposed eM filter is the SE length. In general, the range of the filter length is selected over 10% to 90% of the cyclic interval [115]. In bearing vibration signal analysis, the generally applied filter length is 60%-70% of the cyclic interval [116,117]; but it may deteriorate processing accuracy when the signal is non-linear or non-stationary such as in the case of rotating race defect or rolling element defect signals. Although the finer search spacing can generate more filter lengths for optimization, it can lead to slower convergence in calculation. The proposed eM technique will process the signal in the frequency domain; its implementation and effectiveness will be discussed in the following section.

2.3 Performance Evaluation

Simulation testing

In general, the eM filter parameters (i.e. flat SE filter length) are determined to be 60%-70% of the cyclic interval [116,117] or by trial and error. A series of simulations will be carried out corresponding to different impulse and signal properties (e.g., noise level). The evaluation of the eM filter can be obtained by the number of impulses recognized and their amplitude compared to

other signatures within the signal. Table 3.1 summarizes the simulation results corresponding to different impulse number and noise levels. In general, signal length does not influence the eM filter results; the signal length is set to 10,000 samples. The criterion is to recognize the impulses clearly with respect to sufficiently large ϑ_q values. eM filter convergence depends on the signal characteristics with greater values of ϑ_q. When the signal contains 1 to 7 simulated impulses, the eM filter is employed with the SE length that corresponds to the greatest value of ϑ_q. However, if the signal contains too many impulses (i.e., more than 10 impulses), the large number of impulses as noise would be treated like noise. On the other hand, when noise is added to the tested signal with different magnitude levels (e.g., 20% to 60% of signal's maximum magnitude), the eM filter converges and can enhance the impulses in the signal; however, not all the impulses are enhanced when the noise level exceeds 60% of signal's maximum magnitude.

As an example, consider a simulated signal consisting of five impulses and some noise (30% and 45% of signal's maximum magnitude) as illustrated in Figure 2.2(a) and 2.2(b), respectively. The signal length is set to 10,000 samples. Figure 2.3 illustrates the processing results of eM filters with filter lengths 10%-90% of the cyclic interval. It is seen that these five distinctive impulses can be clearly highlighted if the filter length is 40% of the cyclic interval (Figure 2.3(a)), in this case. Although the filter with length 40% has the higher ϑ_q value (Figure 2.3(a)) than filters with length 20% (Figure 2.3(b)), it cannot recognize all of the five impulses due to noise distortion as illustrated in Figures 2.4 and 2.5, respectively. On the other hand, as demonstrated in Figures 2.4 and 2.5, all nine eM filters converge quickly, however, the convergence of the implemented eM filter is sensitive to filter length. As a result, by trial and error, the filter length of 20% of the cyclic interval is chosen for this example. After the vibration signal is denoised by using the adopted eM filter, it will be further processed by the use of the proposed normalized HHT technique as discussed in Chapter 3.

Table 2.1. Summary of initial values of the eM filter.

Parameters	Tested Range	Impulses Enhanced (%)
Filter length	[0.1, 0.9]	[60, 100]
Impulse number	[1, 7]	[40, 100]
Noise level (%)	[20, 60]	[30, 100]
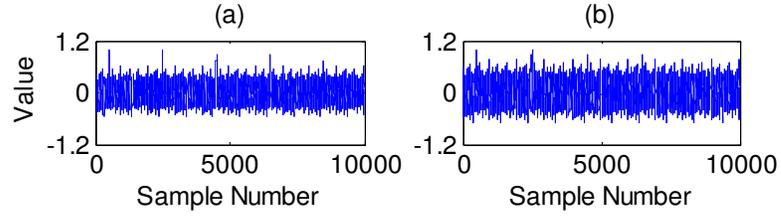
Figure 2.2. Simulated input signal; (a) with 30% noise level; (b) with 45% noise level.
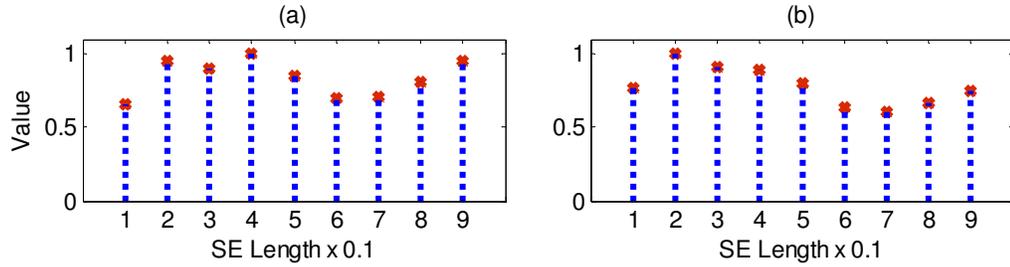
Figure 2.3. Demonstration of normalized ϑ_q indicators versus filter length corresponding to simulated signal in Figure 2.2 for: (a) with 30% noise level; (b) with 45% noise level.
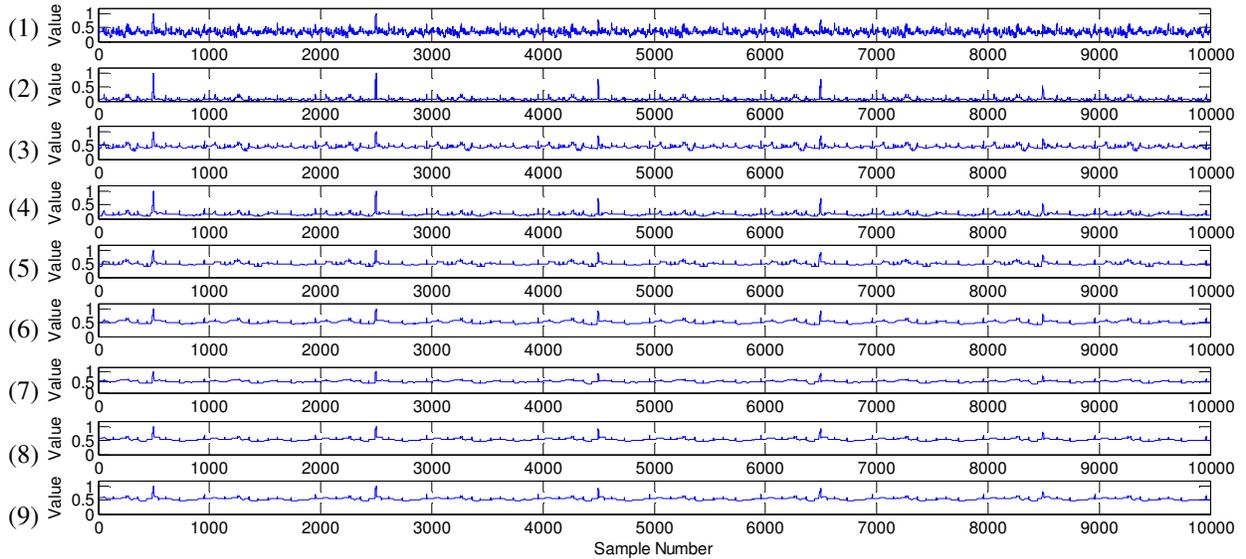
Figure 2.4. Response of a test signal with 30% noise level using eM filters with different lengths : (1)-(9) corresponding to 10%-90% of the cyclic interval for the simulated input signal in Figure 2.2(a).
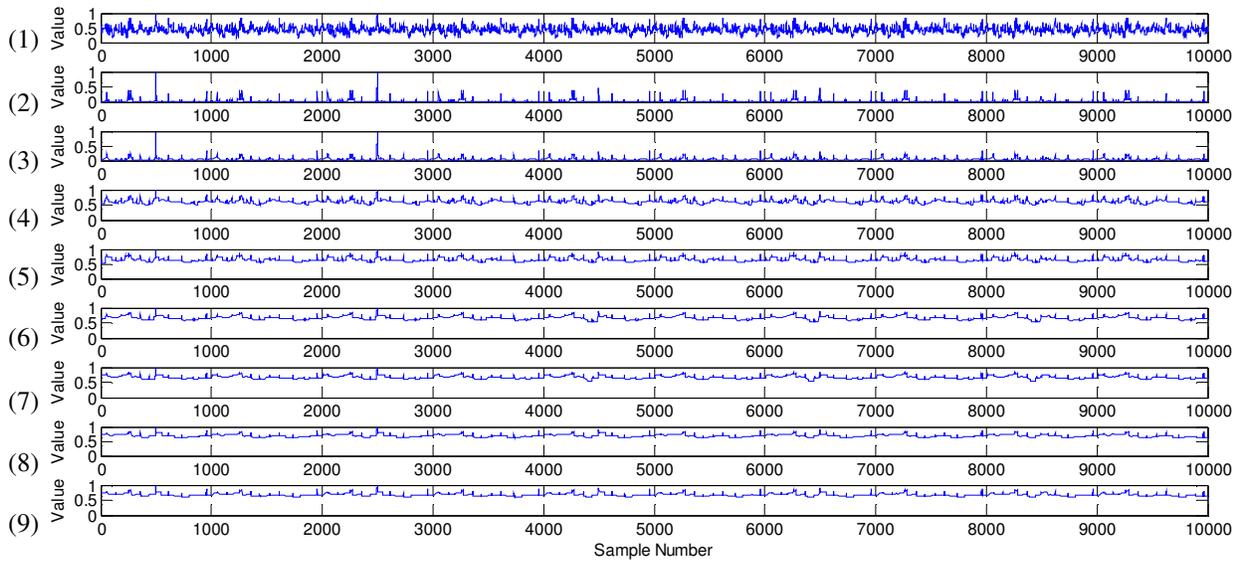
Figure 2.5. Response of a test signal with 45% noise level using eM filters with different lengths: (1)-(9) corresponding to 10%-90% of the cyclic interval for the simulated input signal in Figure 2.2(a).

Chapter 3

eM Filter-based NHHT Technique for Bearing Fault Detection

In this chapter, the eM filter is applied in combination with the NHHT technique [63], MH in short, for bearing fault detection. In the proposed MH technique, the bearing signal is firstly preprocessed using the eM filter with an appropriate SE length, and then the NHHT will be applied for bearing fault detection. Its effectiveness will be examined experimentally corresponding to different controlled bearing conditions.

3.1 Normalized Hilbert Huang Transform (NHHT)

In the NHHT, we deal with determining the weight of each IMF in terms of its contributions to normality and correlation to related condition. The d'Agostino-Pearson (DP) normality test is used to maximize combination output of the IMFs integration. Function non-normality will be a problem when the sample size is small, or when data is highly skewed, or leptokurtic. Normality becomes an important concern when there are clumps in the tails of the distribution function of the data set.

In bearing fault detection, the classical skewness and kurtosis coefficients have some clear limitations: they both have zero breakdown values, and are sensitive to outliers. One single outlier can make the estimate become too large or too small, making it difficult to interpret. Another disadvantage is that they are only defined on distributions having finite moments. DP incorporates both the skewness and the kurtosis to characterize the abnormality that exists in the distribution; it is tailored to detect departures from normality in the tails of the distribution as the properties also vary with respect to its bandwidth. DP test for skewness and kurtosis is effective for detecting abnormality caused by asymmetry or non-normal tail heaviness, which outperforms the Shapiro-Wilk tests [121].

The DP Omnibus test, on the other hand, analyzes the skewness and the kurtosis of the data with the Gaussian distribution, and then compares these values with those expected from a normal data set. The difference is then squared, and the sum of squares result is then used to

calculate a p-value. If a population of a random variable X is normally distributed, its density function will be:

$$f(x) = \frac{1}{\sqrt{2\pi}\sigma} e^{-\frac{1}{2}\left(\frac{x-\mu}{\sigma}\right)^2}$$

(3.1)

where μ and σ are the mean and the standard deviation, respectively. The third and fourth standard moments are given by:

$$\sqrt{b_1} = \frac{E(X-\mu)^3}{[E(X-\mu)^2]^{3/2}} = \frac{E(X-\mu)^3}{\sigma^3}$$

(3.2)

$$b_2 = \frac{E(X-\mu)^4}{[E(X-\mu)^2]^2} = \frac{E(X-\mu)^4}{\sigma^4}$$

(3.3)

where E is the expectation operator and X in this case is an individual IMF. $\sqrt{b_1}$ and b_2 measure skewness and kurtosis, respectively; for a data set with normal distribution, they are 0 and 3, respectively.

D'Agostino and Pearson [120] proposed the test statistic K^2 that combines normalizing transformations of skewness and kurtosis, $Z(\sqrt{b_1})$ and $Z(b_2)$, respectively. The DP test statistic K^2 is given by:

$$DP_i = Z_i^2(\sqrt{b_1}) + Z_i^2(b_2) \ , \ i = 1, 2,\dots, n_D$$

(3.4)

where n_D is the number of selected function (i.e., ten in this case). Each of the transformed sample skewness $Z(\sqrt{b_1})$ test statistic is determined by:

$$Z(\sqrt{b_1}) = \frac{\ln\left(Y_1/\alpha_1 + \sqrt{(Y_1/\alpha_1)^2 + 1}\right)}{\sqrt{\ln(W_1)}}$$

(3.5)

where the corresponding Y_1, α_1, and W_1 are obtained for each function (i.e. for each IMF) given by:

$$Y_1 = \sqrt{b_1} \sqrt{\left(\frac{(n_D+1)(n_D+3)}{6(n_D-2)}\right)} ; \tag{3.6}$$

$$(W_1)^2 = -1 + \sqrt{2\beta_1(\sqrt{b_1})-1} ; \tag{3.7}$$

$$\beta_1(\sqrt{b_1}) = \frac{3(n_D^2 + 27n_D - 70)(n_D+1)(n_D+3)}{(n_D-2)(n_D+5)(n_D+7)(n_D+9)} \tag{3.8}$$

$$\alpha_1 = \sqrt{\frac{2}{W_1^2 - 1}} \tag{3.9}$$

$Z(\sqrt{b_1})$ is a test statistic, which is considered approximately normally distributed under the null hypothesis that the population follows a normal distribution.

Each of the transformed sample kurtosis $Z(b_2)$ test statistic is computed by:

$$Z(b_2) = \frac{1}{\sqrt{4.5A_2}} \left[\left(1 - \frac{2}{9A_2}\right) - \sqrt[3]{\frac{1 - \frac{2}{A_2}}{1 + Y_2\sqrt{2/(A_2-4)}}} \right] \tag{3.10}$$

where

$$A_2 = 6 + \frac{8}{\sqrt{\beta_2(b_2)}} \left(\frac{2}{\sqrt{\beta_2(b_2)}} + \sqrt{1 + \frac{4}{\beta_2(b_2)}} \right) \tag{3.11}$$

$$\sqrt{\beta_2(b_2)} = \frac{6(n_D^2 - 5n_D + 2)}{(n_D+7)(n_D+9)} \sqrt{\frac{6(n_D+3)(n_D+5)}{n_D(n_D-2)(n_D-3)}} \tag{3.12}$$

$$Y_2 = \frac{b_2 - 3(n_D-1)/(n_D+1)}{\left(24n_D(n_D-2)(n_D-3)/(n_D+1)^2(n_D+3)(n_D+5)\right)^{1/2}} \tag{3.13}$$

The normality hypothesis of the data is rejected for large values of the test statistic. Furthermore, according to [120], the K^2 test is approximately chi-squared distributed with two degrees of freedom.

The proposed integration weighted d'Agostino-Pearson (WDP) indicator is determined by [122]:

$$WDP = \frac{\sum_{i=1}^{n_D} \frac{(DP_i)}{\max(DP)} \hat{x}_i}{mean((DP)\hat{x}_i)} \tag{3.14}$$

where n_D is the number of function (i.e., n_D = 10 IMFs in this case).

For the integration of the WDP values for the resulting output signal of the HHT (i.e., IMFs), a large DP number is expected for a faulty bearing since it exhibits higher magnitudes of periodic features. This technique is designed to combine more contributive parts of the signals for representative feature extraction. When DP indicators are realized for all IMF's, the resulting NHHT is determined as weighted IMFs in Equation (3.14). The most distinctive features can be correlated to the highest indicator values among the IMFs. These weighted functions will then be used to recognize the most distinctive IMFs in the developed NHHT technique.

WDP is integrated to estimate the normality measure of the IMFs. When DPs are realized for all functions, the WDP indicator is determined as the maximum output of the WDP-HHT integration corresponding to each IMF. The most distinctive feature functions can be recognized as those with highest DP and WDP values among the IMFs. In implementation, the eM filter is used to enhance bearing related signatures, which is integrated with the NHHT to mitigate random noise and detect bearing detects. The effectiveness of the proposed NHHT technique will be verified experimentally in the following section.

3.2 Performance Evaluation

1) Experimental setup and instrumentations

The experimental setup employed for this work is shown in Figure 3.1. The system is driven by a 2.2 kW induction motor (i.e., 2 Hp), with the speed range from 0.3 Hz to 70 Hz, which is controlled by a speed controller (VFD022B21A). A flexible coupling is utilized to dampen the high-frequency vibration generated by the motor and to accommodate misalignment errors in assembly. Variable load is applied by a magnetic brake system through a bevel gearbox and a belt drive. The ratio between the pulleys on the magnetic brake and the shaft is 1:2; the specified

load torque in the following tests represents the torque value of the magnetic brake. An optical sensor is used to provide a one-pulse-per-revolution signal for shaft speed measurement. Two ball bearings (MB ER-10K) are press-fitted into the bearing housings, which have the following parameters: rolling elements: 8; rolling element diameter: 7.938 mm; pitch diameter: 33.503 mm; and contact angle: 0 deg. The bearing on the left housing is used for testing. Accelerometers (ICP-IMI, SN98697), with sensitivity 10.2 ± 0.1 mV/ (m/s^2), are mounted on the housings to measure vibration signals along the vertical and horizontal directions. Two discs are used to apply extra static radial loads. Considering the structure properties, the signal measured vertically is utilized for analysis in this work, whereas the signal measured from the horizontal direction is used for verification. These vibration and reference signals are fed to a computer for further processing through a data acquisition board (NI PCI- 4472), which has built-in anti-aliasing filters with the cutoff frequency set at half of the sampling rate.
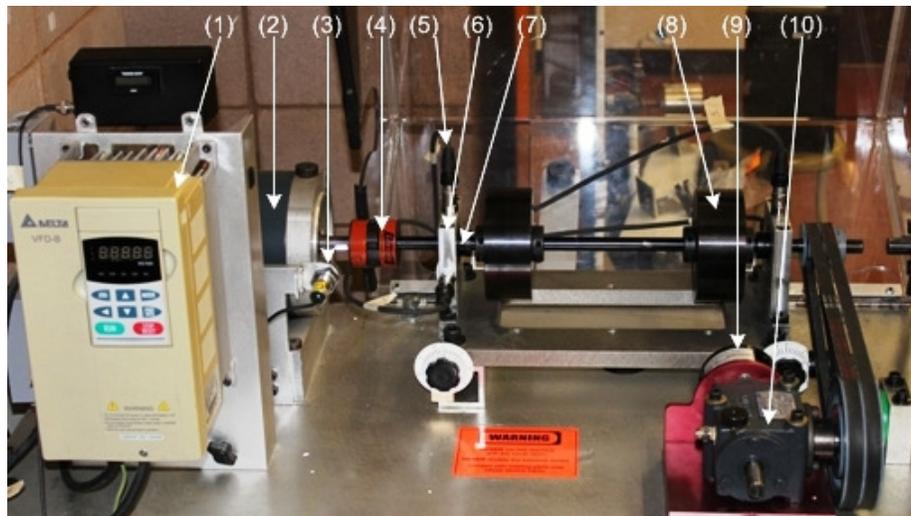
Figure 3.1. Experimental setup: (1) speed control; (2) motor; (3) optical sensor; (4) flexible coupling; (5) ICP accelerometer; (6) bearing housing; (7) test bearing; (8) load disc; (9) magnetic load system; (10) bevel gearbox.

The sampling frequency of the verification test depends on the range of the shaft speed to collect 600~700 samples over each shaft rotation cycle. In this test, four bearing health conditions are considered: healthy bearings, bearings with outer race defect, bearings with inner race defect, and bearings with rolling element defect. Seven different shaft speeds (15, 20, 25, 30, 32, 35, and 40 Hz) and three load levels (1, 2.5, and 5 Nm) are used to test each bearing condition. The outer race defect has a size (area × depth) about 0.2 mm^2 × 0.5 mm; the inner race

defect size is about 0.2 mm^2 × 0.5 mm (area × depth); and the rolling element defect dimension (area × depth) is approximately 0.3 mm^2 × 0.5 mm. Table 3.1 summarizes the characteristic frequencies in terms of shaft speed orders for bearings with different health conditions (e.g., healthy bearings and bearings with defects on the outer races, inner races and rolling elements, respectively), utilizing equations 1.1 to 1.3. All of the related techniques are implemented in MATLAB. The performance comparison is addressed as a part of this research works.

Table 3.1. Characteristic frequencies of MB ER-10K bearing in terms of shaft speed order.

Bearing Condition	Shaft Order
Normal/healthy bearing	1
Outer race defect	3.05
Inner race defect	4.95
Rolling element defect	3.98

2) Validation of eM technique

Firstly, a few examples are used to demonstrate how to implement the proposed morphology-based filtering technique for signal analysis. In order to illustrate the contribution of each SE length to the processed signal (i.e., ϑ_q), Equation (2.16) in Chapter 2 is used to specify each SE length over [0.1, 0.9] with an increment of 0.1 of the cyclic interval. The results are normalized and plotted in Figure 3.2 corresponding to four bearing conditions, with shaft speed of 1800 rpm (or 30 Hz), load torque of 2.5 Nm, and sampling frequency of 20,480 Hz. The proposed eM utilizes all the SE lengths, but it manages the contribution of each filter length according to its weights in Equation (2.16). One example with the SE length $Q = 9$ will be used as an illustration.

For a healthy bearing in Figure 3.2(a), the maximum indicator value corresponds to the fifth length SE length (i.e., $q = 5$) instead of the sixth or seventh SE length as in the classical morphology analysis [106,107]. For the bearing with an outer race defect (Figure 3.2(b)), the maximum ϑ_q corresponds to eighth SE component (i.e., $q = 8$). For the bearing with an inner race defect in Figure 3.2(c), the fifth SE becomes the most contributed one (i.e., $q = 5$). For the bearing with a rolling element (ball) defect (Figure 3.2(d)), the maximum ϑ_q corresponds to the eighth SE component (i.e., $q = 0.8$). On the other hand, it is seen that other order SE length,

41

different from 0.6 or 0.7 as used in [116,117], may also contribute significantly to signal properties in this case.
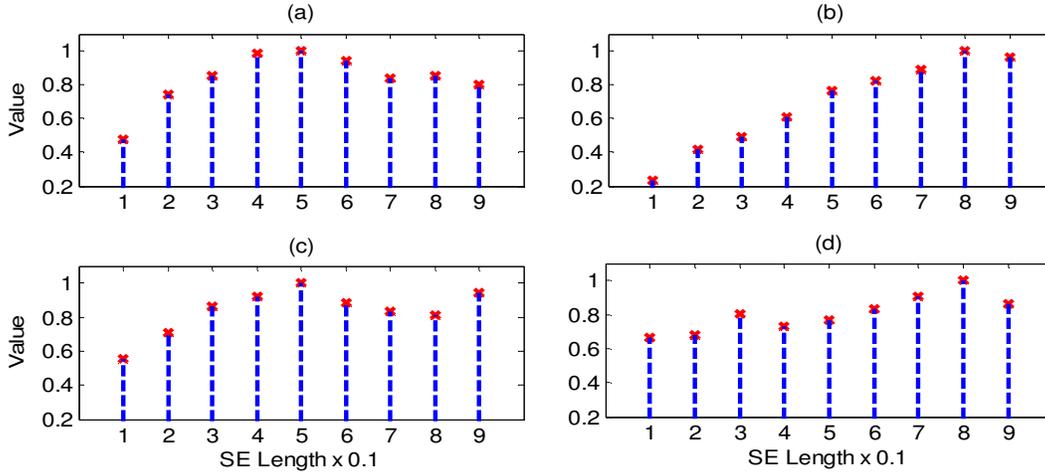
Figure 3.2. Demonstration of normalized MH indicators versus filter length corresponding to different bearing health conditions: (a) healthy bearing; (b) bearing with outer race defect; (c) bearing with inner race defect; (d) bearing with rolling element defect.

3) Implementation of eM for bearing fault detection

In implementing the proposed MH technique (eM plus NHHT [63]) for bearing fault detection, the bearing signal is initially filtered using the appropriate SE length, and then the NHHT will be applied for signal processing and bearing fault detection.

In the MH, the most distinctive IMF will be selected by the use of the normality method as suggested by this author in [63], which has been proven effective in processing non-stationary signals. Correspondingly, the proposed MH technique is realized by:

$$MH_q = \hat{f}_q IMF_w \tag{3.15}$$

where IMF_w is the selected wth IMF and $\hat{f}_q$ is eM filtered signal with the highest indicator ϑ_q of the qth SE length.

The proposed MH technique is implemented in the frequency domain. Firstly, a few examples are used to demonstrate the implementation process. Figure 3.4 shows some of the DP normality measures used in the author's prior work in [63] to process the signals corresponding to four

bearing test conditions with shaft speed of 30 Hz and load torque of 2.5 Nm. The first ten IMFs will be used for MH analysis. For a healthy bearing (Figure 3.3(a)), the most distinguishable IMFs are the first and the sixth IMF (instead of the first and second IMFs as in the classical HHT analysis). Meanwhile, for a bearing with an outer race defect (Figure 3.3(b)), and a bearing with an inner race defect (Figure 3.3(c)), the most distinguishable IMFs are determined to be the first and the second, which is consistent with the classical HHT analysis. On the other hand, for a bearing with a rolling element defect (Figure 3.3(d)), the most distinguishable functions become the first and third IMFs. From Figure 3.3, it can be noted that higher order IMFs (higher than 2) may also contribute significantly to signal properties in this case.
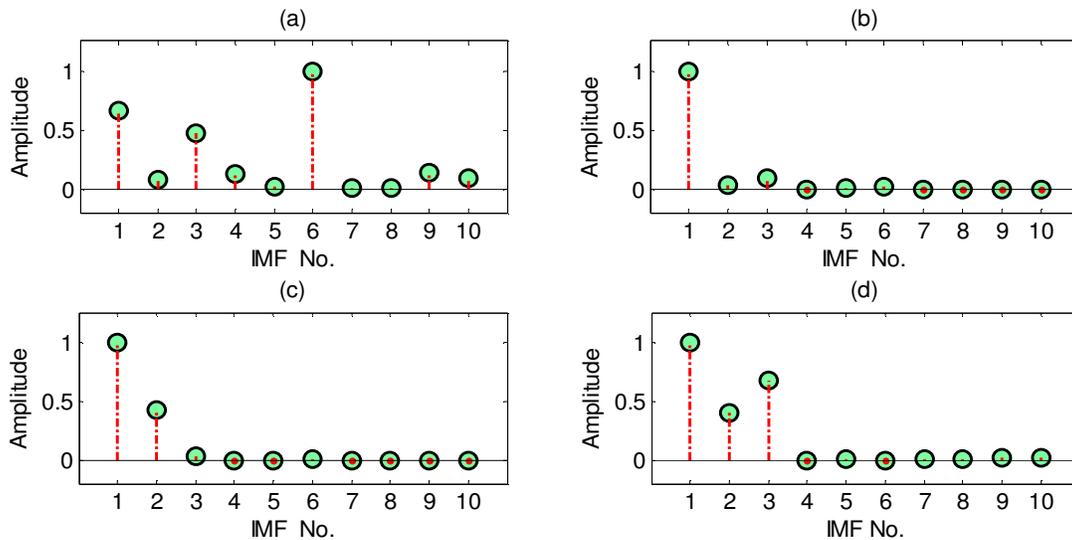
Figure 3.3. Demonstration of normalized d'Agostino-Pearson normality indicators used in [53] versus IMF scales corresponding to filtered signal of different bearing health conditions: (a) healthy bearing; (b) bearing with outer race defect; (c) bearing with inner race defect; (d) bearing with rolling element defect.

Figures 3.4(a)-3.4(d) show part of the collected vibration signals corresponding to different bearing conditions. Although some impulses could be recognized from these vibration signatures such as in Figures 3.4(b), 3.4(c), and 3.4(d), it is difficult to diagnose bearing health conditions based only on these original vibration patterns. The corresponding frequency spectrums for these signals are plotted in Figures 3.4(e)-3.4(h), respectively. It can be seen that the bearing health condition(s) cannot be detected reliably based only on spectral analysis only, especially for complex bearing systems containing non-stationary signals.
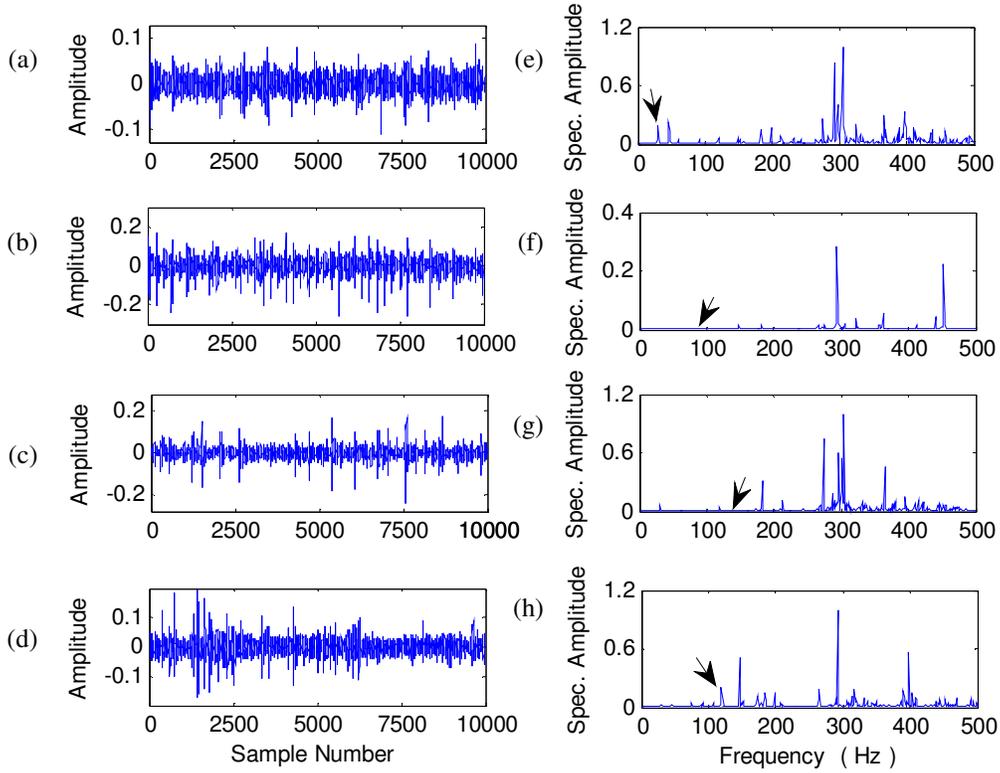
Figure 3.4. Spectral maps of the vibration signals presented in (a, b, c, d) for bearings with different conditions using frequency analysis (e, f, g, h) for: a healthy bearing (a, e); a bearing with outer race defect (b, f); a bearing with inner race defect (c, g); and a bearing with rolling element defect (d, h). Arrows indicate the bearing characteristic frequency.

4) Evaluation of the proposed MH

The effectiveness of the proposed MH technique is compared to some related techniques available in the literature for bearing fault detection. Specifically, the processing results from the classical HHT method using the first two IMFs, designated as HHT, are provided. To examine the effectiveness of the proposed eM filter, two related techniques are used for comparison: the HHT utilizing the eM filter designated as eM-HHT, and the HHT without using the proposed eM filter but applying a constant flat SE length of 0.6, designated as CHT.

(1) Condition Monitoring of a Healthy Bearing

The bearings with healthy conditions were tested first. Figure 3.5 shows an example of the processing results using the related techniques. In this case, the bearing characteristic frequency is $f_r = 30$ Hz. Examining these power spectral graphs, the bearing characteristic frequency can be

identified by each technique. Comparing Figure 3.5(a) (MH), Figure 3.5 (b) (MHT), and Figure 3.5(c) (CHT), it is noticeable that the proposed eM filter can denoise the signal properly and improve signal-to-noise ratio. On the other hand, although the HHT in Figure 3.5(d) can recognize the shaft speed f_r, its spectral maps contain more noise components due to leakage, which may reduce the reliability for online bearing health condition monitoring.
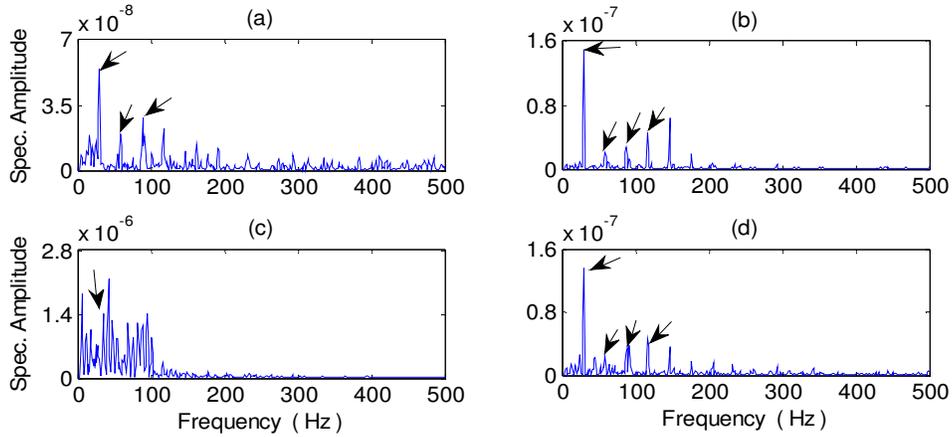
Figure 3.5. Comparison of processing results for a healthy bearing using the techniques of: (a) MH; (b) MHT; (c) CHT; and (d) HHT. Arrows indicate the characteristic frequency and its harmonics.

(2) Outer race fault detection.

When a defect occurs on the fixed ring race of a bearing (the outer race in this case), its defect-induced impulses and resonance modes do not change over time. In this case, the characteristic frequency is $f_{OR} \approx 91$ Hz. Figure 3.6 shows the processing results using the related techniques. It is seen that the proposed MH (Figure 3.6(a)) outperforms not only the MHT (Figure 3.6(b)) with higher magnitude of characteristic frequency components, but also the CHT (Figure 3.6(c)) and HHT (Figure 3.6(d)); its defect frequency and its harmonics dominate the spectral map. The main reason is due to its effective information processing capability, using the suggested normality measure in NHHT and the proposed eM filtering technique.
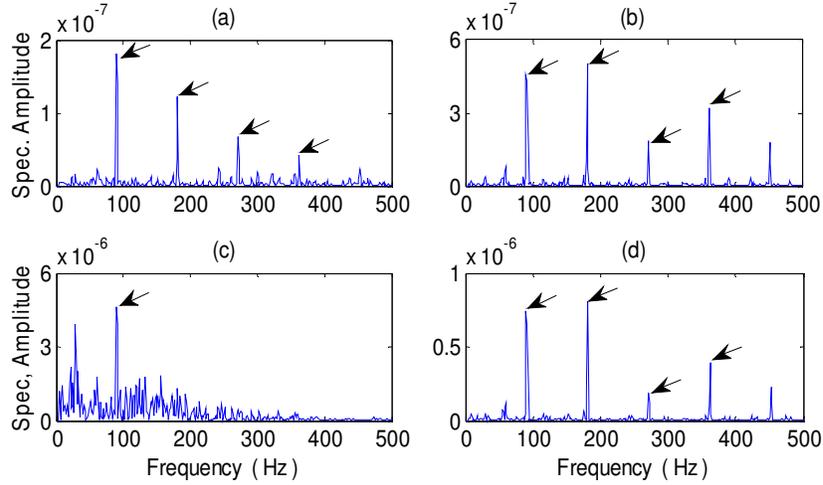
Figure 3.6. Comparison of processing results for a bearing with an outer race defect using the techniques of: (a) MH; (b) MHT; (c) CHT; and (d) HHT. Arrows indicate the characteristic frequency and its harmonics.

(3) Inner race fault detection.

The detection of fault on the rotating inner race is more challenging than the detection of fault on the outer race, because its resonance modes usually vary over time. In this case, the characteristic frequency $f_{IR} \approx 148$ Hz. Processing results using the related techniques are shown in Figure 3.7. It is seen that the proposed MH (Figure 3.7(a)) outperforms the MHT (Figure 3.7(b), the CHT (Figure 3.7(c)), and the HHT (Figure 3.7(d)), due its more efficient denoising processing. It can be seen that defect-related signatures on the maps of the CHT (Figure 3.7(c) and HHT (Figure 3.7(d)) do not dominate the spectra, which can generate false diagnostic results. In the case of the MHT (Figure 3.7(b)), the second harmonic of f_{IR} becomes lower in magnitude than that in Figure 3.7(a), which can mitigate the redundant information for diagnosis.

46
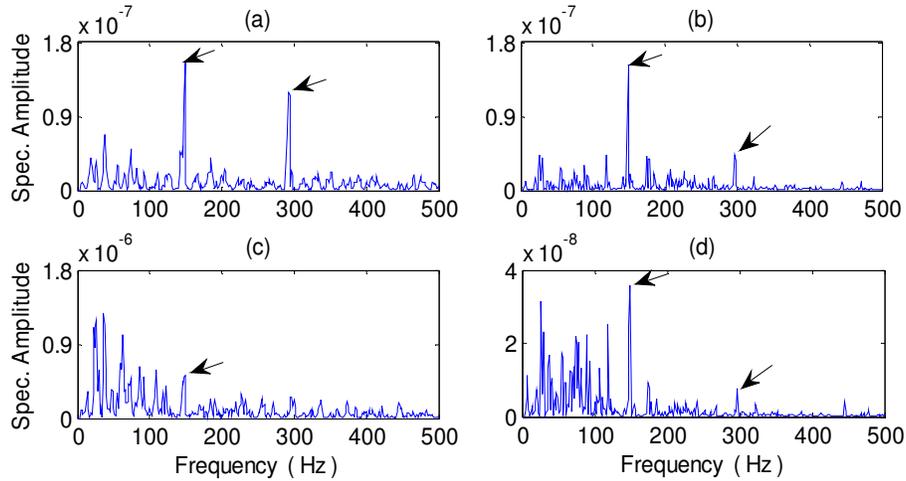
Figure 3.7. Comparison of processing results for a bearing with an inner race defect using the techniques of: (a) MH; (b) MHT; (c) CHT; and (d) HHT. Arrows indicate the characteristic frequency and its harmonics.

(4) Rolling element fault detection.

The detection of fault on a bearing rolling element (ball in this case) could be the most challenging task in bearing fault detection. This is because a ball rolls along different directions (it also slides), and its resonance modes change over time. In this case, the characteristic frequency is $f_{BD} \approx 119$ Hz. Figure 3.8 shows the processing results using the related techniques. It is seen that the proposed MH (Figure 3.8(a)) outperforms other related methods for this fault detection, thanks to its efficient filtering and IMF integration strategies. It can mitigate disturbance and extract distinctive diagnostic features more effectively, which is important for non-stationary signal analysis. The characteristic frequency components of MHT (Figure 3.8(b)), CHT (Figure 3.8(c)), and HHT (Figure 3.8(d)) do not dominate their respective spectral maps, which may lead to false or missed alarms, especially in automatic online machinery health condition monitoring.
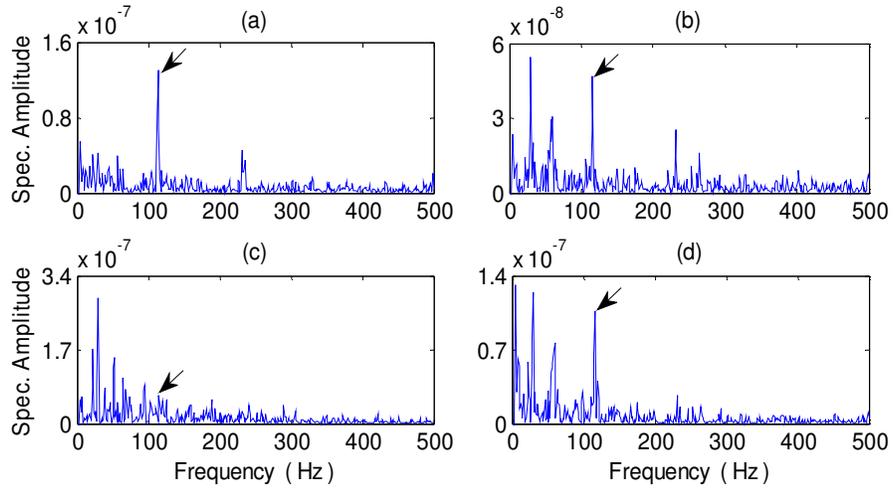
Figure 3.8. Comparison of processing results for a bearing with a rolling element defect using the techniques of: (a) MH; (b) MHT; (c) CHT; and (d) HHT. Arrows indicate the characteristic frequency and its harmonics.

Chapter 4

Integrated Hilbert Huang Transform (iHT) Technique for Bearing Fault Detection Under Controlled Conditions

As stated in the introduction, there are several approaches for bearing fault detection. In the traditional way, the fault is predicted by examining the characteristic spectral features on the frequency spectrum. Different from the traditional FT, which decomposes the signal into a series of sinusoidal functions, the Hilbert Huang transform (HHT) is undertaken based on the intrinsic mode functions (IMFs) performed by the empirical mode decomposition (EMD) [111]. Nevertheless, it has some application limitations as discussed in Introduction section. In this chapter, a new technique, namely integrated HHT (iHT), is proposed for bearing fault detection, under controlled conditions without interference from gear systems. The iHT is used to extract bearing representative features for diagnostic purposes. Its effectiveness will be verified experimentally by comparing its performance to other related techniques.

4.1 The Proposed iHT Technique

This proposed iHT technique is different from the MH in Chapter 3, which applied an information entropy-based measure with NHHT to integrate IMF information for HHT analysis. This new iHT technique firstly determines the weight of each IMF in terms of its contribution to bearing health condition. A linear normality indicator of each IMF is estimated using the Jarque-Bera (*JB*) goodness-of-fit test, which is a measure of departure from normality. Next, the information content of each IMF is determined to provide a non-linear measure of the IMF contribution towards the related bearing health conditions as it does not depends on the orientation of the information space. The linear *JB* and the non-linear information are integrated to process IMFs in order to improve fault detection accuracy.

The normal or Gaussian distribution is the most frequently used distribution method in modeling bearing data [132]. In bearing fault detection, the classical skewness and kurtosis coefficients have some disadvantages, such as a zero breakdown value and their sensitivity to outlying noise [133]. For example, a single outlier can make the estimate fluctuate significantly,

rendering the diagnostic results difficult to interpret. Another disadvantage is that they are defined on distributions with finite moments only. To solve these problems, the *JB* test will be performed for data analysis in this study.

1) JB Goodness-of-Fit test

The *JB* is a parametric hypothesis test. It determines if the null hypothesis of composite normality is reasonable regarding the population distribution of the observed data Z, at a given significance level *β*. The *JB* test can detect normality with the help of asymmetry or non-normal tail measurements [134]; it is also recognized as more effective than other related normality tests such as Shapiro-Wilk and Anderson-Darling [135].

The *JB* test has the following two hypotheses:

1) Null hypothesis: Z is normal with unspecified mean and variance;

2) Alternative hypothesis: Z is not normally distributed.

The *JB* is a 2-sided test of composite normality to estimate the population mean and variance. The test is based on estimates of the sample skewness and kurtosis of the normalized data. Under the null hypothesis, the standardized 3rd and 4th moments are asymptotically normal, and the test statistic has a Chi-square distribution with two degrees of freedom. The *JB* test is usually undertaken with small sample sizes [132], expressed as:

$$JB_i = \frac{N}{6}S_i^2 + \frac{N}{24}(K_i - 3)^2 \qquad (4.1)$$

where N is the sample size; S_i and K_i are the skewness and kurtosis values of the ith IMF, respectively [132,133].

2) Mutual information

Mutual information (MI) is used to measure the correlation between variables [135]. Different from the general autocorrelation function as well as the statistical normality analysis, MI takes into account non-linear correlations. In general, it is less sensitive to the size of the partition elements, and is relatively easier to implement.

MI is a measure from information theory first introduced by Shannon in the context of digital communication [134,135]. It represents the uncertainty about one random variable given knowledge of another random variable, or the amount of information that one random variable contains about another random variable. MI is symmetric and represents the reduction in the uncertainty of one random variable due to the knowledge of another. MI equals zero if the two random variables are independent, and equals infinity if there exists a functional relationship between them. A MI-based indicator will be proposed in this work to select the most distinguishable IMFs for bearing fault detection.

As illustrated in Figure 4.1, consider two information spaces, $H(F_1)$ and $H(F_2)$, of the random variables, F_1 and F_2, with probability distributions of D_1 and D_2, respectively. Joint entropy, $H(F_1, F_2)$, represents the joint probability distribution of F_1 and F_2, where F_1 and F_2 represent the demodulated signals x and $\hat{x}$ obtained from the collected signal, using the Hilbert analysis of Equation 3.7 (Chapter 3), respectively. The proposed MI will use joint probability and product probability to determine the correlation between two variables:

$$I(F_1, F_2) = H(F_1) + H(F_2) - H(F_1, F_2) \tag{4.2}$$

$I(F_1, F_2)$ can be considered as the relative entropy between joint probability distribution D_j, and product distribution D_p, such that:

$$I(F_1, F_2) = \sum_{f_1 \in F_1, f_2 \in F_2} D_j(f_1, f_2) \log_{10}\left(D_p(f_1, f_2)\right) / [D_1(f_1) D_2(f_2)] \tag{4.3}$$

where the product distribution D_p is defined by the product of two random variables having two known distributions: $D_p = D_1 D_2$.
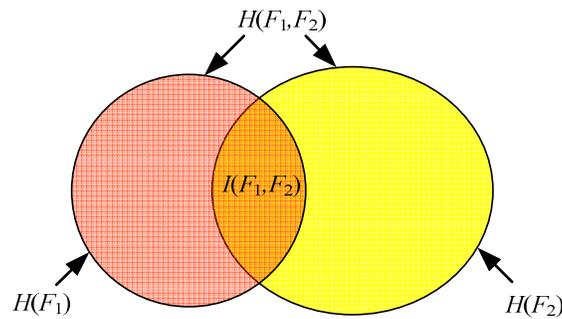
Figure 4.1. Illustration of the relationship between entropy $H(F_1)$ (left circle); $H(F_2)$ (right circle); mutual information $I(F_1, F_2)$ (intersection area); and joint entropy $H(F_1, F_2)$.

From Equation (4.2), it is seen that the maximum MI can be achieved by either maximizing the dataset information (or entropies) $H(F_1)$ and $H(F_2)$, or by minimizing the joint entropy $H(F_1, F_2)$. $I(F_1, F_2)$ is usually sensitive to the changes in the intersection region of the overlap statistics [134]. Since MI takes into account the joint distribution information, it will be more efficient than the general joint entropy in measuring information similarity [135]. If the random variables F_1 and F_2 are independent, the joint probability distribution D_j becomes the product distribution: $D_j = D_p$.

MI represents the relative information contained in datasets F_1 and F_2 over the joint information $H(F_1, F_2)$. If the probability of overlap space from two distributions remains the same, MI is constant regardless of the orientation of distributions $H(F_1)$ and $H(F_2)$. That is, MI is dependent on the overlap information, but independent of the orientations of the constitute spaces $H(F_1)$ and $H(F_2)$.

3) The proposed iHT for bearing fault detection

JB and *MI* are integrated as *JM* to estimate the similarity between signals, corresponding to each IMF:

$$JM_n = a_n\,(JB) \times b_n\,(MI) \tag{4.4}$$

where a_n and b_n are coefficients corresponding to the nth IMF that are application dependent.

In this case, the coefficients a_n and b_n are selected as unity for simplicity. The most distinctive feature functions will be chosen (i.e., those with the highest JM_n indicator values among the IMFs), which are considered to contain maximum correlation information (or minimum entropy), which can be used to recognize the most distinctive IMFs in the proposed iHT analysis.

When *JM* indicators are realized for each IMF, the resulting iHT will be determined as:

$$iHT_i = \sum_i^n (JM \times \hat{x}_i)_i \tag{4.5}$$

These weighted functions are then be used to recognize the most distinctive IMFs in the developed iHT technique. One novelty of the proposed iHT is its automatic selection and implementation of those IMF's that contain more characteristic information of signal properties

that can represent the bearing health conditions, in this case. The effectiveness of the proposed iHT technique will be verified experimentally in the following section.

4.2 Verification of the Effectiveness of the Proposed iHT Technique

The effectiveness of the proposed iHT technique, including the realization of the IMF integration method, will be verified in this subsection using the same experimental setup as illustrated in Figure 3.2.

1) Evaluation of performance

(1) iHT implementation.

The following example demonstrates the implementation procedures of the proposed iHT technique. Figure 4.2 shows some *JM* results corresponding to four bearing health conditions with shaft speed of 1800 rpm (or 30 Hz) and load torque of 3.5 Nm. The first ten IMFs (i.e., $n = 10$) are used for HHT analysis. For a healthy bearing (Figure 4.2 (a)), the most distinguishable IMFs are the first and sixth IMFs, rather than the first and second IMFs, as in the classical HHT analysis. For a bearing with an outer race defect (Figure 4.2(b)), the most distinctive functions are the first and second IMFs. For a bearing with an inner race defect (Figure 4.2(c)), the most distinguishable IMFs become the first and second IMFs, which is consistent with the classical HHT analysis. For a bearing with a rolling element defect (Figure 4.2(d)), the most distinguishable functions become the first and third IMFs. On the other hand, it is seen that some higher order IMFs, other than the first and second IMFs, may also contribute significantly to signal properties, in this case.
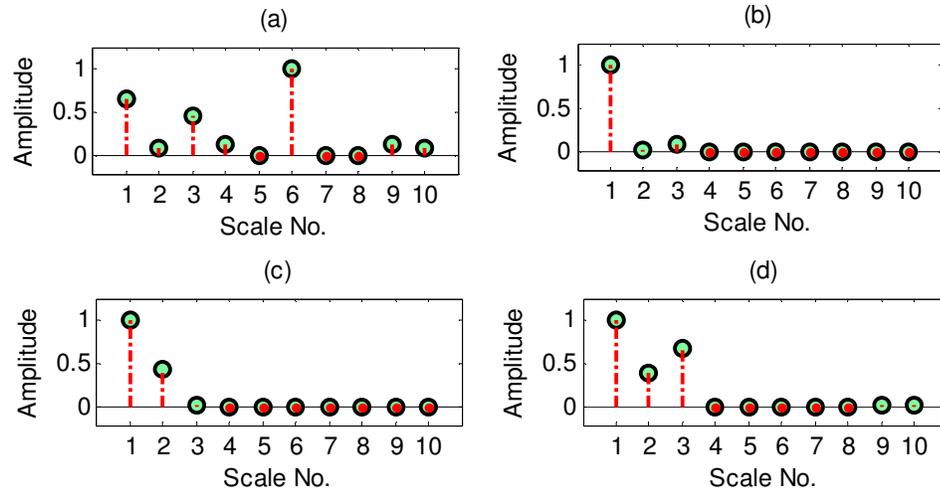
Figure 4.2. Demonstration of normalized *JM* indicators versus IMF scales corresponding to different bearing health conditions: (a) healthy bearing; (b) bearing with outer race defect; (c) bearing with inner race defect; and (d) bearing with rolling element defect.

To compare the performance of the proposed iHT, the processing results from the commonly-applied HHT method, using the first two IMFs, designated as HHT, are provided. Furthermore, the processing results from the WT are also applied (designated as WT); the complex Morlet Wavelet is used in the WT.

Figure 4.3 shows parts of the collected vibration signals corresponding to different bearing conditions. Although some impulses could be recognized from these vibration signatures such as in Figures 3.4(b), 3.4(c), and 3.4(d), it is difficult to diagnose bearing health conditions based solely on these original vibration patterns, especially for complex bearing systems with non-stationary signals.
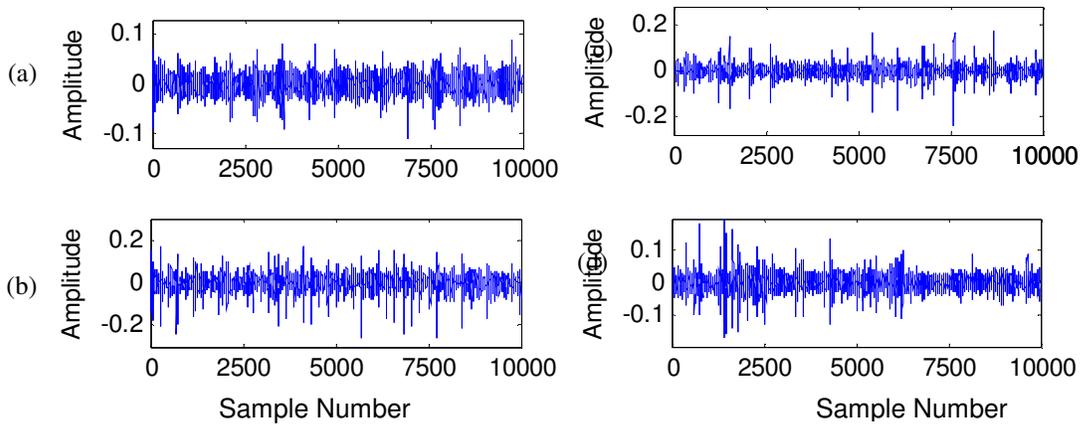
Figure 4.3. Vibration signal for different bearing conditions: (a) healthy bearing; (b) bearings with outer race defect; (c) bearings with inner race defect; and (d) bearings with rolling element defect.

(2) Healthy bearing condition monitoring.

Firstly, the bearings with healthy conditions are tested. Figure 4.4 shows the processing results in terms of power spectrums using the related techniques. In this case, the bearing characteristic frequency is 30 Hz. Examining these power spectral graphs, the bearing characteristic frequency can be identified by each technique. Comparing Figure 4.4(c) (iHT), Figure 4.4(a) (WT), and Figure 4.4(b) (HHT), the proposed iHT technique provides the best performance in enhancing the shaft speed information (with higher magnitude). iHT can also recognize several shaft harmonics, but with very low magnitudes than the shaft speed. Although the WT in Figure 4.4 (a) and HHT in Figure 4.4(b) can recognize the shaft speed, their spectral maps contain more noise components due to reasons such as leakage, which may reduce the reliability for bearing health condition monitoring.
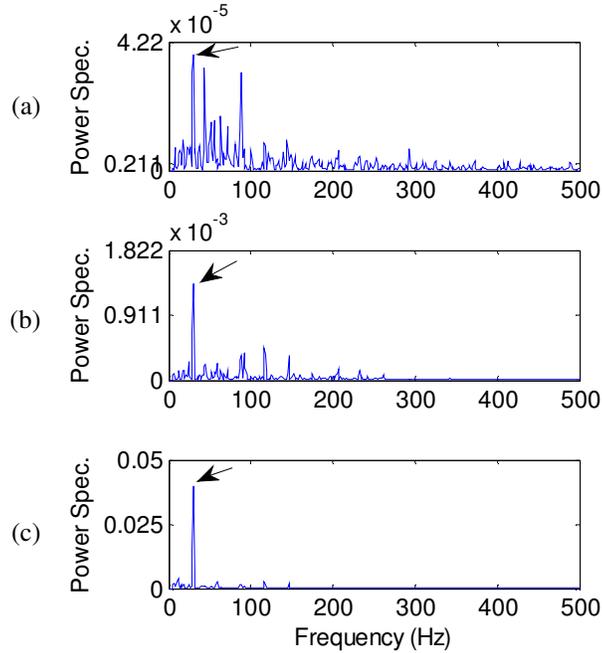
Figure 4.4. Comparison of processing results for a healthy bearing using the techniques of: (a) WT; (b) HHT; and (c) iHT. Arrows indicate the characteristic frequency.

(3) Outer race fault detection.

As stated before, when a defect occurs on the fixed ring race of a bearing (the outer race in this case), its defect-induced resonance modes do not change over time. In this case, the characteristic frequency is f_{OR} = 91 Hz. Figure 4.5 shows the processing results using the related methods. It is seen that the proposed iH (Figure 4.5(c)) outperforms not only the WT (Figure 4.5(a)) with higher magnitude of characteristic frequency components, but also the HHT (Figure 4.5(b)) with the defect frequency and its harmonics dominating its spectral map. The main reason is due to its effective information processing using the proposed *JM* normality method.
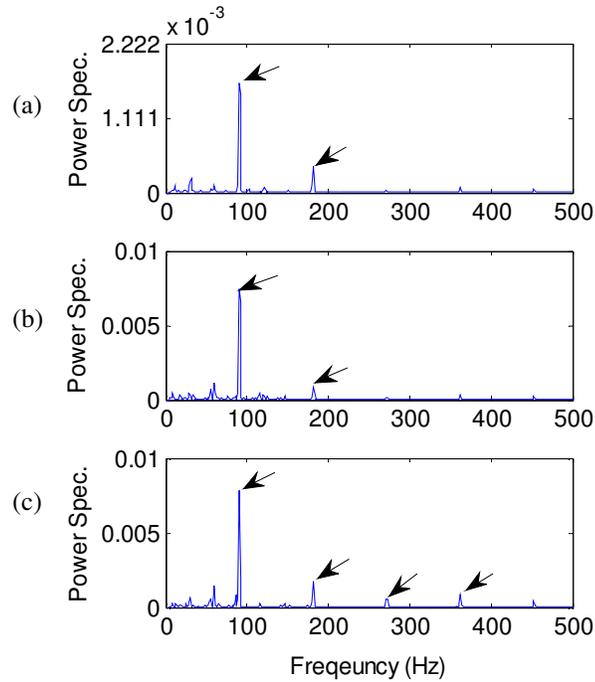
Figure 4.5. Comparison of processing results for a bearing with an outer race defect using the techniques of: (a) WT; (b) HHT; and (c) iHT. Arrows indicate the characteristic frequency and its harmonics.

(4) Inner race fault detection.

The detection of a fault on rotating elements is considered more challenging than the detection of fault on the outer race, as discussed in Chapter 3. In this case, the characteristic frequency $f_{IR} =$ 148 Hz. Processing results using the related methods are shown in Figure 4.6. Similarly, the proposed iHT (Figure 4.6(c)) outperforms both the WT (Figure 4.6(a)) and the HHT (Figure 4.6(b)) due to its efficient information processing strategy.
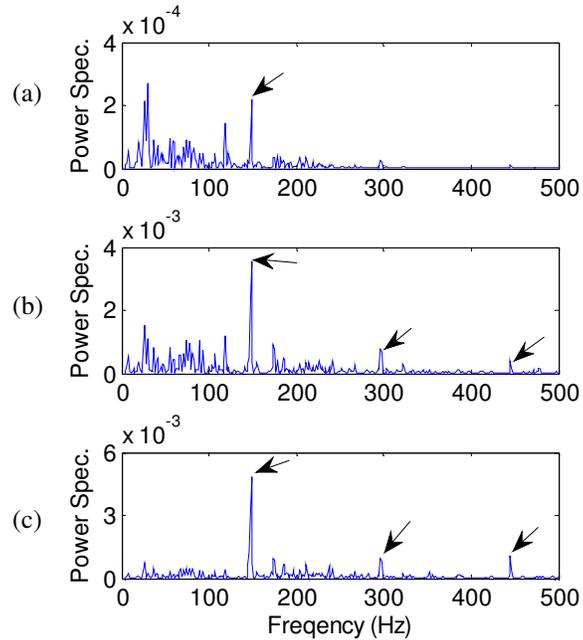
Figure 4.6. Comparison of processing results for a bearing with an inner race defect using the techniques of: (a) WT; (b) HHT; and (c) iHT. Arrows indicate the characteristic frequency and its harmonics.

(5) Rolling element defect detection.

The detection of a fault on the rolling element is considered the most challenging task in bearing fault detection. This is because the rolling element rotates along different directions (it also slides), and its resonance modes change over time. In this case, the characteristic frequency is f_{BD} = 119 Hz. Figure 4.7 shows the processing results using the related methods. It is clear that the proposed iHT (Figure 4.7(c)) gives the best diagnostic results due to its efficient *JM* information integration strategy. The characteristic frequency components of WT (Figure 4.7(a)) and HHT (Figure 4.7(b)) do not dominate their spectral maps, which may lead to false or missed alarms, especially in automatic online machinery health condition monitoring.

58
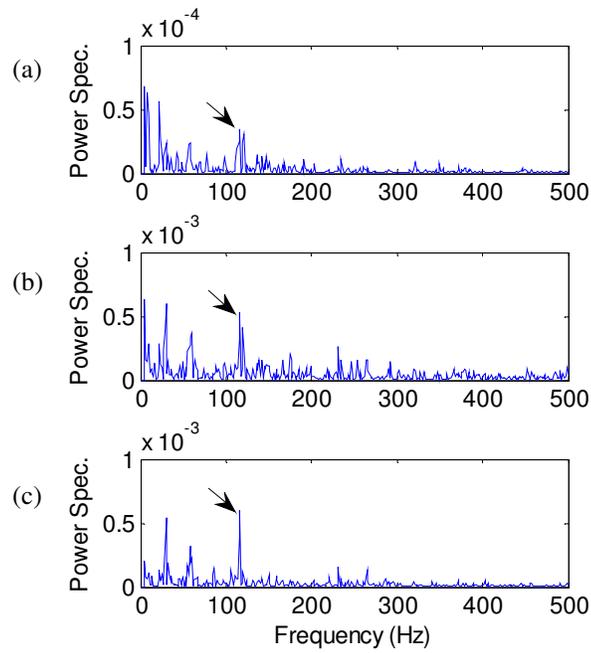
Figure 4.7. Comparison of processing results for a bearing with a rolling element defect using the techniques of: (a) WT; (b) HHT; and (c) iHT. Arrows indicate the characteristic frequency.

Chapter 5

Fault Detection of Bearings in Gearboxes

5.1 Gearbox Signal Analysis

1) Gear mesh frequencies

As discussed in Chapter 1, for a gearbox (gear system) consisting of multiple pairs of gear trains, the gear mesh frequency (MF), f_{gm}, is calculated by:

$$f_{gm} = N_T f_{r,} \tag{5.1}$$

where N_T is the number of teeth on the gear, and f_r is the rotating speed of the gear.

If a gear system is healthy, its gear vibration signal spectrum will be dominated by the gear MF components. Even when the gear speed and load are constant, there exists a varying force in gear meshing operations, and the contact stiffness will vary periodically depending on the position of contact on the tooth's surface [137,138]. The varying force will excite a vibration at the tooth MF and its harmonics [139,140].

2) Gear fault detection using time synchronous average (TSA) filtering

TSA is a signal averaging process over some number of cycles, synchronous with the running speed of a specific gear in the gearbox [141,142]. The TSA allows the vibration signature of the gear of interest to be separated from the other vibration signals. In implementation, the vibration signal is divided into many segments with the help of a once-per-revolution reference; the vibration that is periodic with the gear rotation will be recognized. The averaged result represents the signal average for one revolution of the shaft [141]. Successful application of the TSA requires a constant frequency deterministic component.

TSA signal is determined by

$$x_S[n] = \frac{1}{R}\sum_{r=1}^{R} x_c[n+(r-1)N] \tag{5.2}$$

where $x_c[n]$ is the collected vibration signal over R revolutions, each revolution is consisting of N number of data samples, $n = 0,1, \ldots, N$-1.

In practice, a vibration signal from rotating machinery contains small frequency variations, even when operating at a nominally constant speed. The use of interpolation and resampling is essential to reduce the effect of shaft speed variations [143]. The resulting signal is known as the signal average. Nevertheless, a major drawback of TSA is the loss of distribution or autocorrelation information, which could contain representative features used for fault detection [148,149].

There are several techniques available in the literature for gear fault detection. Amplitude modulation is analyzed according to the overall residual signal after employing a multi-bandstop filter to remove the gear meshing vibration; the damage-related signature could be recognized [147]. The phase modulation analysis is based on the analytical TSA signal average $x_S[n]$, because using a multi-bandstop filter to compute the overall residual signal can result in additional phase distortion.

3) Bearing fault detection in a gearbox

When a bearing component is damaged, each time a roller (ball) rolls over the defect location, an impulsive force occurs that causes resonances of the bearing and/or support structures. The response decay depends on dampening properties in the support structures. As discussed in Equations (1.1)-(1.3) in Chapter 1, each type of bearing defect is characterized by a specific characteristic frequency depending on the bearing component where the defect occurs, the bearing geometry, and the speed at which the shaft rotates [151,152]. Often, a succinct bearing vibration component will be present in the early stages of failure. The major problem in detecting the incipient bearing fault is that these fault-related representative features are usually weak in magnitude, and are masked by the higher-level gear vibration [153,154]. The objective of the research work in this chapter is to propose a new technique to demodulate bearing fault-related features for gearbox vibration signals.

As discussed in Chapter 1, currently there are techniques that can be used to separate bearing signals from gear vibration. When resonance sparse decomposition (RSD) is used in

fault detection, RSD is usually in combination with some post-processing methods to further process the results. These post-processing methods include statistical analysis, genetic algorithm, soft-computing tools, or filtering process [92-96]. However, post-processing performs subjective feature amplification, which is usually application-oriented, and less robust in processing nonstationary vibration signals like those generated from a bearing with rotating ring damage plus the effects such as slips of rolling elements and load zone variations [96,97].

To solve the aforementioned RSD limitations, the objective of this work is to propose a new leakage-free RSD (LRSD) technique to demodulate bearing characteristic features from gearbox vibration signals. First, a leakage-free filter is proposed in the frequency domain to remove high energy periodic signals. Second, a novel strategy is suggested to correlate the RSD with the decomposition parameters to facilitate demodulation operation for real-time applications.

5.2 The Proposed LRSD Technique

The proposed LRSD technique will be used to adaptively decompose the vibration signal into transient (bearing) from oscillatory (gear and shaft) components in gearboxes.

The RSD in LRSD is implemented in iterative two-channel filter banks. Its highpass and lowpass filters are specified in the frequency domain for reconstruction. As previously discussed in Section 1.5, the RSD integrates the morphological components analysis (MCA) and Tunable-Q WT (TQWT) to process signals. It has been verified in Chapter 1 that the TQWT can process signals having high-frequency components with short duration, and low frequency components with long duration, which is generally the nature of a gearbox signal [90]. To achieve better results, the Q factor of WT could be chosen according to the oscillatory behavior of the signal. TQWT iteratively applies two-channel high and low filter banks, where the lowpass output of each filter bank is the input to the next filter bank [90,91]. The Q factor can be tuned according to the frequency properties of the input signal. In general, the larger the Q, the better the frequency aggregation of the signal [91]; in contrast, the smaller the Q, the better the time aggregation of the signal and the lower the resonance property. The Q factor of an oscillatory pulse is the ratio of its center frequency to its bandwidth. Alternatively, the oversampling rate (r) (i.e., redundancy) can be defined to represent the decomposition levels (J). The Q factor in

TQWT will be chosen according to the oscillatory behavior of the signal. The theory of TQWT, the selection of Q factor, and other related parameters, are explained next.

5.2.1 Tunable Q wavelet transform (TQWT)

TQWT uses a perfect reconstruction of oversampled filter banks with real valued scaling factors [90]. The Q factor, oversampling rate or redundancy (r), and number of levels (J) are the main parameters of TQWT. For discrete-time signals of finite length, TQWT can be implemented with the FT, as the TQWT is modestly over-completed with iterated two-channel filter banks [91] as discussed next.

1) Signal reconstruction

In order to obtain ideal perfect reconstruction, the frequency response of the lowpass filter and the highpass filter of the input signal $x(n)$ must be selected in such a way that the reconstruction signal $\hat{x}$ is as close as possible to the input signal.

The amplitude frequency response of the lowpass filter, $L(\omega)$, and the highpass filter, $H(\omega)$, are defined by [90,92]:

$$L(\omega) = \begin{cases} 1, & |\omega| \leq (1-\beta)\pi \\ \theta\left(\dfrac{\alpha\pi - \omega}{\alpha + \beta - 1}\right), & (1-\beta)\pi < |\omega| < \alpha\pi \\ 0, & \alpha\pi \leq |\omega| \leq \pi \end{cases} \tag{5.3}$$

$$H(\omega) = \begin{cases} 0, & |\omega| \leq (1-\beta)\pi \\ \theta\left(\dfrac{\alpha\pi - \omega}{\alpha + \beta - 1}\right), & (1-\beta)\pi < |\omega| < \alpha\pi \\ 1, & \alpha\pi \leq |\omega| \leq \pi \end{cases} \tag{5.4}$$

where $\theta = (1/2)(1 + \cos\omega)\sqrt{2 - \cos\omega}$ is the Daubechies frequency response with two vanishing moments during reconstruction of the transition bands of the lowpass and highpass filters [90]. Ideal perfect reconstruction requires that the selected filters must meet the criteria: $|L(\omega)|^2 + |H(\omega)|^2 = 1$. In addition, the respective lowpass and highpass scales α and β [90,91] are determined by $\beta = 2/(Q+1)$ and $\alpha = 1 - \beta/r$. It is critical that, $\alpha + \beta > 1$, in order to ensure the

WT will not be overly redundant when the filter banks are oversampled [90-92], which will lead to localized filter responses for reconstruction.

2) Lowpass and highpass scaling properties

The sampling rate of the signal depends upon the selection of scaling parameters. Lowpass and highpass scaling α and β used in filters of TQWT are explained next.

A) *Lowpass Scaling*. Lowpass scaling is defined as the frequency domain scaling, which preserves the low frequency contents of the signal. With sampling parameter α and input signal sampling rate f_s, the output sampling rate will be αf_s. Lowpass scaling block diagram is illustrated in Figure 5.1(a), whereas Figure 5.1(b) and Figure 5.1(c) show the lowpass scaling with $\alpha < 1$ and $\alpha > 1$, respectively.

When $0 \leq \alpha \leq 1$, the lowpass scaling with parameter α is defined as:

$$Y(\omega) = X(\alpha\omega), \quad |\omega| \leq \pi \tag{5.5}$$

When $\alpha \geq 1$, lowpass scaling is defined as:

$$Y(\omega) = \begin{cases} X(\omega/\alpha), & |\omega| \leq \alpha\pi \\ 0, & \alpha\pi < |\omega| \leq \pi \end{cases} \tag{5.6}$$

As demonstrated in Figure 5.1(b), the lowpass scaling preserves the signal behavior around DC (i.e., when $\omega = 0$) [90,91].
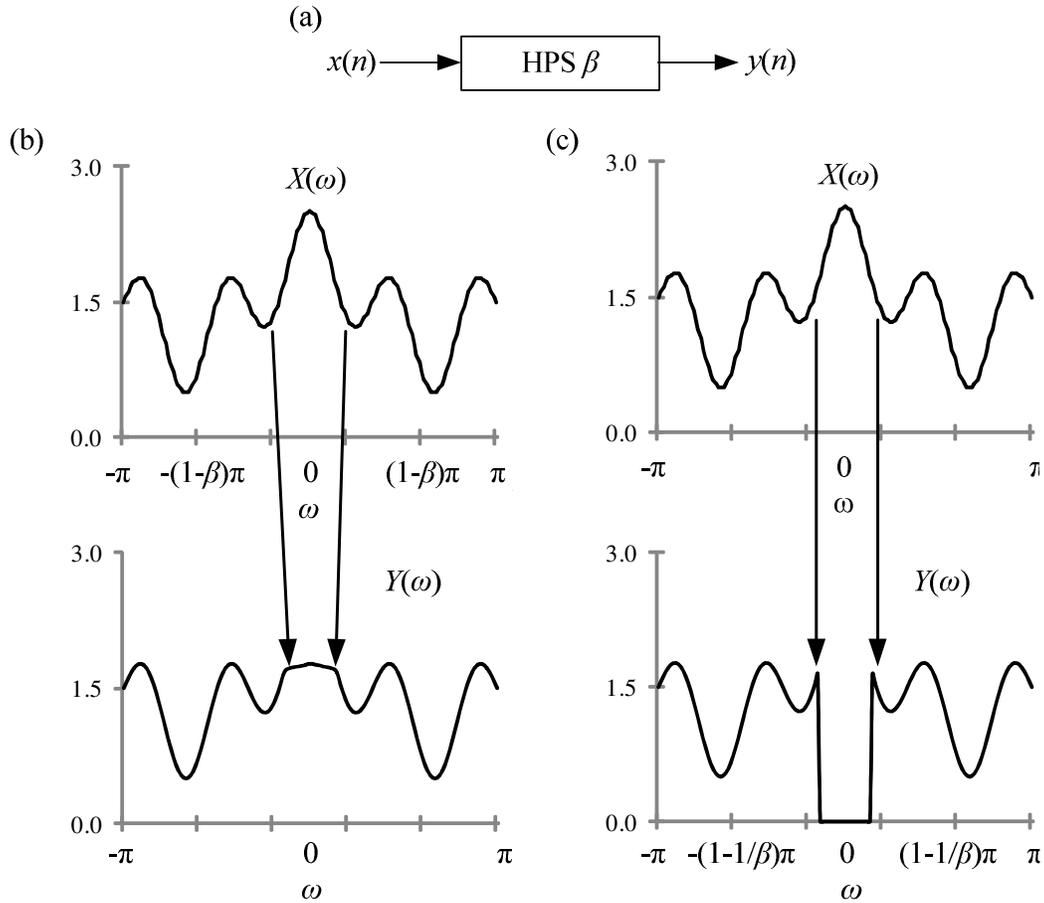
Figure 5.1. Lowpass scaling for continuous signal: (a) lowpass scaling block diagram; (b) lowpass scaling with $\alpha <$ 1; (c) lowpass scaling with $\alpha > 1$.

Similarly, for lowpass scaling of a discrete signal with the length of N, N_0 is the length of the output signal and $x(n)$ is an N point signal for $0 \leq n \leq N\text{-}1$ [90].

If $N_0 < N$ and both N_0 and N are even, then the lowpass scaling is defined as:

$$Y(k) = X(k), \ 0 \leq k \leq N_0/2 - 1 \tag{5.7a}$$

$$Y(N_0/2) = X(N/2) \tag{5.7b}$$

$$Y(N_0 - k) = X(N - k) \, , \ 1 \leq k \leq N_0/2 - 1 \tag{5.7c}$$

where $X(k)$ and $Y(k)$ denote the discrete FT of input and output signals, respectively. When $N_0 < N$, the scaling reduces the sampling rate. If $N_0 > N$, scaling increases the sampling rate and lowpass scaling is defined as [90,91]:

$$Y(k) = X(k), \qquad 0 \le k \le N_0/2 - 1 \qquad (5.8a)$$

$$Y(k) = 0, \qquad N/2 \le k \le N_0/2 - 1 \qquad (5.8b)$$

$$Y(N_0/2) = X(N/2) \qquad (5.8c)$$

$$Y(N_0 - k) = 0, \qquad N/2 \le k \le N_0/2 - 1 \qquad (5.8d)$$

$$Y(N_0 - k) = X(N - k), \quad 1 \le k \le N/2 - 1 \qquad (5.8e)$$
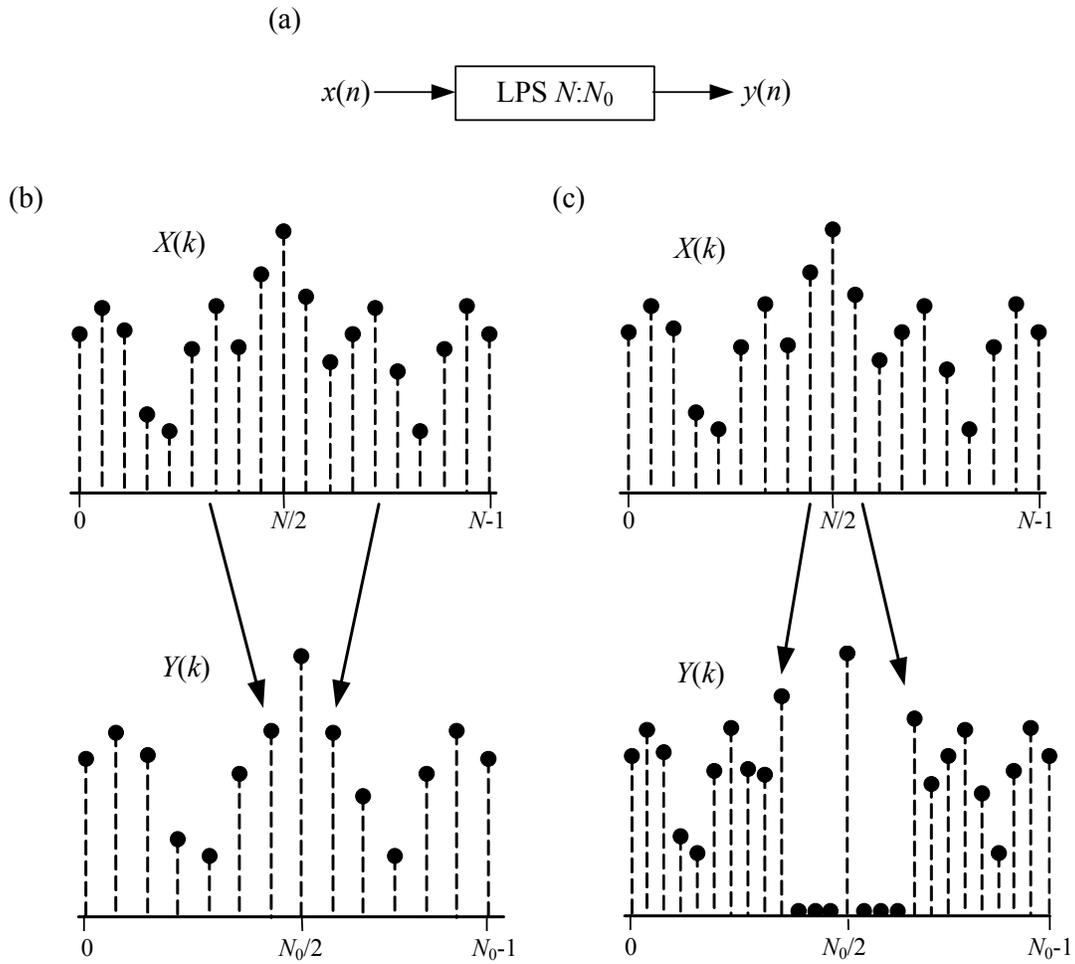
Figure 5.2. Lowpass scaling for discrete signal (a) block diagram; (b) lowpass scaling when $N_0 < N$; (c) lowpass scaling when $N_0 > N$.

B) *Highpass Scaling*. Contrary to lowpass scaling, highpass scaling preserves the high frequency content of the signal. With highpass scaling parameter β and input sampling rate f_s, the output signal has a sampling rate of βf_s [91-92].

When $0 < \beta \leq 1$, highpass scaling with parameter β is expressed as:

$$Y(\omega) = \begin{cases} x(\beta\omega + (1-\beta)\pi), & 0 < \omega < \pi \\ x(\beta\omega - (1-\beta)\pi), & -\pi < \omega < 0 \end{cases} \tag{5.9}$$

When $\beta \geq 1$, highpass scaling is defined as:

$$Y(\omega) = \begin{cases} 0, & |\omega| < (1-1/\beta)\pi \\ x(\beta\omega + (1-\beta)\pi), & (1-1/\beta)\pi < \omega < \pi \\ x(\beta\omega - (1-\beta)\pi), & -\pi < \omega < -(1-1/\beta)\pi \end{cases} \tag{5.10}$$

Figure 5.3(a) shows the block diagram of the highpass scaling, where as Figure 5.3(b) and 5.3(c) illustrates the highpass scaling for $\beta < 1$ and $\beta > 1$, respectively. Highpass scaling preserves the signal behavior when $\omega = \pi$ (i.e., the Nyquist frequency), and thus $Y(\pi) = X(\pi)$.

In implementation, TQWT is first applied on rows and then on columns of the signal.
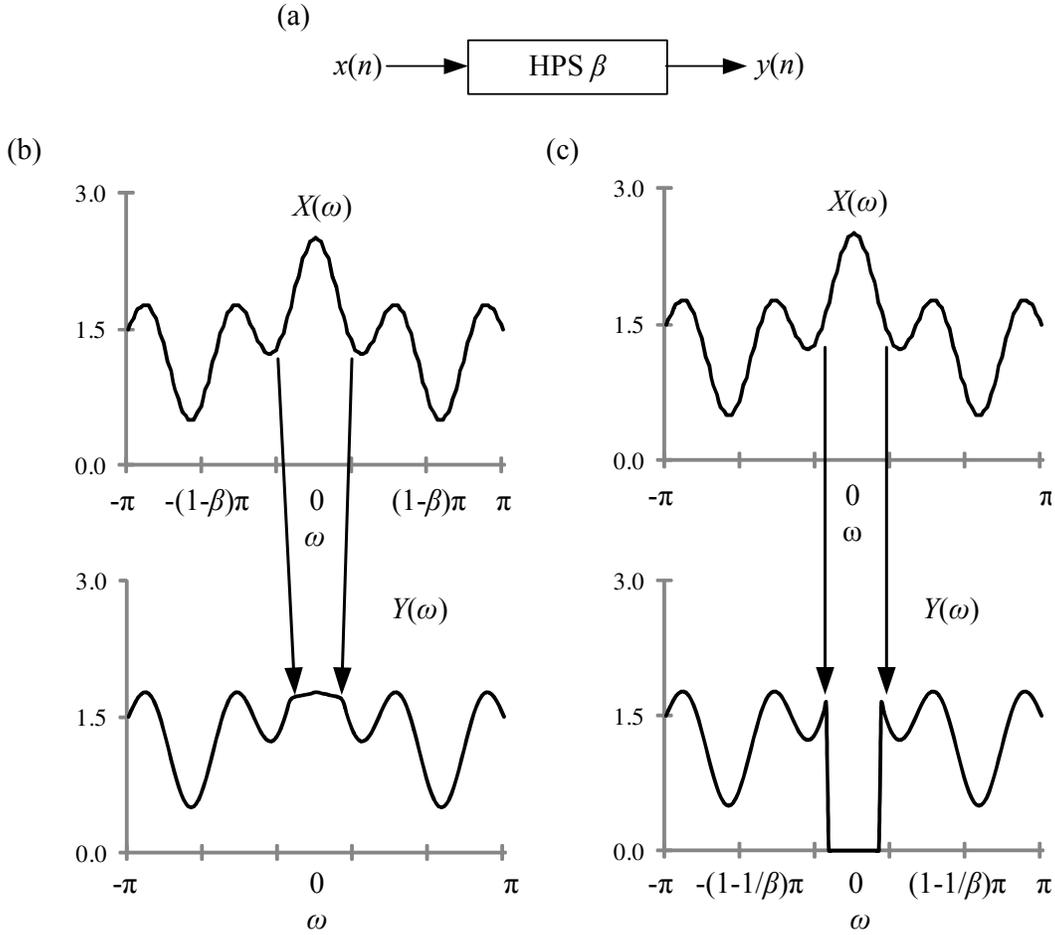
Figure 5.3. Highpass scaling for continuous signal: (a) block diagram of highpass scaling; (b) highpass scaling with $\beta < 1$; (c) highpass scaling with $\beta > 1$.

Similarly, for lowpass scaling of a signal, suppose N and N_1 are the lengths of the input signal and the output signal, respectively; let $x(n)$ be an N point signal for $0 \leq n \leq N - 1$. If $N_1 < N$, and both N_1 and N are even, then highpass scaling N_1 as in [90,91] will be:

$$Y(0) = X(0) \tag{5.11a}$$

$$Y(N_1/2 - k) = X(N/2 - k), \quad |k| \leq N_1/2 - 1 \tag{5.11b}$$

If $N_1 > N$, highpass scaling N_1 is defined as [90,91]:

$$Y(0) = X(0) \tag{5.11a}$$

$$Y(k) = 0, \ 1 \leq k \leq (N_1 - N)/2 \tag{5.11b}$$

$$Y(N_1/2 - k) = X(N/2 - k), \ |k| \leq N/2 - 1 \tag{5.11c}$$

68

$$Y(N_1 - k) = 0, \; 1 \le k \le (N_1 - N)/2 \qquad\qquad (5.11\text{d})$$

Highpass scaling can preserve the spectrum of the signal around the Nyquist frequency (corresponding to the discrete FT coefficient with index $k = N/2$) as illustrated in Figure 5.4.
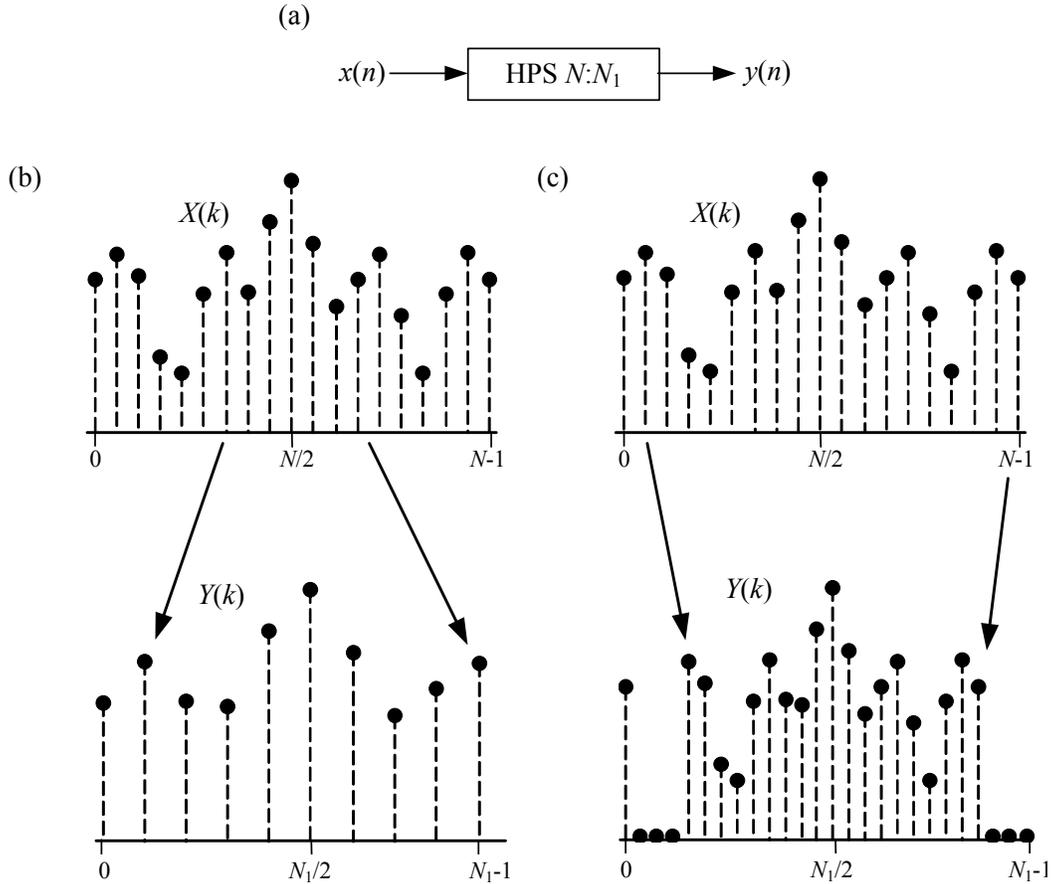
Figure 5.4. Highpass scaling for discrete signal: (a) block diagram; (b) highpass scaling with $N_1 < N$; (c) highpass scaling with $N_1 > N$.

3) Main parameters of TQWT

Given a sampling rate f_s at the level j, the following parameters are used to design TQWT filters:

- Select an oversampling rate (redundancy), $r \ge 1$; ($r \ge 3$ is used in this work).

- Specify Quality factor $Q \ge 1$; ($Q \ge 2$ is used in this work).

If r is close to 1, the WT function will not be localized (i.e. converged) in time, resulting in excessive undesirable ringing [90,92]. The two-channel filter bank will be oversampled by a factor $(\alpha + \beta) \times r$, which should be greater than 1. The redundancy, r, is defined as $r = \beta / (1 - \alpha)$.

For the desired Q factor of the level j, frequency response is determined by [90]:

$$Q = \frac{\omega_c}{BW} = \frac{2 - \beta}{\beta} \tag{5.12}$$

With the Q factor, a maximum number of J levels, denoted as J_{max}, is defined to facilitate the related computation [91,92]:

$$J_{max} = round\left(\log\left(\frac{N}{4(Q+1)}\right) \bigg/ \log\left(\frac{Q+1}{(Q+1) - 2/r}\right) \right) \tag{5.13}$$

where J_{max} is rounded to the nearest integer.

The center frequency at each level j frequency band response is non-zero in the interval $(\omega_1 - \omega_2)$ where [90-92]:

$$\omega_1 = (1-\beta) \, \alpha^{j-1} \, \pi \tag{5.14a}$$

$$\omega_2 = \alpha^{j-1} \, \pi \tag{5.14b}$$

The center frequency ω_c in rad/sample at level j is the average of ω_1 and ω_2 [90,91]:

$$\omega_c = \frac{1}{2}(\omega_1 + \omega_2) = \alpha^{j\frac{2-\beta}{2\alpha}} \tag{5.15}$$

The center frequency at level j will be:

$$f_c = \alpha^{j\frac{2-\beta}{4\alpha}} f_s \tag{5.16}$$

where f_s is the input signal sampling rate in Hz.

The bandwidth (BW) of the frequency response producing subband j is half the width of the interval over which the frequency response is non-zero [90,92]:

70

$$BW = \frac{1}{2}(\omega_2 - \omega_1) = \frac{1}{2}\beta\alpha^{j-1}\pi \qquad (5.17)$$

4) Two-channel filter banks for continuous signal

Figure 5.5 illustrates a block diagram of two-channel filter banks for a continuous signal. The sampling rate for lowpass subband signal $v_0(n)$ is αf_s, and for highpass subband signal $v_1(n)$ is βf_s. The scaling parameters α and β should satisfy the conditions $0 < \beta \leq 1$, and $0 < \alpha < 1$ to prevent over redundancy of the WT [90,91]:
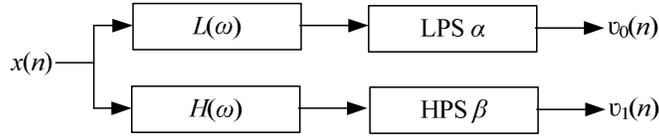
Figure 5.5. Block diagram of two-channel filter banks.

Consider J levels of decomposition, then $J + 1$ subband signals can be formulated in a cell array:

$$\{v_{11}; v_{12}; v_{13}; \ldots, v_{1J}; v_{0J}\} \quad (5.18)$$

where v_{0J} is the $J + 1$ the subband signal having the lowest frequency and the subband signals from v_{11} to v_{1J} are high frequency signals, The number of samples in each subband can be obtained using the following scaling parameters [90]:

$$[\beta f_s N, \alpha\beta f_s N, \alpha^2\beta f_s N; \ldots, \alpha^J\beta f_s N; \alpha^J f_s N] \qquad (5.19)$$

For perfect reconstruction of the signal with well-localized filter responses, the filter bank should be oversampled. At sublevel j of the total J levels TQWT, the lowpass (L_j) and highpass (H_j) filters are defined as:

$$L_j(\omega) = \begin{cases} \prod_{g=0}^{j-1} L(\omega/\alpha^g), & |\omega| \leq \alpha^j\pi \\ 0, & \alpha^j\pi < |\omega| \leq \pi \end{cases} \qquad (5.20)$$

71

$$H_j(\omega) = \begin{cases} H(\omega/\alpha^{j-1})\prod_{g=0}^{j-2} L(\omega/\alpha^g), & (1-\beta)\alpha^{j-1}\pi < |\omega| \le \alpha^{j-1}\pi \\ 0, & |\omega| \le \pi \end{cases} \qquad (5.21)$$

The lowpass subband such as the first stage (υ_{01}) is determined by using lowpass filter $L(\omega)$ and lowpass scaling (LPS α). Similarly, the highpass subband υ_{11} is obtained using $H(\omega)$ and HPS β.

Figure 5.6 illustrates a response example of a two-channel filter bank for $\alpha = 0.7$ and $\beta = 0.5$. It is seen that the two frequency responses are unified in their passbands, and zero in their stopbands. Nevertheless, they are not ideal lowpass and highpass filters because they have the transition bands over the intervals, $(1 - \beta)$ and $(-\alpha\pi \le \omega \le \alpha\pi)$, respectively. The width of the transition band $(\alpha + \beta - 1)\pi$ is exactly the same as that of the filter bank exceeding the critical sampling rate. Therefore, if $\alpha + \beta = 1$, the filter bank is critically sampled, where the transition bandwidth is zero (ideal filters). On the other hand, the time-domain responses of these filters are not properly localized. It is important that the condition of $\alpha + \beta > 1$ is satisfied such that the time-domain responses are well localized. From Figure 5.6(d), it is important to note that the spectrum should cover the overall frequency bandwidth after scaling.
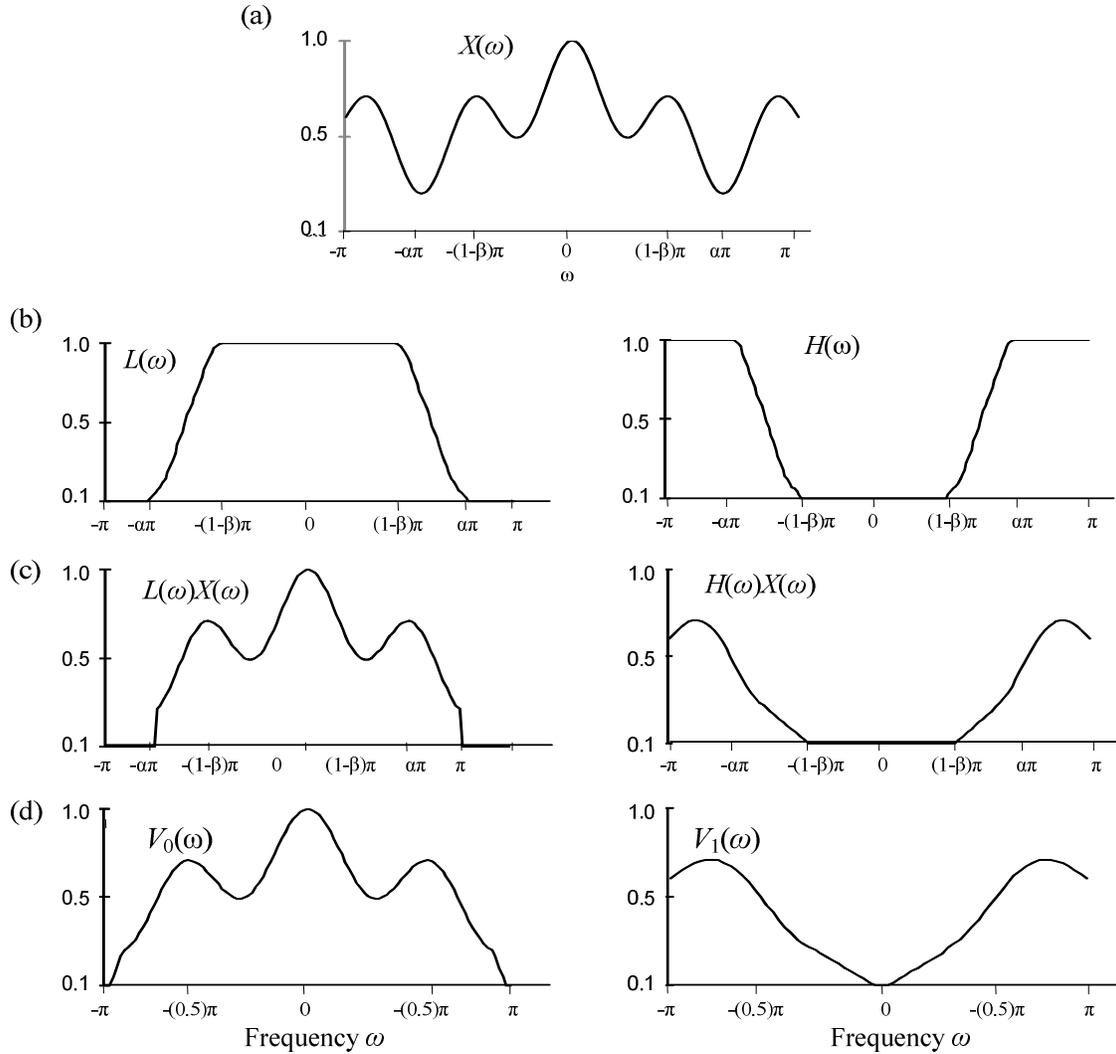
Figure 5.6. Response of two-channel filter banks: (a) FT of input signal; (b) lowpass frequency response $L(\omega)$ and highpass frequency response $H(\omega)$; (c) FT of input signal after filtering; (d); FT after scaling.

5) Two-channel filter banks finite length signal

The TQWT of a finite length signal is implemented by recursively applying the filter bank to its lowpass channel, as illustrated in Figure 5.7. The parameters N, N_0, N_1 must be specified at each level, or $N_0 = \alpha N$ and $N_1 = \beta N$ for lowpass and highpass scaling of the signal of length N, respectively.

73
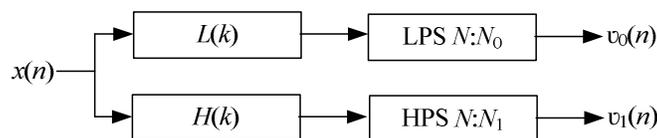
Figure 5.7. Two channel filter banks for discrete signal.

Given signals $v_0(n)$ and $v_1(n)$ with length N_0 and N_1, the implementation of the filter bank for the signal $x(n)$ is as follows [90,91]:

o Compute N point discrete FT of the input signal $x(n)$ to obtain coefficients $X(k)$ for $0 \leq k \leq N_1$-1.

o Perform point-to-point multiplication to get $R_i(k) = X(k)$ and $H_i(k)$, for $i = 0, 1$.

o Take lowpass/highpass scaling on $R_i(k)$ to obtain the discrete FT coefficients $v_i(k)$, $0 \leq k \leq N_i$, for $i = 0, 1$.

o Compute the N_0 point inverse discrete FT of $v_0(k)$ to obtain $v_0(n)$ for $0 \leq n \leq N_0$-1; compute N_1 point inverse discrete FT of $v_1(k)$ to obtain $v_1(k)$.

In designing the filters, N_0 and N_1 should satisfy the following conditions:

$N_0 + N_1 > N$; $N_0 \approx \alpha N$; $N_1 \approx \beta N$.

Figure 5.8 illustrates the response of a two-channel filter bank for a discrete signal, and a three-level WT filter bank is shown in Figure 5.9.
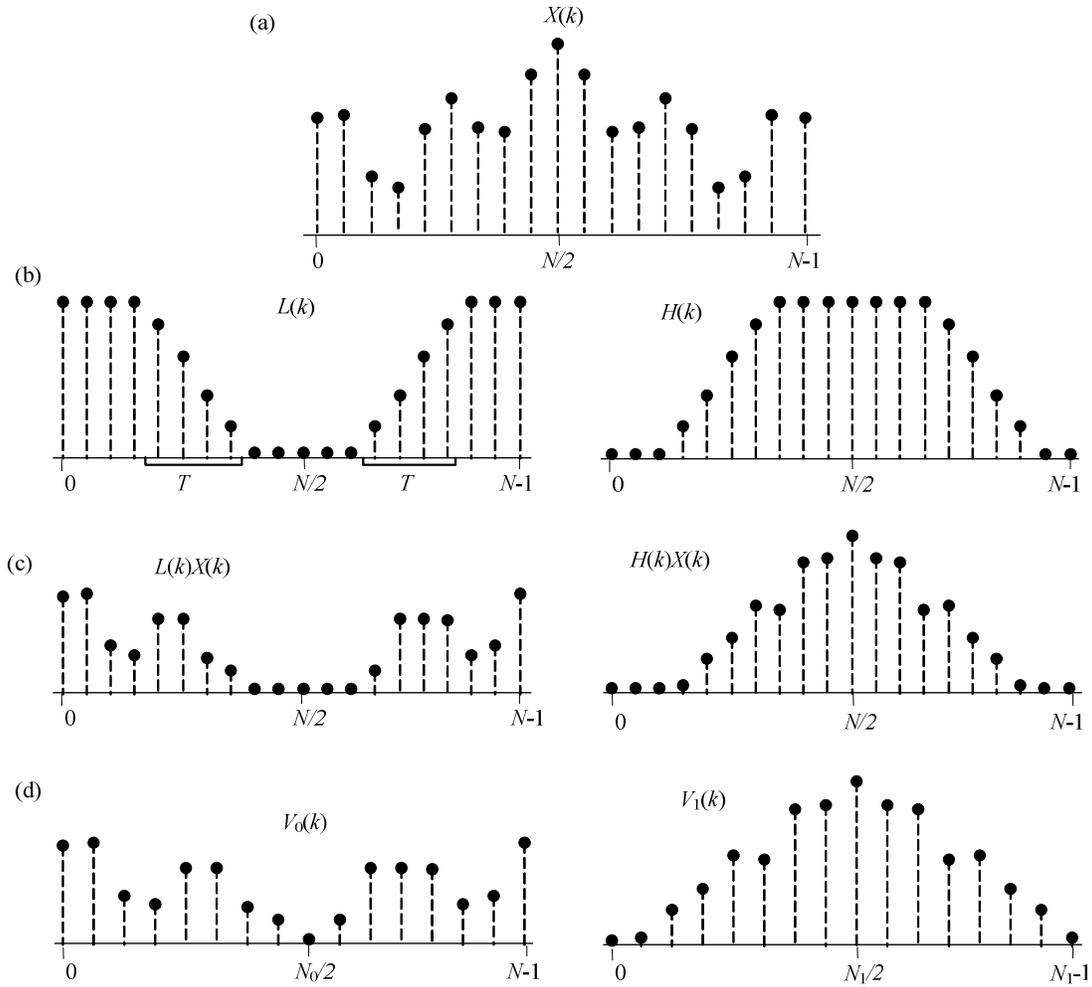
Figure 5.8. The response of a two-channel filter bank for discrete signal: (a) discrete FT of input signal $X(k)$; (b) lowpass $H_0(k)$ and highpass filters $H_1(k)$; (c) discrete FT of input signal after filtering; (d) discrete FT after scaling.
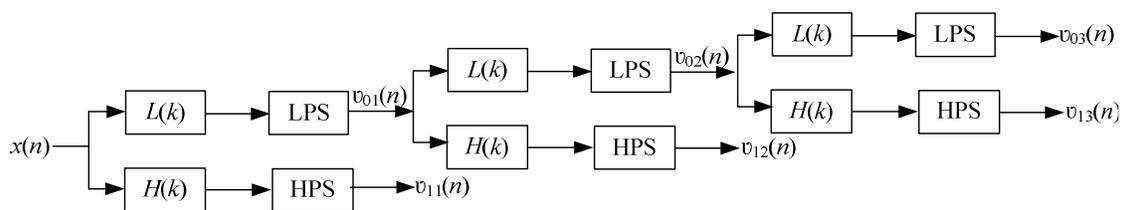
Figure 5.9. Three-level Wavelet filter banks.

LRSD uses the TQWT to obtain the basic function library of high Q and low Q transforms and to calculate the corresponding WT coefficients. The two-channel filter banks are shown in Figure 5.10, where LPS and HPS represent lowpass and highpass filters respectively, L^* and H^* is the conjugate complexes of L and H, respectively. The sampling frequency of

subband signal υ_{0J} is αf_s, and the sampling frequency of υ_{1J} is βf_s, where f_s is the sampling frequency of the input signal $x(n)$.
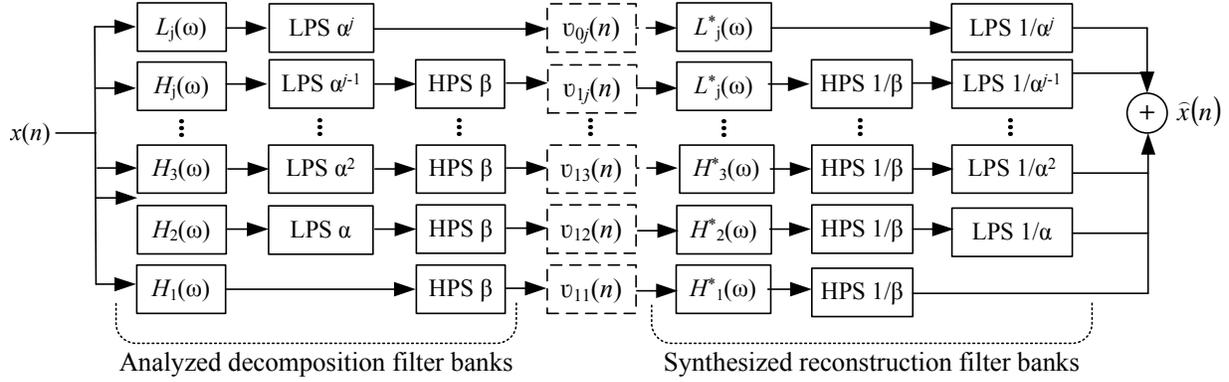
Figure 5.10. Block diagram of the decomposition and the reconstruction filter banks of the input signal $x(n)$.

The TQWT is considered perfectly discrete with moderate completion when it is computed with radix-2 FT [90-92], as discussed next.

A) Radix-2 TQWT

The unitary discrete FT uses powers of two in length to reduce computational cost of the TQWT [90]. The radix-2 TQWT uses radix-2 FT [91]; its assumption is that the length of the signal is the power of two; otherwise, it has to be zero padded. The unitary discrete FT satisfies the Parseval's theorem of signal energy conservation [90,92].

The redundancy of the Radix-2 TQWT and the redundancy r satisfy the following condition [90]:

$$\frac{1}{N}\left(N_0^{(j)} + \sum_{j=1}^{J} N_1^{(j)} \right) < 2r \tag{5.22}$$

After decomposition and reconstruction, it is possible that a sparse representation of the signal using the high Q and low Q factors will separate characteristic signatures of gear and bearing signals [93-97].

5.2.2. Morphological Components Analysis

The sparse representation of the signal is determined by solving the basis pursuit problem using morphological components analysis, expressed in terms of high and low oscillatory components, x_H and x_L, by minimization of the following cost functions [92-97]:

$$x_H = S_H W_1 \tag{5.23a}$$

$$x_L = S_L W_2 \tag{5.23b}$$

where S_H and S_L are the high and low of the TQWT filter banks, respectively; W_1 and W_2 are the coefficients decomposed by [93,94]:

$$J(W_1, W_2) = \frac{1}{2}\|x - S_H W_1 - S_L W_2\|_2^2 + \lambda_1 \|W_1\|_1 + \lambda_2 \|W_2\|_1 \tag{5.24}$$

where λ_1 and λ_2 are the regulation parameters, chosen according to the power distribution of the decomposed resonance components. Equation (5.24) is minimized recursively using some method such as the split augmented Lagrangian shrinkage algorithm, in this case [95-97].

Split augmented Lagrangian shrinkage algorithm uses a viable splitting technique of a constrained problem to conduct unconstrained optimization. Considering Equation (5.24), the unconstrained optimization formulation can be formulated as [156-160]:

$$\min_{W} f_1(W) + f_2(W) \tag{5.25}$$

where:

$$f_1(W) = \lambda_1 \|W_1\|_1 + \lambda_2 \|W_2\|_1 \tag{5.26a}$$

$$f_2(W) = \frac{1}{2}\|x - S^* W\|_2^2 \tag{5.26b}$$

where $S^* = \begin{bmatrix} S_H^*, S_L^* \end{bmatrix}$ and $W = [W_1, W_2]^T$.

Firstly, a splitting variable, $U = [U_1, U_2]^T$, is assigned to the argument of f_1 under the constraint $U = W$, which leads to the following expression:

$$\min_{W,U} f_1(U) + f_2(W) \tag{5.27}$$

Next, the alternating direction method of multipliers [156] is used to update the above equation by:

$$U^{(l+1)} = \arg\min_{U} f_1(U) + \frac{\mu}{2}\left\|U - W^{(l)} - d^{(l)}\right\|_2^2 = \arg\min_{U} \lambda_1\|U_1\|_1 + \lambda_2\|U_2\|_1 + \frac{\mu}{2}\left\|U - W^{(l)} - d^{(l)}\right\|_2^2$$

$$\tag{5.28}$$

$$W^{(l+1)} = \arg\min_{W} f_2(W) + \frac{\mu}{2}\left\|U^{(l+1)} - W - d^{(l)}\right\|_2^2 = \arg\min_{W} \frac{1}{2}\left\|x - S^*W\right\|_2^2 + \frac{\mu}{2}\left\|U^{(l+1)} - W - d^{(l)}\right\|_2^2$$

$$\tag{5.29}$$

$$d^{(l+1)} = d^{(l)} - \left(U^{(l+1)} - W^{(l+1)}\right) \tag{5.30}$$

where l is the iteration index, and μ is the penalty parameter.

In order to minimize Equation (5.28), soft-threshold rule is utilized to find appropriate U, given by $U^{opt} = soft\left(y, \dfrac{\lambda}{\mu}\right)$, where $soft(y, Th) = y \cdot \max\left(0, 1 - \dfrac{Th}{|y|}\right)$; $Th \in \mathfrak{R}_+$ is the threshold; $\mathfrak{R}_+$ is a set of real-valued positive number, $y \in \mathbb{C}$ is any complex-valued number. U is updated by

$$U^{(l+1)} = soft\left(W^{(l)} + d^{(l)}, \frac{\lambda}{\mu}\right) \tag{5.31}$$

Minimizing the convex quadratic function (5.29) can be achieved by:

$$W^{(l+1)} = \left(\left(S^*\right)^T \left(S^*\right) + \mu I\right)^{-1}\left(\left(S^*\right)^T x + \mu\left(U^{(l+1)} - d^{(l)}\right)\right) \tag{5.32}$$

Consider the TQWT:

$$W^{(l+1)} = \frac{1}{\mu}\left(I - \frac{1}{\mu+2}SS^*\right)\left(Sx + \mu\left(U^{(l+1)} - d^{(l)}\right)\right) = \frac{1}{\mu+2}S\left(x - S^*\left(U^{(l+1)} - d^{(l)}\right)\right) + \left(U^{(l+1)} - d^{(l)}\right)$$

$$\tag{5.33}$$

Equation (5.30) is updated by:

$$d^{(l+1)} = W^{(l+1)} - \left(U^{(l+1)} - d^{(l)}\right) = \frac{1}{\mu+2} S\left(x - S^*\left(U^{(l+1)} - d^{(l)}\right)\right) \quad (5.34)$$

Updating Equations (5.31)-(5.34) yields:

$$U^{(l+1)} = soft\left(W^{(l)} + d^{(l)}, \lambda/\mu\right) \qquad (5.35a)$$

$$V^{(l+1)} = U^{(l+1)} - d^{(l)} \qquad (5.35b)$$

$$d^{(l+1)} = \frac{1}{\mu+2} S\left(x - S^* V^{(l+1)}\right) \qquad (5.35c)$$

$$W^{(l+1)} = d^{(l+1)} + V^{(l+1)} \qquad (5.35d)$$

Equation (5.35) is considered the iteration processes of Split augmented Lagrangian shrinkage algorithm that includes splitting variables, alternating direction method of multipliers, and soft threshold [158-161].

5.2.3 Proposed leakage-free filter

The leakage-free filter will be implemented to remove the interference from a periodic signal, such as gear mesh. In general, the weak bearing signals are modulated by the strong gear mesh and shaft vibrations. In order to improve signal-to-noise ratio of the bearing signal that has low energy level with a low Q factor, the strong gear mesh vibration should be filtered out properly. Removing gear MF and its harmonics can reduce J levels and iteration number of the Split augmented Lagrangian shrinkage algorithm needed to separate the vibration signal into two distinct oscillatory components.

A leakage-free filter is implemented in this subsection to reduce interference from the gear meshing and shaft rotations. The filter parameters are chosen based on gear system information such as the number teeth on the gears and the running speed of the shaft. For example, consider a vibration signal measured from a gearbox, $x(t)$, which consists of the shaft signal, $x_s(t)$, gear signal, $x_g(t)$, bearing signal, $x_b(t)$, and noise.

The overall gearbox vibration signal could be expressed as:

$$x(t) = x_s(t) + x_g(t) + x_b(t) + \eta(t) \tag{5.36}$$

where $\eta(t)$ is the weighted white noise.

The periodic shaft signal, $x_s(t)$, can be expressed as:

$$x_s(t) = \sum_{p=1}^{P} B_p \cos\left((2\pi f_r t)p + \theta_p\right) \tag{5.37}$$

where B_p and θ_p are the magnitude and phase of pth shaft harmonic ($P = 5$ in this test), respectively.

The gear signal is also periodic, which can be modeled as the integration of gear MF and its harmonics, expressed as:

$$x_g(t) = \sum_{k=1}^{K} A_k \cos(2\pi k f_{gm} t + \varphi_k) \tag{5.38}$$

where A_k and φ_k are the magnitude and phase of kth gear harmonic, respectively. Gear MF $= f_{gm} = N_T f_r$, f_r is shaft running speed and N_T is the number of teeth of the gear of interest. K is the total number of MF harmonic considered ($K = 5$ in this test).

The leakage-free filter is implemented in the frequency domain. Filtering of the gear MF and its harmonics will be implemented by letting the magnitudes of related stopbands equal 0. If $X(f)$ is the FT of the gearbox signal $x(t)$, set $X(f)$ to zero over the stopbands of $f \in [(k f_{gm} + 1) - 0.5p, (k f_{gm} + 1) + 0.5p]$, the signal residual after this filtering process can be obtained by calculating the real part of the inverse FT:

$$\bar{x}(t) = real\left(F^{-1}(2X(f))\right) \tag{5.39}$$

where F^{-1} is the inverse FT, real is the function that corresponds to the real part of the resulting FT function. Because only a one-sided spectrum is used, a factor 2 is used in Equation (5.39). Using such an effective and leakage-free filtering process, we can avoid perplexing post-processing at each j level signal [93-97], especially if a large J (e.g., 100 levels) is used for analysis.

Figure 5.11 shows some processing results using a simulated gearbox vibration signal with shaft running speed of 20 Hz and gear teeth number of 20 (i.e., $f_{gm} = 400$ Hz). The gear MF and its sidebands are clearly visible in Figures 5.11(a) and 5.11(b), this indicates that gearbox vibration is dominated by strong gear mesh processes. To compare the proposed leakage-free filter to a commonly used multi-band bandstop filter or a classical comb filter. The comb filter is a multi-bandstop Butterworth filter, with a filter order of three; its stop center frequencies are the gear MF and its harmonics; the bandstop is chosen to be $4f_r$ Hz. Test results are provided in Figures 5.11(c) and 5.11(d), whereby leakage can be recognized on the spectral map Figure 5.11 due to filtering distortion. Figures 5.11(e) and 5.11(f) show the signal residual and the related spectral map with the use of the leakage-free filter. It is clear that the results are more accurate with less filtering distortion.
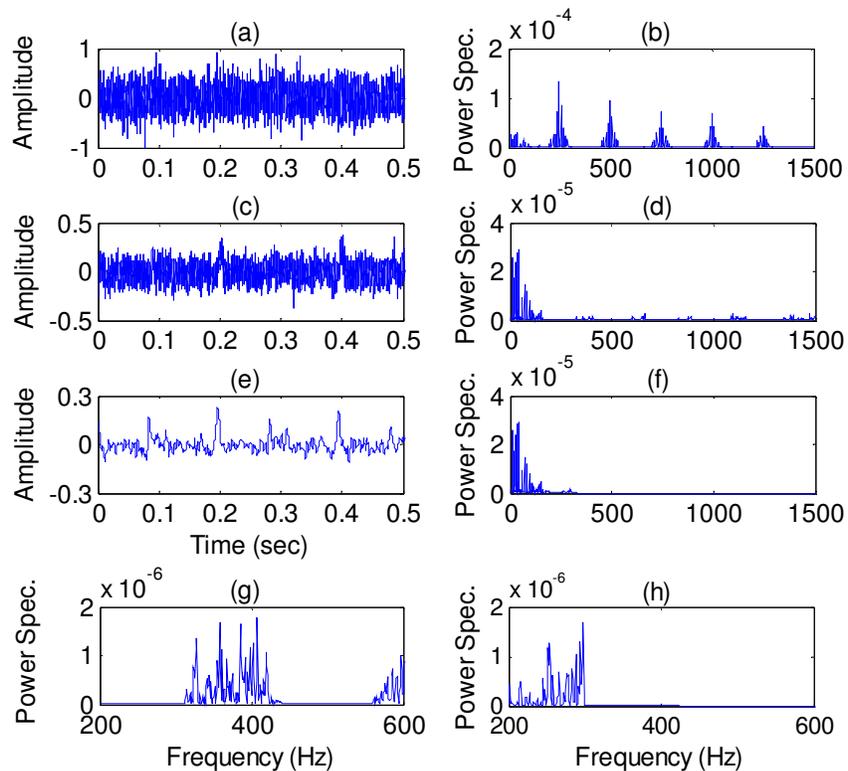
Figure 5.11. Processing results using simulated gearbox signal: (a) gearbox signal; (b) power spectrum of the signal in (a); (c) signal residual after applying comb filter; (d) spectrum of the signal in (c); (e) signal residual after applying leakage-free filtering; (f) power spectrum of the signal in (e); (g) zoom-in of graph (d); (h) zoom-in of graph (f).

5.3. LRSD for Bearing Fault Detection in Gearboxes

In this section, the effectiveness of the proposed LRSD technique is verified, firstly by simulation data, and secondly by real gearbox experimental tests.

5.3.1 Implementation of the proposed LRSD technique

In implementation of the LRSD, two parameters (Q and r) should be chosen properly: Q_1 and r_1 correspond to high resonance frequency (designated as HR) analysis, and Q_2 and r_2 correspond to low resonance frequency (designated as LR) analysis. An example will first be used, based on simulated gearbox vibration signal, to illustrate how to implement the LRSD for bearing fault detection. In this simulation test, levels $J = 100$ are selected. Figures 5.12(a) and 5.12(b) show two HR signals with ($Q_1 = 3$, $r_1 = 10$) and ($Q_1 = 4.5$, $r_1 = 25$); Figures 5.12(c) and 5.12(d) demonstrate two simulated LR signals with ($Q_2 = 2$, $r_2 = 10$) and ($Q_2 = 3.5$, $r_2 = 25$), respectively. Figures 5.12(e) to 5.12(h) correspond to their respective power spectral maps. After comparing the corresponding spectral maps, it can be seen that increasing Q and r has no clear effect on enhancing the characteristic features of the gear MF and its harmonics. On the other hand, the bearing characteristic features (i.e., bearing characteristic frequency $\approx$ 36 Hz in this case) do not dominate the spectrum, which can lead to missed and/or false alarms in automatic (online) gearbox health condition monitoring.
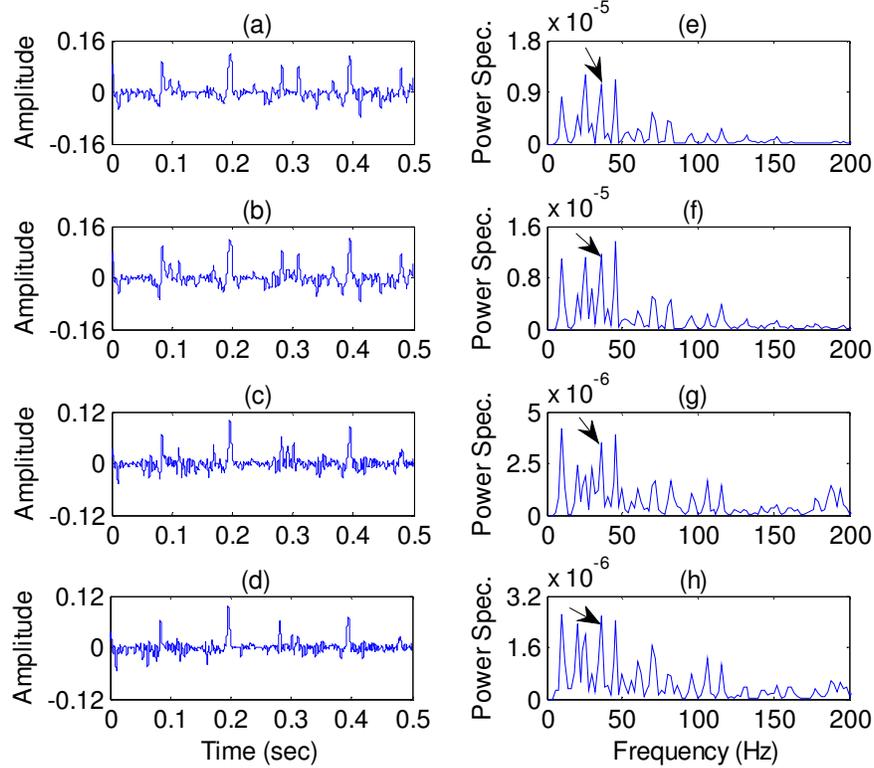
Figure 5.12. RSD processing examples using simulated signals: (a) HR time signal ($Q_1 = 3$, $r_1 = 10$); (b) HR time signal ($Q_1 = 4.5$, $r_1 = 25$); (c) LR time signal ($Q_2 = 2$, $r_2 = 10$); (d) LR time signal ($Q_2 = 3.5$, $r_2 = 25$); figures (e) to (h) correspond to their respective power spectra. Arrows indicate bearing characteristic frequency.

Next, we apply the proposed leakage-free filter to remove periodic signals from the gear meshing (i.e., MF and its harmonics). The signal residual is illustrated in Figure 5.13(a), whose spectral map is shown in Figure 5.13(f). It is seen from Figure 5.13(f) that the gear MF and its harmonics have been removed from the spectrum; however, bearing characteristic features are still buried by other stronger vibration signatures. The RSD is applied to compute the HR and LR resonance responses of the signal residual. If $J_1 = J_2 = 100$, $Q_1 = 3$, 4.5, $r_1 = 10$, 25 and $Q_2 = 2$, 3.5, $r_2 = 10$, 25, the time signals and spectral maps for HR resonance responses are illustrated in Figures 5.13(b), 5.13(c), 5.13(g) and 5.13(h), respectively. LR time and spectra are demonstrated in Figures 5.13(d), 4.13(e), 4.13(i) and 4.13(j), respectively. From these results, it is seen that the health-related characteristic features of the bearing still do not dominate the resulting spectra due to interference from the shaft running speeds, as indicated in Figures 5.13(i) and 5.13(j).
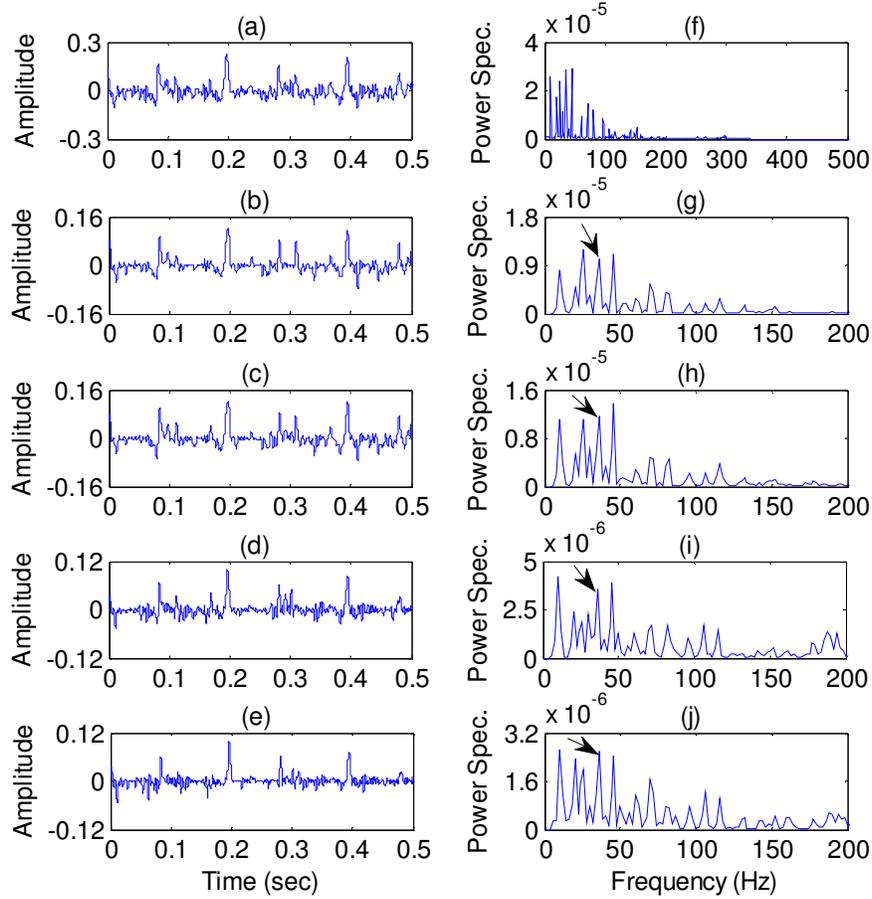
Figure 5.13. RSD using overall residual signal from simulated signal: (a) residual signal after filtering gear mesh signal; (b) HR signal ($Q_1 = 3$, $r_1 = 10$); (c) HR signal ($Q_1 = 4.5$, $r_1 = 25$); (d) LR signal ($Q_2 = 2$, $r_2 = 10$); (e) LR signal ($Q_2 = 3.5$, $r_2 = 25$); figures (f) to (j) correspond to their respective power spectra. Arrows indicate bearing characteristic frequency.

To further improve signal-to-noise ratio of the bearing signal, the shaft running signatures are filtered out from the vibration signal. If the shaft frequency is f_r Hz in the frequency domain, the stopbands will be [pf_r – BW, pf_r + BW] around at the center frequency [pf_r+1], $p = 1, 2, \dots ,$ 5; BW is a band window and is selected as BW = 20% f_r or BW = 2, in this case. The new signal residual is shown in Figure 5.14(a). With similar Q and r values as used previously, the time-domain signals and the corresponding power spectra of the HR responses are illustrated in Figures 5.14(b), 5.14(c), 5.14(f) and 5.14(g), respectively. Figures 5.14(d), 5.14(e), 5.14(h) and 5.14(i) illustrate corresponding results with LR resonance signals; it is seen that the bearing characteristic frequency can be recognized clearly, which also dominates the spectrum of Figure 5.14(i).
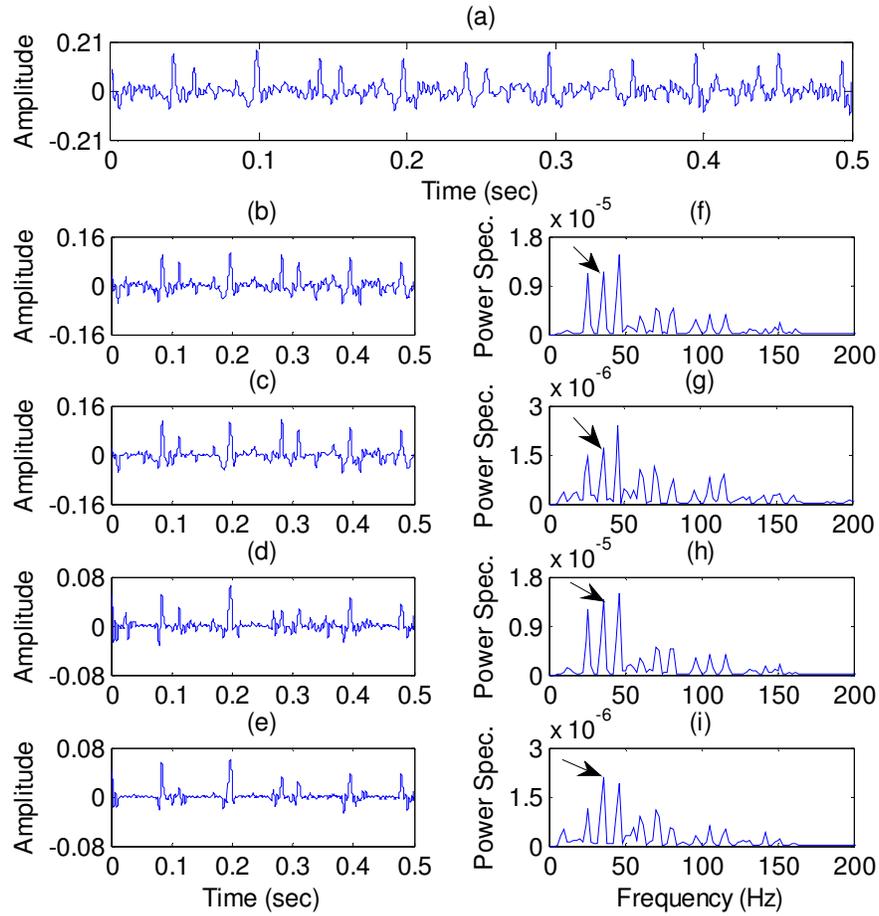
Figure 5.14. LRSD for fault detection: (a) Signal residual after shaft and gear signals are removed; (b) HR signal ($Q_1 = 3$, $r_1 = 10$); (c) HR signal ($Q_1 = 4.5$, $r_1 = 25$); (d) LR signal ($Q_2 = 2$, $r_2 = 10$); (e) LR signal ($Q_2 = 3.5$, $r_2 = 25$); Figures (f) to (g) correspond to their respective power spectra. Arrows indicate bearing characteristic frequency.

To compare the processing speed of the general RSD and the proposed LRSD, testing was undertaken using a laptop computer with processor Intel® Core™ i3-2310M CPU (2.10GHz). Table 5.1 summarizes the processing time to reach 5% error using 100 iterations to compute the values of J_{max}. It is seen that the LRSD is faster (approximately 15~40%) than the general RSD. Compared to available RSD fault detection methods, the proposed LRSD technique can achieve a sparse representation of the signal without the use of complete reconstruction operations and complex post-processing. The performance comparison will be undertaken in the following subsection by experimental tests.

Table 5.1. Processing speed comparison in terms of processing time in seconds using different J_{max} values

Method	J_{max} Values				
	50	100	150	200	250
RSD	68.5 sec	198.6 sec	378.3 sec	439.4 sec	786.7 sec
LRSD	65.8 sec	160.9 sec	272.7 sec	278.3 sec	464.1 sec

5.3.2 Experimental testing setup

To verify the effectiveness of the proposed LRSD technique for bearing fault detection in gearboxes, a series of tests were undertaken under different system conditions. The tests were performed using an experimental setup (from Spectra Quest Inc.) similar to the one used in Section 3.3 (Figure 3.2) with controlled test conditions. As shown in Figure 5.15, in this test, bearings are installed inside a gearbox under various operating conditions. Three sets of ball bearings (MB ER-12K) are secured to the shafts, which have the following parameters: number of rolling elements: 8; rolling element diameter: 7.938 mm; pitch diameter: 33.477 mm; and contact angle: 0 degrees. The bearing on the right side of the input shaft is for testing. The gearbox consists of two pairs of spur gears, as shown in Figure 5.16(a). The input pair of pinion/gear has 32 and 80 teeth, and the second pair has 96 and 48 teeth, respectively. Dynamic load is applied by a magnetic particle brake system (Placid Industries, B150-24-H). Vibrations signals are collected using ICP accelerometers (ICP-IMI, SN98697) with a sensitivity of l00mV/g, and are mounted on the gearbox casing along different directions, as shown in Figure 5.16(b). These vibration and reference signals are fed into a computer for further processing through the data acquisition system.
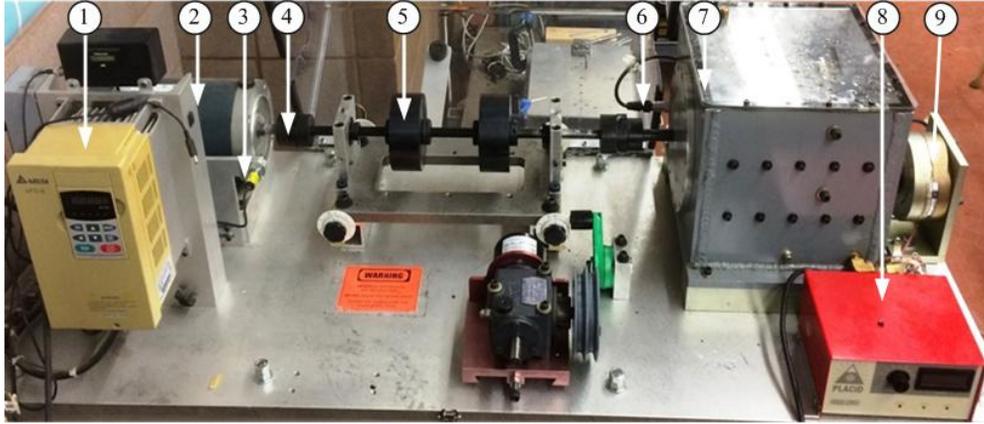
Figure 5.15. Experimental setup: (1) speed controller; (2) motor; (3) optical sensor; (4) flexible coupling; (5) load disc; (6) accelerometer; (7) gearbox; (8) magnetic power supply; (9) magnetic brake load system.

(a)   (b)
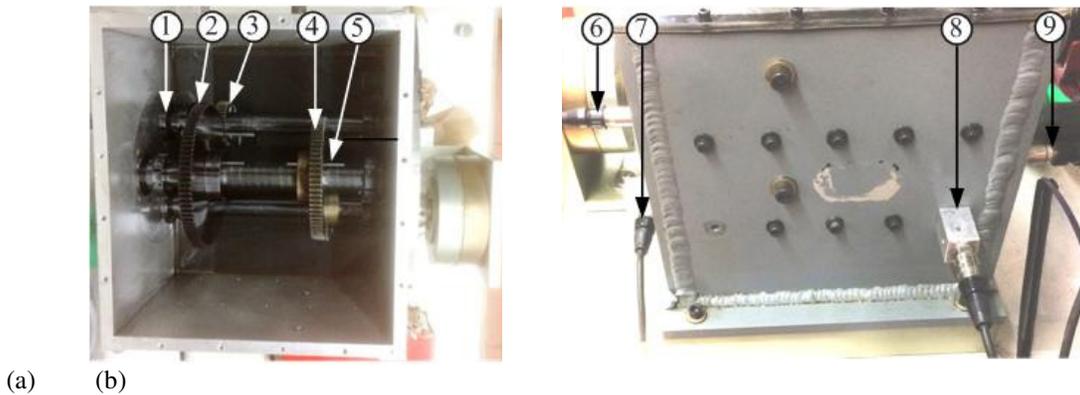
Figure 5.16. (a) The two-stage gear system: (1) the tested bearing at input shaft; (2) input gear; (3) input pinion (4) output gear; (5) output pinion at output shaft. (b) Installation of ICP accelerometers for vibration measurement: (6) along radial output; (7) along horizontal output; (8) along horizontal input; (9) along radial input.

5.3.3 Performance evaluation of the proposed LRSD technique

The effectiveness of the proposed LRSD technique is tested for bearing fault detection in gearboxes. For comparison, the processing results from the classical RSD method without the use of the leakage-free filter are provided. To examine the effectiveness of the proposed leakage-free filter, the RSD using classical bandstop filters, RSDc in short, is studied.

In this test, the sampling frequency of the experiments is selected in terms of the shaft speed to ensure the collection of 600–700 samples over each shaft rotation cycle. In this test, five bearing health conditions are considered: healthy bearings, bearings with outer race defect (minor and severe), and bearings with inner race defect (minor and severe). Five different shaft

87

speeds (i.e., 240, 540, 840, 1140, and 1320 RPM) and eight loading levels (i.e., 0, 03, 1.2, 2.8, 6.5, 9.4, 14, and 17 N.m) are used to test each bearing condition. The outer race defects have a size (area × depth) of 0.2 mm^2 × 0.5 mm for a minor defect, and 0.4 mm^2 × 0.5 mm in the case of a severe fault, respectively. The inner race defect sizes measure about (area × depth) 0.2 mm^2 × 0.5 mm for minor defect, and 0.4 mm^2 × 0.5 mm for severe fault cases.

In order to select the proper Q and r values, we proposed a selection method based on a ψ measure, which is defined as:

$$\psi(i) = \overline{K}_r(i) \times \cos_i(\Phi) \tag{5.40}$$

where $\overline{K}_r(i) = K_r(i) / \sum K_r(i)$ is the normalized kurtosis and $\cos(\Phi)$ is the cosine distance similarity measure.

The kurtosis is computed by:

$$K_r(i) = \frac{\mu_4(i)}{\sigma^2(i)}, \quad i = 1, 2, \ldots, I \tag{5.41}$$

where $\mu_4(i)$ is the fourth moment and $\sigma(i)$ is the standard deviation at the ith processing level for a given Q and r, where $Q \in [1, 50]$ and $r \in [1, 20]$, $I = 20$ steps in this case.

The cosine distance is a similarity measure over [0,1] between two non-zero vectors, to measure the cosine of the angle, expressed as:

$$\cos_i(\Phi) = \frac{\left(x(t) \cdot \widehat{x}_i(t)\right)}{\left(\|x(t)\|_2 \|\widehat{x}_i(t)\|_2\right)} \tag{5.42}$$

where $\|*\|_2$ is the L_2 norm of the input signal $x(t)$, and $\widehat{x}(t)_i$ is the processed signal at the ith level [162-164].

The higher the value of the proposed measure ψ in Equation (5.40), the more representative the reconstructed function at particular i level, since defect features are impulsive and usually have some modulation from normal distribution. Figure 5.17 demonstrates the normalized values of the proposed ψ measure corresponding to $Q \in [1, 20]$ and $r \in [5, 50]$ at $J = 50$ levels. The highest

ψ measure value occurs at $Q = 32$, 20 and $r = 8$, 2.5, respectively. The higher Q and r values are used for HR analysis, whereas the lower Q and r values are used for LR analysis.
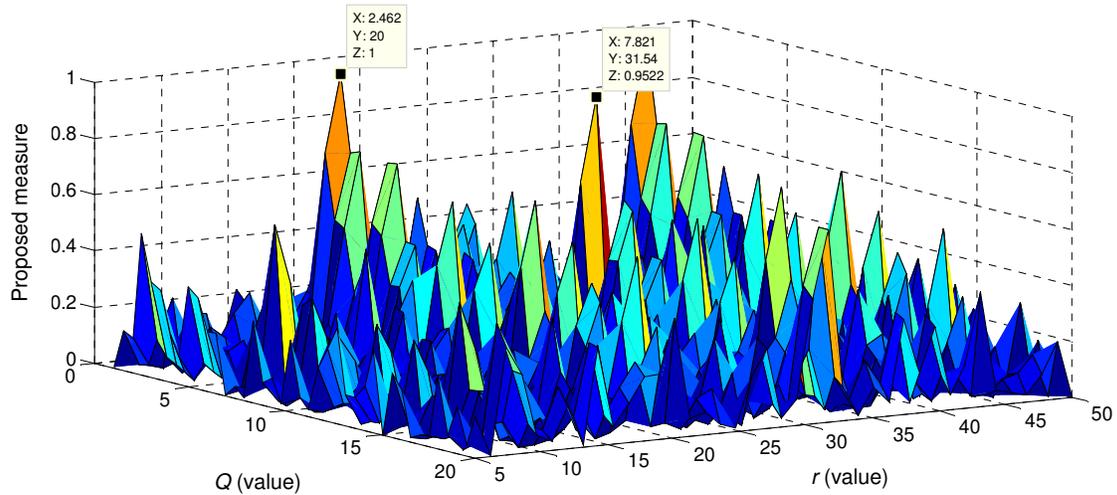
Figure 5.17. Proposed ψ measure for different Q and r values.

To facilitate comparison, RSD, RSDc, and LRSD will use the same parameters such that $J_1 = 50$, $Q_1 = 8$, $r_1 = 32$ and $J_2 = 50$, $Q_2 = 2.5$, $r_2 = 20$, for HR and LR, respectively. All of the related techniques are programmed using MATLAB.

1) Condition monitoring of a healthy bearing

The bearings with healthy conditions are tested first. Figures 5.18 and 5.19 show the processing results using the related techniques. In this case, the bearing characteristic frequency is $f_r = 22$ Hz, the input gear set MF$_i$, MF$_i \approx 704$ Hz, and the output gear set MF$_o$, MF$_o \approx 587$ Hz Figures 5.18(a) and 5.18 (b) display a part of the vibration signal and its power spectrum; the health condition of the gearbox bearing cannot be clearly diagnosed. Figures 5.18(c) and 5.18(d) show the HR in the time and frequency domains, whereas Figures 5.18(e) and 5.18(f) show the LR responses in time and power spectrum, respectively. Examining these power spectral graphs in Figures 5.18(d) and 5.18(f), healthy condition of the bearing can be identified, even though the characteristic frequency does not dominate the spectrum. Thus, further processing is needed to filter the gear MF from the collected signal.
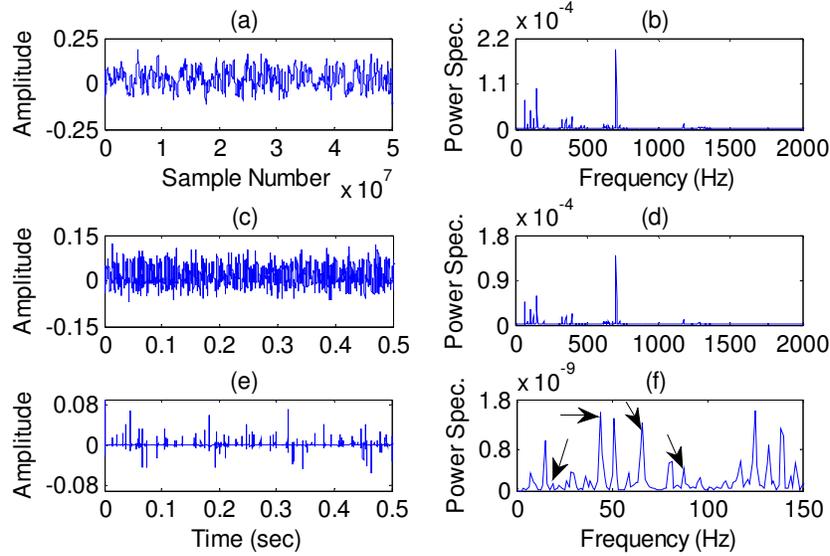
Figure 5.18. Processing results using the RSD for a healthy bearing: (a) part of original signal; (b) power spectrum of (a); (c) HR time signal; (d) power spectrum of (c); (e) LR time signal; (f) power spectrum of (e). Arrows indicate bearing characteristic frequency and its harmonics.

The LRSD is applied to remove MF_i and MF_o and their harmonics; the residual signal and frequency spectra are shown in Figures 5.19(a) and 5.19(b), respectively. Examining the HR response in Figures 5.19(c) and 5.19(d), the second, third, and fourth harmonics of shaft speed can be clearly recognized. From the LR responses in Figures 5.19(e) and 5.19(f), we can also see that the dominant bearing characteristic frequency and its harmonics on the spectrum, which confirms the healthy condition of the bearing in the gearbox. Such clear diagnostic results are due to effective feature extraction of the proposed LRSD method.
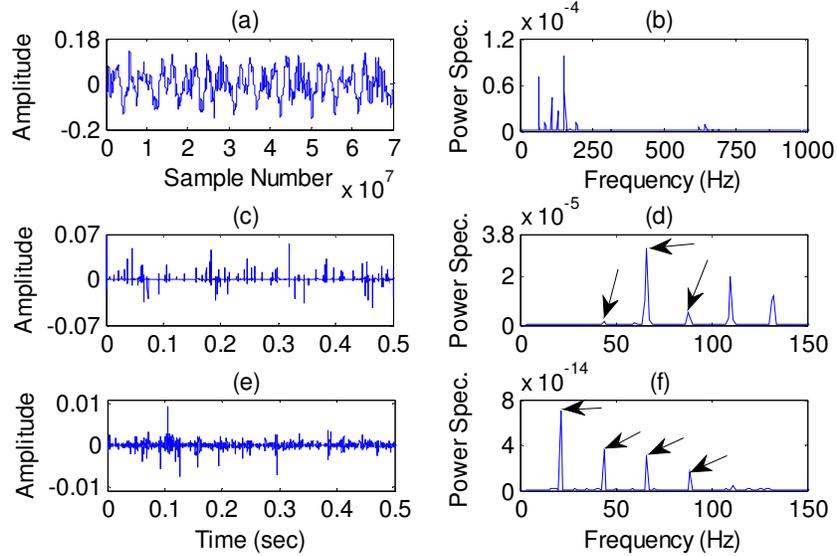
Figure 5.19. Processing results using the LRSD for a healthy bearing: (a) signal residual; (b) power spectrum of (a); (c) HR of the signal residual; (d) power spectrum of (c); (e) LR of the signal residual; (f) power spectrum of (e). Arrows indicate bearing characteristic frequency and its harmonics.

2) Outer race fault detection

As stated before, feature modes of outer race defects do not change over time. In this case, the characteristic frequency is $f_{OR} \approx 67.2$ Hz. Figures 4.20, 4.21, and 4.22 show processing results using the related techniques. It is seen that the gear MF (MF_i and MF_o) and shaft-related harmonic dominate the spectrum in Figure 4.20(b). By applying RSD, gear MFs and shaft signals dominate the HR (Figures 4.20(c) and 4.20(d)) and LR responses (Figures 4.20(e) and 4.20(f)), respectively.

91
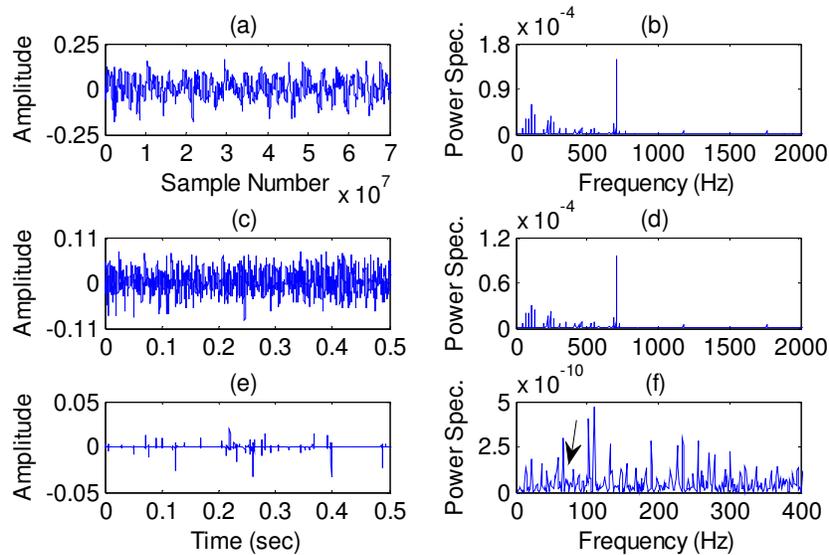
Figure 5.20. Processing results using RSD for a bearing with outer race defect: (a) collected signal; (b) power spectrum of (a); (c) HR signal; (d) power spectrum of (c); (e) LR signal; (f) power spectrum of (e). Arrow indicates bearing characteristic frequency.

The gear mesh and shaft running signals are removed by the use of the general bandstop filters; the processing results using the RSDc are illustrated in Figure 5.21. The signal residual and its spectrum are shown in Figures 5.21(a) and 5.21(b). The HR and LR responses are illustrated in Figures 5.21, 5.21(c) and 5.21(d), as well as Figures 5.21(e) and 5.21(f), respectively. The power spectrum results in Figures 5.21(d) and 5.21(f) cannot provide reliable diagnostic information about the faulted bearing.
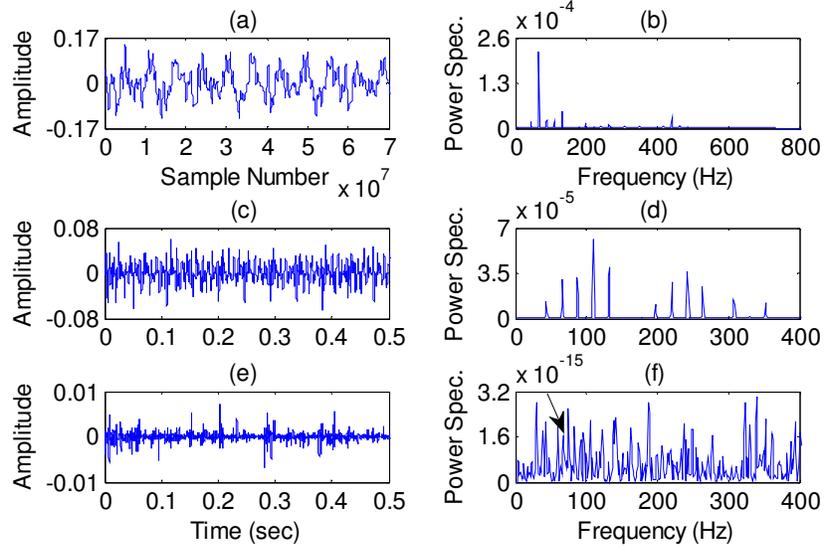
Figure 5.21. Processing results using RSDc for a bearing with outer race defect: (a) signal residual; (b) power spectrum of (a); (c) HR signal; (d) power spectrum of (c); (e) LR signal ; (f) power spectrum of (e). Arrows indicate bearing characteristic frequency and its harmonics.

On the other hand, utilizing the proposed LRSD technique, the signal residual is shown in Figure 5.22(a); and its HR and LR responses are illustrated in Figures 5.22(c) and 18(e), whereas the spectra of these signals are shown in Figures 5.22(b), 5.22(d) and 5.22(f), respectively. It is seen from the power spectrum of Figure 5.22(f) that the proposed LRSD outperforms the RSD (Figure 5.20(f)) and RSDc Figure 5.21(f)); Figure 5.22(f) has not only clear characteristic frequency components, but also these components dominating the spectral map. The results can be used effectively for health condition monitoring of bearings in gearboxes.
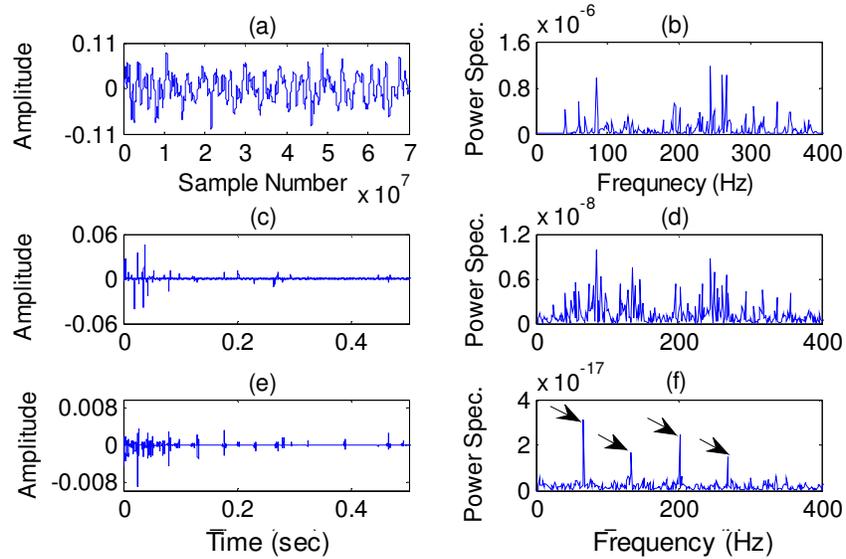
Figure 5.22. Processing results using LRSD for a bearing with outer race defect: (a) signal residual; (b) power spectrum of (a); (c) HR signal; (d) power spectrum of (c); (e) LR signal; (f) power spectrum of (e). Arrows indicate bearing characteristic frequency and its harmonics.

3) Inner race fault detection.

As stated previously, the detection of faults on the inner race (rotating bearing race) is usually more challenging than the detection of a fault on the outer race (fixed bearing race) because the resonance modes associated with the inner race impulses vary over time. In this case, the characteristic frequency $f_{IR} \approx 109$ Hz. Figures 5.23, 5.24, and 5.25 outline the processing results using the related techniques. Similarly, based on the collected vibration signal from the gearbox casing (Figures 5.23(a)), gear MFs and shaft signal dominate the HR responses (Figures 5.23(c) and 5.23(d)), and LR responses (Figures 5.23(e) and 5.23(f)), respectively, using the RSD. The bearing characteristic features cannot be recognized clearly for reliable bearing fault detection.
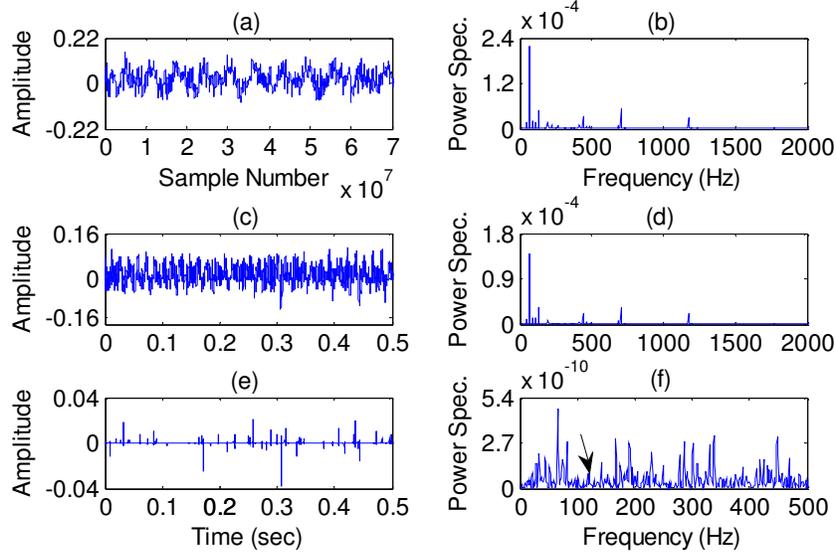
Figure 5.23. Processing results using RSD for a bearing with an inner race defect: (a) collected signal; (b) power spectrum of (a); (c) HR signal; (d) power spectrum of (c); (e) LR signal; (f) power spectrum of (e). Arrows indicate bearing characteristic frequency and its harmonics.

After removing the gear MFs using RSDc, the HR response in Figure 5.24(d) and LR response in Figure 5.24(f) still cannot provide a clear indicator about health conditions of the tested bearing. Nonetheless, applying the proposed LRSD by filtering out both gear MFs and shaft rotating signatures, it is clear that the proposed LRSD in Figures 5.25(e) and 5.25 (f) outperforms those using RSD (Figures 5.23(f)) and RSDc (Figure 5.24(f)). The LRSD maps have higher resolution of bearing characteristic frequency components and its harmonics dominate the spectral maps, thanks to the efficient leakage-free filtering and resonance response information processing.
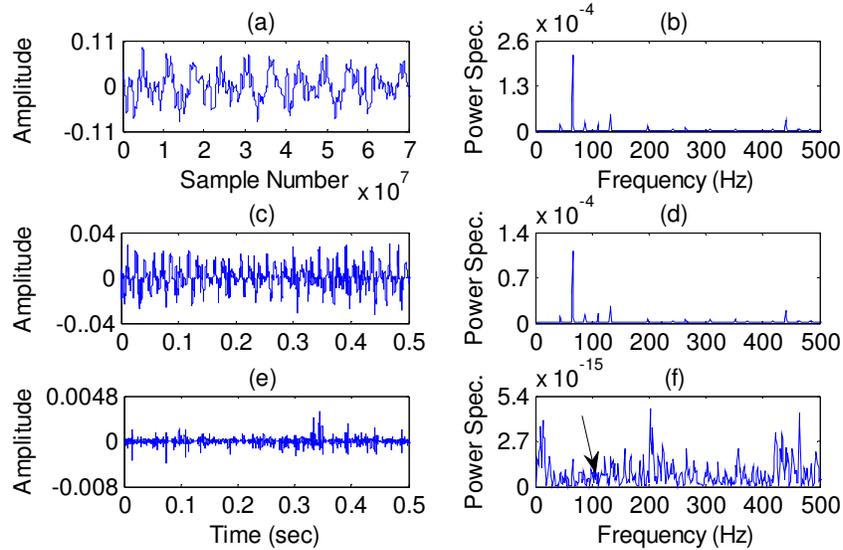
Figure 5.24. Processing results using RSDc for a bearing with an inner race defect: (a) collected signal; (b) power spectrum of (a); (c) HR signal; (d) power spectrum of (c); (e) LR signal; (f) power spectrum of (e). Arrows indicate bearing characteristic frequency and its harmonics.
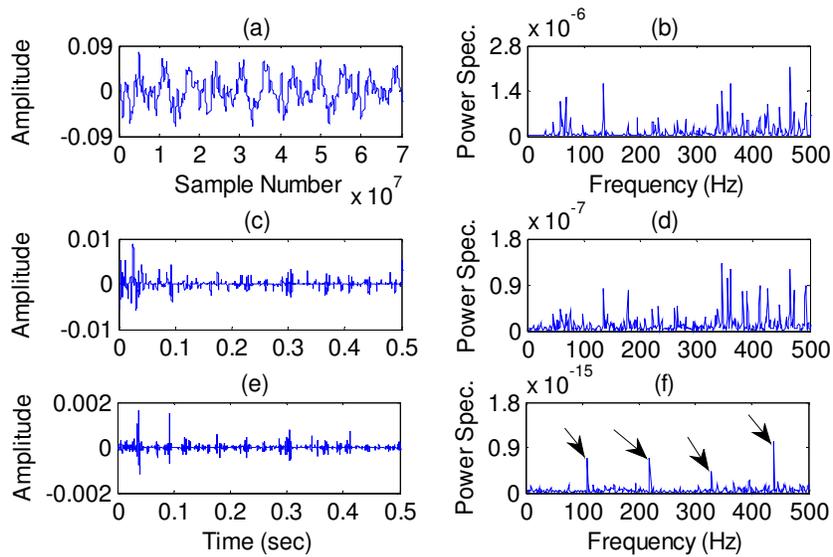

Figure 5.25. Processing results using LRSD for a bearing with an inner race defect: (a) collected signal; (b) power spectrum of (a); (c) HR signal; (d) power spectrum of (c); (e) LR signal; (f) power spectrum of (e). Arrows indicate bearing characteristic frequency and its harmonics.

Chapter 6

Conclusion and Future Work

6.1 Conclusions

Gearboxes are vital systems in rotating machinery. A reliable monitoring system is critically needed in industries to provide early warning of damage or malfunction in order to avoid sudden failures and breakdowns. Fault detection in rolling element bearings in gearboxes remains the most challenging topic not only in gear system monitoring, but also in this R&D field. A bearing is not a component like a shaft or a gear, but a system consisting of inner/outer rings, rolling elements and a cage. In addition, bearing vibration signals are relatively weak in magnitude, which are usually modulated by strong gear mesh signals from gearboxes. The objective of this PhD research is to develop new technologies for bearing fault detection in gearboxes. The strategy is on how to differentiate between gear and bearing signals. The decoupling strategies are based on the assumption that gear signals are periodic deterministic contents, whereas the bearing signals experience some randomness and can be approximated as a second order cyclostationary.

Firstly, a novel morphological Hilbert-Huang transform technique, MH in short, has been proposed for incipient bearing fault detection and non-stationary signal analysis. The collected vibration signals are firstly denoised by the proposed enhanced morphological (eM) filtering technique that does not require prior knowledge about the signal. Next, a normality indicator is employed to select the most distinctive IMF for MH processing. This new morphological filter is based on Renyi entropy analysis to actively enhance the impulsive features. The effectiveness of the proposed MH technique has been verified by experimental tests corresponding to different bearing conditions. The MH method can effectively recognize distinctive IMFs for non-stationary signal analysis and bearing fault detection. Test results have also shown that the proposed filter can effectively denoise the signal and highlight defect-related features.

Secondly, an integrated Hilbert-Huang transform (iHT) technique has been suggested for non-stationary signal analysis and incipient bearing fault detection. A new weighted normality

indicator (named JM) is suggested for selecting unique IMF. Next, the selected most prominent IMFs are used to integrate the selected IMFs for bearing defect detection. The efficiency of the proposed iHT technique has been confirmed through experimental testing corresponding to different bearing conditions. The iHT method can effectively recognize more distinctive IMFs for non-stationary signal analysis and bearing fault detection. It has a potential for real-world bearing condition monitoring applications.

A new leakage-free resonance-based signal sparse decomposition, namely LRSD, has been proposed for high and low resonance response analysis, and incipient bearing fault detection in gearboxes. The suggested scheme includes a novel leakage-free filter procedure and the resonance-based signal sparse decomposition (RSD). The leakage-free filter is recommended based on prior knowledge about the gearbox components, and to reduce the periodic interference effects due to gear mesh (MF) and shaft modulated signals. In the proposed LRSD, the leakage-free filter is used first to demodulate bearing signals by removing MF and shaft signals. The r and Q values in the TQWT are properly selected based on a kurtosis- cosine distance measure. The effectiveness of the proposed LRSD technique is verified experimentally. Test results prove that the proposed LRSD technique can effectively diminish interfering gears and shaft signals to highlight defect-related features. It has a potential for real world bearing fault detection in gearboxes.

6.2 Future Work

Future research is suggested to address the following topics:

1) Similar to other propositions in this R&D field, the main limitation of proposed techniques is that this work is undertaken with controlled parameter selection in order to reduce computational burden. Advanced research can be undertaken to develop a faster and more efficient technique to demodulate bearing signals collected from gearboxes and develop techniques for combined fault detection (gear and bearing faults) to expedite efficient and robust applications.

2) Vibration signals are utilized in the current work. It would be advantageous to test the developed system with signals coming from different sensors, such as the current sensors and acoustic sensors.

3) Although the presented methods have accurately recognized bearing conditions, the results obtained using experimental data. In actuality bearings mounted on real-world applications such as water treatment plant pumps, trains, etc. could be used to validate the robustness of the proposed techniques. Vibration signals obtained from these environments are expected to have different characteristics than those obtained from a test rig in the lab.

4) Further studies of the proposed techniques in the design and test of integrated a smart-sensor using vibration and current signals are recommended. As a matter of fact, in the course of this work, some developments in graphical user interface (GUI) are discovered (see Appendix B) that would be appropriate for other applications rather than the test rig in the lab and for stand-alone, continuous, real-time performance and condition monitoring of rotary machinery.

Appendix A

Resonance Based Decomposition (RSD) Validation Test

In this section, Tunable Q Wavelet transform technique TQWT and split augmented Lagrangian shrinkage algorithm (SALSA) techniques are validated using high and low frequency signals. Each individual signal contains three different frequencies. All signals used for this validation test are sinusoidal in nature in order to keep computational complexity to minimum.

A.1 Tunable Q Wavelet transform technique (TQWT)

As previously discussed in Chapter 5, the most important parameters for the TQWT are the Q factor, redundancy (r), and the number of levels (J).

Figure A.1 shows the signal response in time for three low frequency signals combined (Figure A.1(a)) and three high frequency signals combined (Figure A.1(b)). From these figures, it can be seen that there are three distinct frequencies in each of the low and high frequency signals.
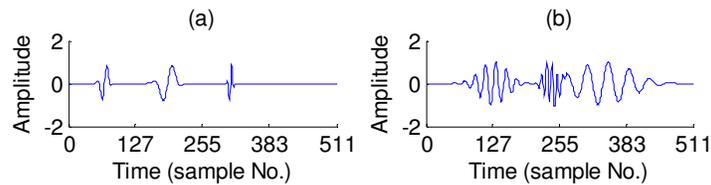
Figure A.1. Simulated signal with three different frequencies: (a) low resonance; (b) high resonance.

First, each signal is processed individually, using separate TQWT parameters: ($Q = 1$, r =3, and J =7) for a low frequency signal, and ($Q = 3.5$, r =3, and J =12) for a high frequency signal. In addition, the sampling frequency, f_s, is set to one sample per second for 512 samples. Figure A.2 illustrates the subband response in time for each TQWT response for the low (Figure A.2(a)) and the high (Figure A.2(b)) frequency signals. The Wavelet response and its corresponding scaling function at each prospective level are shown in Figure A.3 at level 7 for the low frequency signal (Figures A.3(a) and A.3(c)), and at level 12 for the high frequency signal (Figure A.3(b) and A.(d)), respectively.
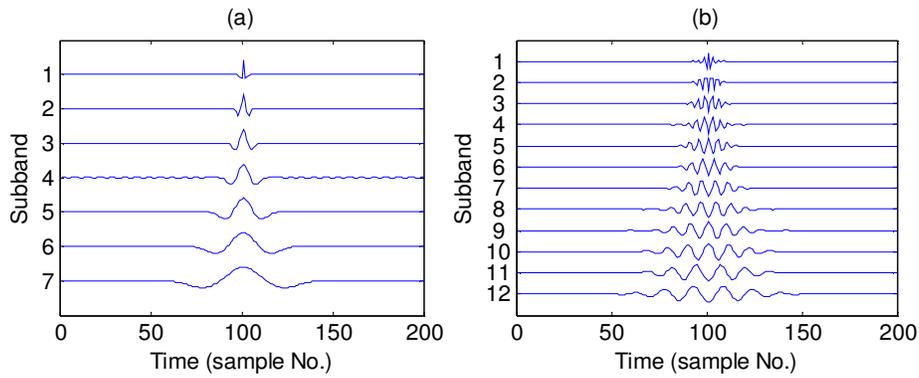
Figure A.2. Wavelets subbands of simulated signal: (a) low resonance (1-7); (b) high resonance (1-12).
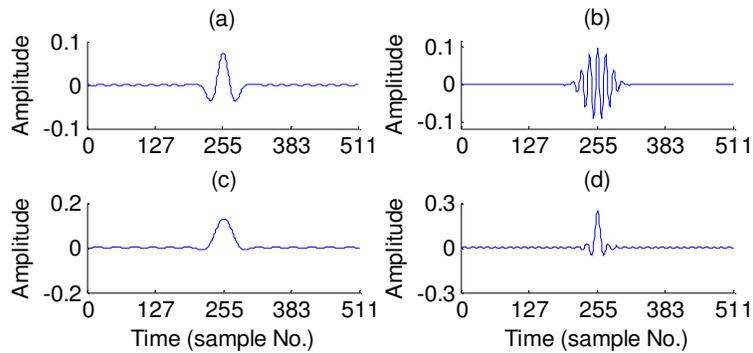
Figure A.3. Simulated signal Wavelet response: (a) at level 7; (b) at level 12; (c) lowpass scaling function at level 7; (d) lowpass scaling function at level 12.

The TQWT must satisfy Parseval's energy theorem, which states that the total combined energy of the Wavelet coefficients must equal the energy of the signal. The energy of each Wavelet coefficient subband for the low frequency signal is shown in Figure A.4(a), however it can been observed that the total energy is only 93% of the signal energy, which means that the remaining energy is contained in the (J+1) level (Figure A.5(a)). Although the added energy of each Wavelet coefficient subband for the high frequency signal (Figure A.4(b)) is only 16% of the signal energy, the remaining energy is contained in the (J+1) level (i.e., level 13), as demonstrated in Figure A.5(b)).
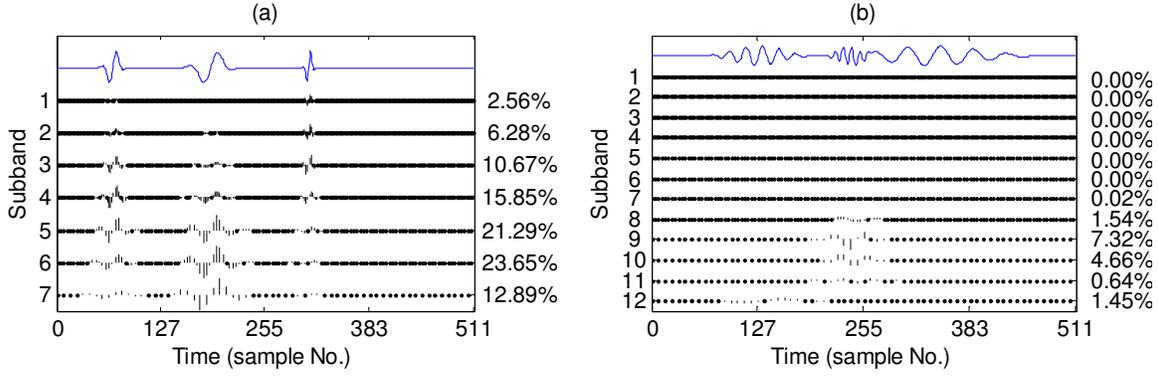
Figure A.4. Energy percentage of the total energy at each Wavelet subband for: (a) low resonance; (b) high resonance.
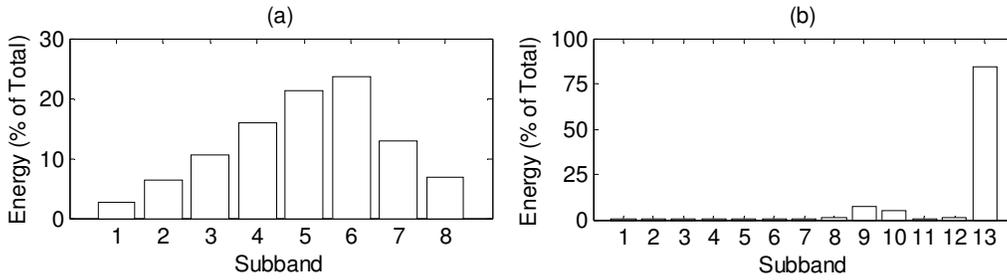
Figure A.5. Distribution of signal energy at each subband for: (a) low resonance; (b) high resonance.

A.2 Split Augmented Lagrangian Shrinkage Algorithm (SALSA)

Firstly, the setup of the spare representation of the signal is accomplished using equations from Chapter 5 (Equations 5.23 to 5.35). Then, the regularization parameters ($A_1 = 0.45$ and $A_2 = 0.5$) for high frequency and the low frequency responses, respectively) are set as a vector of length $J+1$, and the μ is set as 0.1. This μ affects the convergence speed; however, optimization of the SALSA function using these parameters is usually achieved through empirical methods or some rough proportionality estimation of signal energy. Figure A.6 shows the cost function of 100 iteration for the low frequency signal (Figure A.6(a)) with a relative root mean square (RMS) reconstruction error of 6.4 $\times 10^{-2}$ (Figure A.7(a)), and a high frequency signal (Figure A.6(b)), with a relative RMS reconstruction error of 6.8 $\times 10^{-2}$ (Figure A.7(b)). The energy of the reconstructed subband is shown in Figure A.7. For the low frequency response, it can be seen that the total energy (for levels 1-7) has increased from 93% to 99% (Figure A.8(a)), whereas for the high frequency response, the total energy (for levels 1-12) has increased from 16% to 20%

(Figure A.7(b)). Therefore, this proves the effectiveness and efficiency of combining TQWT and SALSA in the RSD method.
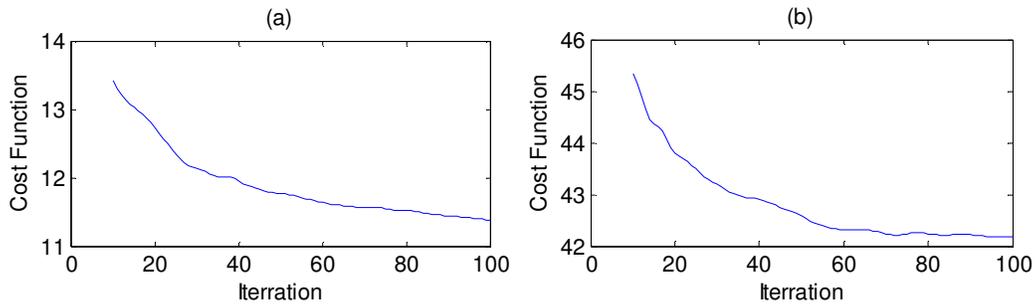
Figure A.6. SALSA cost function for 100 iterations for: a) low resonance; (b) high resonance.
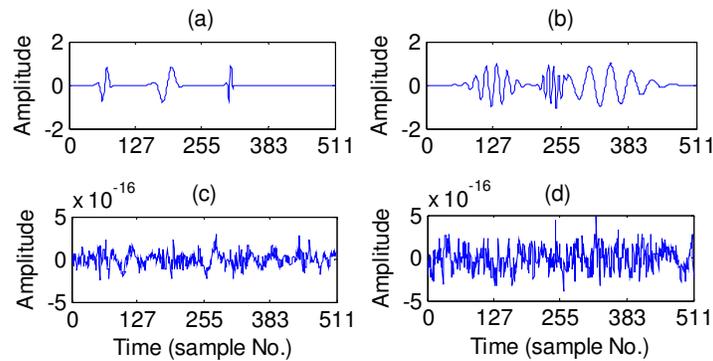
Figure A.7. Simulated signal reconstruction of: (a) low frequency; (b) high frequency; (c) error of (a); (d) (c) error of (b).
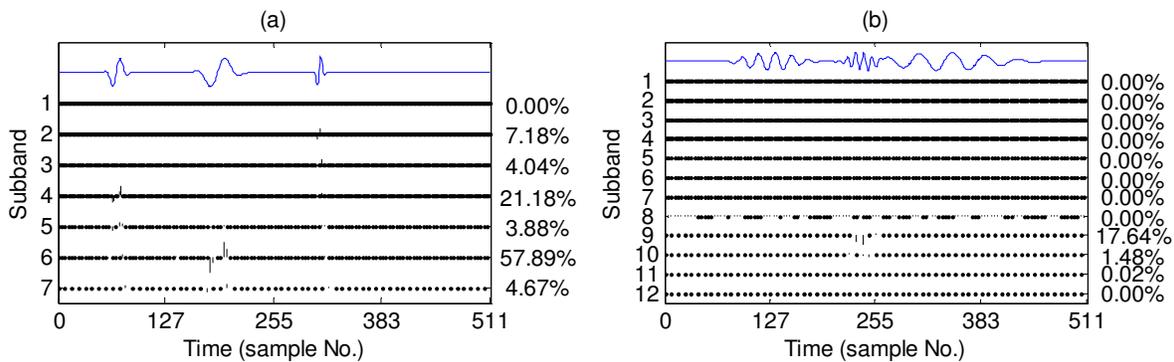
Figure A.8. Energy percentage after of the total energy applying SALSA at each Wavelet subband for: (a) low resonance; (b) high resonance.

In this next section, the two low and high frequency signals (shown in Figure A.1) are combined including all six different frequencies, as shown in Figure A.9(a). Using the same values as the previous test for the TQWT and SALSA parameters, the high resonance component at level 12 is shown in Figure A.10(a), and the low resonance component at level 7 is shown in

Figure A.10(b). The reconstruction of the high frequency signal is shown in Figure A.9(b), whereas the reconstruction of the low frequency signal is shown in Figure A.9(c). The residual signal is outlined in Figure A.9(d), which has a reconstruction relative RMS reconstruction error of 1.865×10^{-16}. The cost function for 100 iteration of SALSA is shown in Figure A.11.
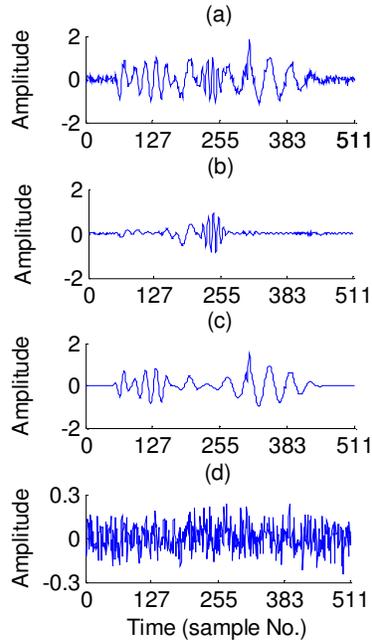
Figure A.9. Combined high and low frequencies simulated noisy signal: (a) combined signals; (b) high resonance response; (c) low resonance response; (d) residual.
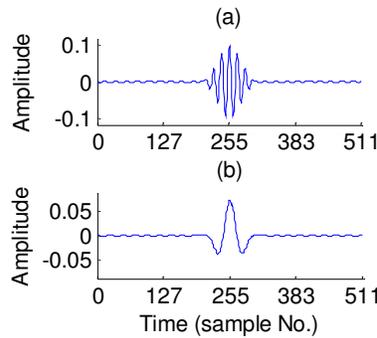
Figure A.10. Combined signal Q Wavelet response: (a) high resonance component at level 12; (b) low resonance component at level 7.
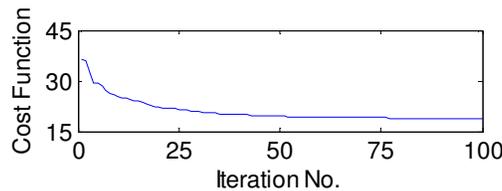
Figure A.11. Cost function for 100 iteration of SALSA.

The responses of the RSD are compared for different parameters of the TQWT and RSD in terms of the averaged relative RMS values for signal reconstruction of simulated signal shown in Figure A.9(a). TQWT parameters are initialized as follows ($Q_1 = 3.5$, $r_1 = 3$, and $J_1 = 12$) for a high frequency signal, and ($Q_2 = 1$, $r_2 = 3$, and $J_2 = 7$) for a low frequency signal. In addition, for RSD parameters of the SALSA are initialized as ($A_1 = 0.35$ and $A_2 = 0.40$) and the output is also compared. Multiple tests were conducted for each parameter of the TQWT and SALSA and the averaged relative RMS values for signal reconstruction of simulated signal is evaluated as shown in Table A.1. The TQWT and RSD are sets as ranges, for high frequency response of the simulated signal ($Q_1 = [1.5, 2.5, 3.5, 4.5, 5.5]$, $r_1 = [3, 4, 5, 6, 7]$, $J_1 = [8,10,12,14, 16]$, and $A_1 = [0.15, 0.25, 0.35, 0.45, 0.55]$), and for low frequency response of the simulated signal ($Q_2 = [1, 2, 3, 4, 5]$, $r_2 = [3, 3.5, 4, 4.5, 5]$, $J_2 = [3, 5, 7, 9, 11]$, and $A_2 = [0.1, 0.3, 0.5, 0.7, 0.9]$), respectively. The tests were repeated for iteration numbers [Iter = [20, 60, 100, 140, 180] and for $\mu = [.05, 0.1, 0.15, 0.2, 0.25]$. When the parameter or the variable (Var) is not being tested, it was set back to its initial value. The empirical test that was utilized in obtaining results in Table A.1 shows that carful considerations should be made when deciding the range of parameter's values to be employed, next the selection decision of which sets of parameters should be made to process the signal while minimizing computational burden and the relative RMS values.

Table A.1. MCA parameters compared in terms of averaged relative RMS reconstruction errors.

Var./ Iter.	20	60	100	140	180
Q_1	1.84E-01	1.81E-01	1.87E-01	1.82E-01	1.84E-01
r_1	1.86E-01	1.86E-01	1.82E-01	1.85E-01	1.85E-01
J_1	1.90E-01	1.82E-01	1.91E-01	1.85E-01	1.82E-01
A_1	1.04E-01	1.58E-01	1.84E-01	1.96E-01	2.04E-01
Q_2	1.89E-01	1.97E-01	1.90E-01	1.91E-01	1.95E-01
r_2	1.85E-01	1.82E-01	1.91E-01	1.86E-01	1.88E-01
J_2	1.92E-01	1.91E-01	1.84E-01	1.84E-01	1.88E-01
A_2	7.51E-02	1.68E-01	1.90E-01	2.01E-01	1.96E-01
μ	1.73E-01	1.84E-01	1.87E-01	1.77E-01	1.78E-01
Iteration No.	1.46E-01	1.82E-01	1.83E-01	1.87E-01	1.84E-01

Appendix B

Integrated Smart Sensor User Interface Design

B.1. Introduction

Modern rotary machinery consists of many mechanical systems such as bearings, shafts, and gears, which are all susceptible to breakdown. Without any condition monitoring system, the breakdown is usually catastrophic, and requires an expensive part replacement. Real-time condition monitoring allows for early detection of faults, which could require a simple solution such as the application of a lubricant. This type of preventive measure not only prolongs the useful life of the component, but it also prevents sudden and unexpected equipment failure. Real-time condition monitoring can be accomplished by examining different signatures/information carriers of mechanical system [166]. For example, a vertical pump system consists of a motor and its associated bearings and couplings, a gear reduction system consisting of worm and spur gears, and kinematic links. Faults resulting in excessive vibration may be caused by coupling misalignment, bearing failure, or gear train failure [167]. Each fault occurs at its characteristic frequency, and therefore the state of the mechanical system can be determined by monitoring the amplitudes of the relevant frequencies. Vibration due to coupling misalignment occurs at the harmonics of the shaft rotational speed. Gear vibration occurs at the gear turn speed or at the sidebands of the gear mesh frequency [168-170]. Ball bearing vibration may be caused by outer bearing race defects, inner bearing race defects, or rolling element defects, all which can be estimated at specific frequencies.

By monitoring the real-time signatures of the mechanical system (vibration in this work), anomalies can be quickly identified and addressed. This Appendix provides a description of a graphical tool that can be used to allow the user (using a computer) to control and communicate with the sensor, process collected data, and displays results. Health monitoring is the method of evaluating reliability in terms of a product's health in its life cycle environment. Most of the work done on health monitoring available in literature focuses on diagnostic or condition monitoring of various mechanical structures [171-173]. Typical methods used for condition monitoring can include [4-8,166-170]: visual inspection, vibration signatures and modal analysis, current analysis, and temperature analysis, etc.

In order to implement an online condition monitoring system or concept in an industrial environment as economically as possible, utilizing the communication capabilities of the industrial environment is required. Depending on the solution selected, the analyses of the conditions are performed in a measuring device, in power controlling devices such as switches, frequency converters etc., or in computers at a local or global management level in industrial plants [168]. If all analyses are performed in a measuring device, large processing capacity of the device is required. If the measurement device only collects data, calculation capacity requirements are more modest, but the capacity of communication is extended. This is due to the necessity of transferring measurement data (perhaps pre-processed) to an analyzing device. It is possible that vibration monitoring is required in order to achieve adequate reliability of the condition estimate of the rotary machinery. In this case, the data must be exported from the machine installation location [171-173]. One objective of this part of work is to explore these possibilities when condition monitoring is implemented with a stand-alone condition-monitoring device, or as a part of some other device such as a motor protection relay or smart graphical monitoring system. The implementation of the condition-monitoring system should adapt to the industrial information infrastructure, providing means for global monitoring.

B.2. MEMS-based Smart Sensor Development

A measurement system consists of three basic parts, as illustrated in Figure B.1 The sensor, in this case a Microelectromechanical system (MEMS) accelerometer, is a device that converts a physical input into an output, usually voltage or pulse width modulation. The signal processor performs signal conditioning and analysis on the sensor output. Finally, a computer is used to display sensor data for real-time monitoring and subsequent processing.

Sensor → Signal Processor → Computer

Figure B.1. Elements of a measurement system.

Vibration sensor

Vibration sensors are also called seismic sensors, seismometers or geophones. In literature, the terms "seismic" and "geophone" are generally used in geophysics-related articles. In this work,

the term vibration is preferred to prevent possible misunderstandings. We employ the vibration sensor with the aim of detecting vibration on machines. The sensor converts vibrations into electrical signals depending on the intensity of the vibration waves in the axis of the vibration sensor. Vibration sensors can be categorized into two groups based on the number of their axes: one-axis and three-axes sensor types. A three-axis vibration sensor is used in this work for the analysis.

In this work, LIS3DH vibration sensor, which is manufactured by STMicroelectronics [174,175] is used for demonstration. The LIS3DH is an ultra-low-power, high performance three-axis linear accelerometer belonging to the "nano" family. The length, width, and thickness of the LIS3DH vibration sensor are 3 mm, 3 mm, and 1 mm, respectively. The LIS3DH has dynamically user-selectable full scales of $\pm2g/\pm4g/\pm8g/\pm16g$, and is capable of measuring accelerations with output data rates from 1 Hz to 5 kHz.

Signal processing unit

A microcontroller is a well-known device to store, compare, and select data. Microcontroller programs usually integrate with other software to perform signal analysis. However, integrating different software for capturing signals and performing signal analysis is quite complex. Therefore, microcontroller programming is not used in the current study. This study is intended to develop a system that has the capability to collect acceleration signals generated by a MEMS accelerometer while simultaneously analyzing the sensed signals.

In the case of a condition monitoring system with online data collection, indication an analysis of the machinery faults often requires manual in-house calculations to be embedded into the system, as well as analysis tools that run in separate computers at the management level. High frequency data of electric, magnetic, or mechanic quantities must be calculated locally in order to avoid the need for a high capacity field bus at the device level. Many complicated tasks can be performed in embedded systems such as transformation to the frequency domain, adaptive filtering, or fuzzy reasoning [168-170]. On the other hand, indications of certain faults are reliable only with very complicated analysis, or when the results are compared to previous results throughout a long period of time. The devices used in control and protection of the machines and drives include a very different number and quality of measurements, data processing capacity and communications capacity.

Graphical user interface (GUI) unit

Available commercial measurement systems usually develop their own embedded platforms and language programming. In this research work, in order to perform signal analysis, especially for vibration-based monitoring, many researchers have used well-known software such as MATLAB. MATLAB offers an intuitive language and flexible environment for technical computations, which integrates mathematical computing and visualization tools for data analysis, and development of algorithms and applications. However, one crucial disadvantage of MATLAB is that the GUI needs to be programmed, but simulations are simply too complex and time consuming to be programmed in MATLAB. Furthermore, MATLAB provides relatively poor performance in terms of interfacing hardware and software. Therefore, current work tries to increase the graphic resolution, while at the same time to have at least the same performance as other software in signal processing, which definitely eases the procedure for interfacing between hardware and software. Therefore, a prototype-customized program is used instead of MATLAB, since it can overcome several disadvantages mentioned above.

B.3. GUI System Design

According to the design and/or customers' requirements in designing a proper reliable sensor, vibration-based sensor systems can contain different equipment/components, which may have various advantages and disadvantages. For a multi-sensor-based smart vibration sensor application, the system designer should meticulously take into account the characteristics of these individual components. The design and its corresponding GUI software are discussed in detail in the next sections.

Prototyping platform

The prototyping platform is developed to operate with Microsoft® Windows platforms. Most of the hardware and software are open-source for Windows prototyping platforms. There are several Windows boards available for different purposes. One of the modest ones is the STEVAL-MKI109V2 board, which has been modernized by STMicroelectronics [174]. The STEVAL-MKI109V2 (eMotion) is a motherboard designed to provide the user with a complete, ready-to-use platform for the demonstration of MEMS devices mounted on adapter boards. The STEVAL-MKI109V2 uses an STM32F103RET6 microcontroller, which functions as a bridge

between the sensor on the adapter board and the computer (i.e. PC), on which it is possible to use customized applications. Analog signals of the vibration sensor are digitized with 8-bit resolution using the board. Next, all algorithms are implemented on the board without a personal computer. The overall system is implemented as a stand-alone project quite easily, thanks to the chip prototyping platform.

The developed GUI provides a user-friendly interface outlining the main characteristics of the MEMS vibration sensor. It allows for easy setup of the sensors as well as the complete configuration of all the registers and advance features embedded in the digital output device. The GUI software provides a visualization of the outputs of the sensor(s) in both graphical and numeric formats, and it allows the user to save data and related figures. The next section describes the functions of the GUI. The GUI software is designed to operate with Microsoft® Windows platforms and is written with Microsoft® Visual Studio 2010. The GUI is a Windows form application written in C# (.NET Framework 4.0) and designed for the operation of the prototype board described previously, or for the STWVAL-MKI105V1 for LIS3DH 3-axes digital accelerometer [174,175].

GUI analysis

To perform vibration-based analysis using the GUI software, users require knowledge about the operating conditions and the parameters of interest, which will help to visualize the results effectively. Generally speaking, in the frequency domain analysis (i.e., using FT-based analysis), the highest peak and its corresponding frequency are investigated for condition related signature(s). If this frequency matches any of the characteristics of any of the faults discussed in Chapter 1, then the peak will most likely correspond to the energy of a defect impulse displayed in the frequency spectra.

In the following pages, example of the proposed GUI and its function are given. Figure B.2 shows launched executable file that can be provided with a sensor package. Figures B.3 and B.4 show the different tabs and their prospective controls that are designed to perform a specific task.

Figure B.3 shows three tab controls that are designed to perform the following main functions in the GUI:

❖ "Operating Parameters" - connects and disconnects the board. It is also used to set the different operating parameters for the vibration sensor. The continuous data can be also displayed in this window.

❖ "Preparatory Testing" - displays the samples plot for the vibration signal. It is also used to display the main statistical measurements of the sampled data.

❖ "Essential Examination" - its main function is to display the FFT plot of the data.

Operating Parameters tab (Figure B.2) are employed as follows:

1. Select the appropriate kit name. In this case, use MKI105V1 (LIS3DH in this work) then select the communication (COM) port currently used from the list.

2. Click "Connect". This action will turn ON the LED light to confirm connection to the board. It is now possible to use the GUI.

3. Select the type of parameter of interest to measure (for this work, the acceleration measurements are used in this work.

4. Choose one of the operating modes previously set by the designer. These modes include the sampling frequency, acceleration scale (in g values), highpass filter parameter, the range of frequency to display on the FFT plot, and the cutoff frequency of the lowpass filter.

5. Click "Start" to receive the data continuously. This action will turn ON the LED light to confirm the data reading function. The continuous data being read is displayed for each axis. To stop data streaming, click on the "Stop" button. This button must be pressed in order to perform further analyses on the collected data.

6. In order to save the data, click the "Save Table" button. This function saves the data of all three axes of the vibration sensor.

7. To disconnect the board, click the "Disconnect" button. This will turn OFF the corresponding LED light. The user can also power down the board by clicking the "Power Down" button.
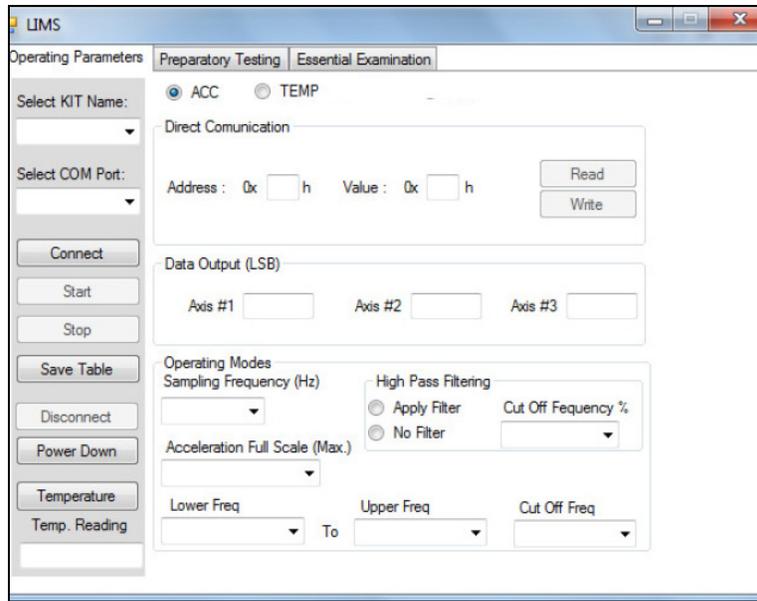
Figure B.2. Developed graphical user interface: main window.

Preparatory Testing tab (Figure B.3) employed as follows:

After the data is collected, the functions within this window help the user visualize the collected data in terms of samples collected; statistical measurements of the collected data can be also displayed. The functionality of this tab control is described as follows:

1. To load the data plot onto the screen, click the "Load Chart" button; the graph is then plotted in the window. Users have the option to save the chart by clicking the "Save Chart" button, or to clear the chart plot from the screen by clicking the "Clear Chart" button.

2. Statistical measurements for the kurtosis, skewness, standard deviation (std), and mean for the data collected are all calculated and displayed for the user to verify if the collected data are within certain predetermined values. This can be performed after the user clicks the "Run Stats" button. Users then have the option of saving the chart by clicking the "Save Chart" button, or clearing the displayed measurement by clicking the "Clear Stats" button.
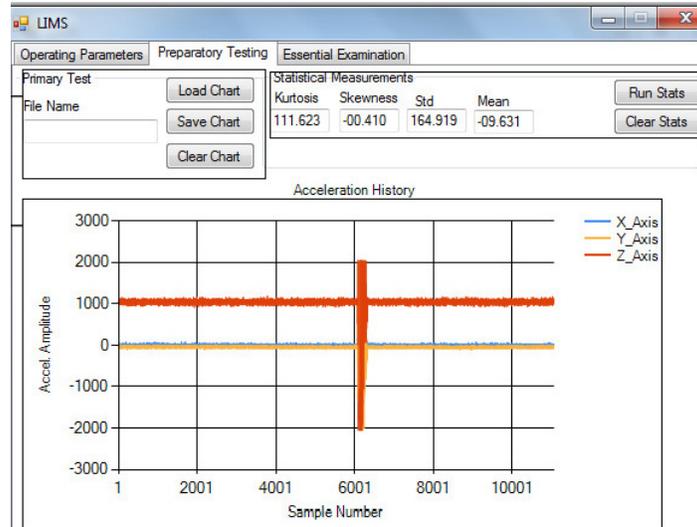
Figure B.3. Preparatory testing window.

Essential Examination tab (Figure B.4) procedure:

Finally, after the collected data is verified for further analysis, the functions within this tab control will allow the user to perform and plot the fast FT (FFT).

1. First, to perform FFT on the collected data, the "FFT" button must be clicked. Then to plot the results, the "Plot FFT" button must be clicked. Users have the option to clear the plot area by clicking the "Clear Chart" button to use the plot area for new data.

2. The FFT plot of all three axes and their corresponding lowpass filtered results are displayed together. An example of sample FFT plot is displayed in Figure B.4.
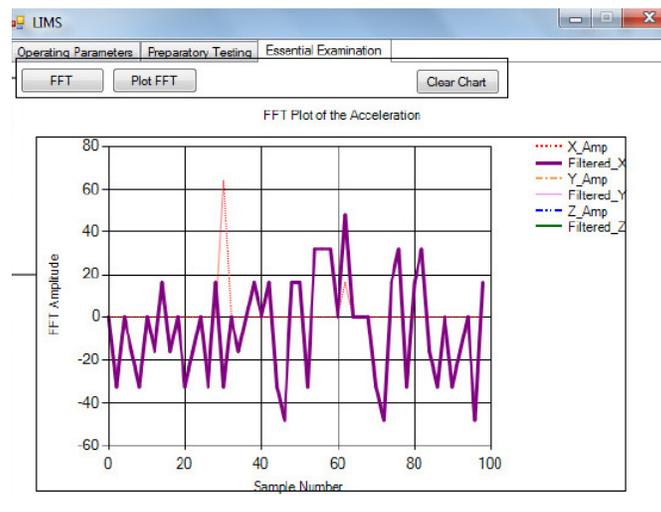
Figure B.4. Examination of the data using FFT plot.

113

B.4. Concluding Remarks

By using an MEMS accelerometer, which is low-cost, lightweight, compact, and low in power consumption, a GUI tool is developed for smart vibration-based sensing for machinery fault detection. With the development of vibration sensors, sensor applications have been used in many aspects of day-to-day life. This document focuses on the application of vibration sensors in rotary machinery, especially for plant development. With the help of the sensor, individuals could monitor various equipment components from a control room. This project is based on an emerged vibration sensor device named LIS3DH, developed by STMicroelectronics Company. In the final system, the board uses the corresponding sensor to collect data, which enables GUI users/operators to visualize the condition of the machine being monitored. The GUI stores the data in a local database or in local files. The designed system can also update the received data to a specific server in real-time. To realize the final product, many factors should be considered when designing the sensor to satisfy the requirements for a robust monitoring system as discussed throughout this work, but also not limited to USB modules, utility modules, real-time clock modules, accelerometer modules, etc. Future works can explore the deployment of temperature, current, and/or acoustic measurements. The automatic fault analysis (especially in the case of cyclic faults) is possible. Yet, much research must be carried out before such a system is reliable enough for the practical use.

References

[1] Machinery gearbox photograph. http://www.trapeziumengineering.com/2014/10/23/planetary-gear-box. (Retrieved October 27, 2017).

[2] P. Donnell, C. Heising, C. Singh, S. Wells, Report of large motor reliability survey of industrial and commercial installations, IEEE Transactions on Industry Applications, 23(1), 1987, 153-158.

[3] A.M. Al-Ghamd, D. Mba, A comparative experimental study on the use of acoustic emission and vibration analysis for bearing defect identification and estimation of defect size, Mechanical systems and signal processing. 20(7), 2006, 1537-71.

[4] Y. Lei, J. Lin, M.J. Zuo, and Z. He, Condition monitoring and fault diagnosis of planetary gearboxes: a review, Measurement, 48, 2014, 292-305

[5] C. Chen and C. Mo, Method for Intelligent Fault Diagnosis of Rotating Machinery, Digital Signal Processing, 14, 2004, 203–217.

[6] Z. Feng M. Liang, and F. Chu, Recent advances in time-frequency analysis methods for machinery fault diagnosis: a review with application examples, Mechanical Systems and Signal Processing, 38(1), 2013, 165-205.

[7] T. Akagaki, M. Nakamura, T. Monzen, and M. Kawabata, Analysis of the behavior of rolling bearings in contaminated oil using some condition monitoring techniques, Journal of Tribology Engineering, 220(5), 2006, 447-453.

[8] A. Jardine, D. Lin, and D. Banjevic, A review on machinery diagnostics and prognostics implementing condition-based maintenance, Mechanical Systems and Signal Processing, 20, 2006, 1483-1510.

[9] N. Baydar, A. Ball, A comparative study of acoustic and vibration signals in detection of gear failures using Wigner–Ville distribution, Mechanical systems and signal processing, 15, 2001, 1091–1107.

[10] P.D. Samuel and D.J. Pines, A review of vibration-based techniques for helicopter transmission diagnostics, Journal of Sound and Vibration, 282, 2005, 475–508.

[11] Li Zhixiong, Y. Jiang, C. Hu, and Z. Peng, Recent progress on decoupling diagnosis of hybrid failures in gear transmission systems using vibration sensor signal: A review, Measurement, 90, 2016, 4-19.

[12] J. McNames, Fourier series analysis of epicyclic gearbox vibration, Journal of Vibration and Acoustics, 124, 2001, 150–152.

[13] P. McFadden, Detecting fatigue cracks in gears by amplitude and phase demodulation of the meshing vibration, Journal of Vibration Acoustics Stress and Reliability in Design-Transactions of the ASME 108, 1986, 165–170.

[14] P. McFadden, Interpolation techniques for time-domain averaging of gear vibration, Mechanical Systems and Signal Processing, 3, 1989, 87–97.

[15] Broken gear tooth defect. http://www.bmbikes.co.uk/photos/museumphotos/Gear.jpg. (Retrieved October 28, 2017).

[16] Pitting defect in gears. http://marinersrepository.blogspot.ca/p/gear-wear-and-failures.html. (Retrieved October 22, 2017).

[17] Scoring defect in gears. http://media.noria.com/sites/archive_images/Backup_200101_Gear5.jpg. (Retrieved October 27, 2017).

[18] A. Aherwar, M. Khalid, Vibration analysis techniques for gearbox diagnostic: A review, International Journal of Advanced Engineering Technology, 3, 2012, 4–12.

[19] H. Endo and R.B. Randall, Enhancement of autoregressive model based gear tooth fault detection technique by the use of minimum entropy deconvolution filter, Mechanical Systems and Signal Processing, 21, 2007, 906-919.

[20] E. Bechhoefer and M. Kingsley, A review of time synchronous average algorithms, Annual Conference of the Prognostics and Health Management Society, San Diego, CA, 2009, 24-33.

[21] P.D. McFadden and M.M. Toozhy, Application of synchronous averaging to vibration monitoring of rolling element bearings, Mechanical Systems and Signal Processing, 14, 2000, 891-906.

[22] Y. Zhan, C. Mechefske, Robust detection of gearbox deterioration using compromised autoregressive modeling and Kolmogorov-Smirnov test statistic-Part I: Compromised autoregressive modeling with the aid of hypothesis tests and simulation analysis, Mechanical Systems and Signal Processing, 21, 2007, 1953–1982.

[23] L. Chen, M. Viliam, Application of vector time series modeling and T-squared control chart to detect early gearbox deterioration, International Journal of Performability Engineering, 10, 2014, 105–114.

[24] F. Elasha, C. Ruiz-Carcel, D. Mba, and P. Chandra, A Comparative Study of the Effectiveness of Adaptive Filter Algorithms, Spectral Kurtosis and Linear Prediction in Detection of a Naturally Degraded Bearing in a Gearbox, Journal of Failure Analysis and Prevention, 14(5), 2014, 623-636.

[25] Gear mesh frequencies and its harmonics. http://www.maintenanceonline.co.uk/maintenanceonline/content_images/Page%2046%20fig%205.jpg. Retrieved October 27, 2017).

[26] Q. Miao, D. Wang, and H. Huang, Identification of characteristic component in frequency domain from signal singularities, Review of Scientific Instruments, 81, 2010, 1-7.

[27] R. Jiang, J. Chen, G. Dong, T. Liu, W. Xiao, The weak fault diagnosis and condition monitoring of rolling element bearing using minimum entropy deconvolution and envelope spectrum, Proceedings of the Institution of Mechanical Engineers, Part C: Journal of Mechanical Engineering Science, 227, 2013, 1116–1129.

[28] W.J. Staszewski, K. Worden, and G.R. Tomlinson, Time-Frequency Analysis in Gearbox Fault Detection Using the Winger-Ville Distribution and Patter Recognition, Mechanical System and Signal Processing, 5, 1997, 673-692.

[29] S. Hussain, H. Gabbar, Fault diagnosis in gearbox using adaptive Wavelet filtering and shock response spectrum features extraction, Structural Health Monitoring, 12, 2013, 169–180.

[30] Y. Li, R. Shao, J. Cao, A new and effective method of gear fault diagnosis using Wavelet packet transform combined with support vector machine, Journal of Northwestern Polytechnical University, 28, 2010) 530–535.

[31] N. Saravanan and K.I. Ramachandran, Incipient gearbox fault diagnosis using discrete Wavelet transform (DWT) for feature extraction and classification using artificial neural network (ANN), Expert Systems with Applications, 37(6), 2010, 4168-4181.

[32] Y. Lei and M.J. Zuo, Fault diagnosis of rotating machinery using an improved HHT based on EEMD and sensitive IMFs, Measurement Science and Technology, 20(12), 2009, 125701.

[33] Y. Yang, Y. He, J. Cheng, D. Yu, A gear fault diagnosis using Hilbert spectrum based on MODWPT and a comparison with EMD approach, Measurement, 42, 2009, 542–551.

[34] Shaft imbalanced forces defect. https://www.ctemag.com/sites/www.ctemag.com/files/article_images/10066.png. (Retrieved October 26, 2017).

[35] P. Pennacchi, N. Bachschmid, and A. Vania, A Model-Based Identification Method of Transverse Cracks in Rotating Shafts Suitable for Industrial Machines, Mechanical Systems and Signal Processing, 20 , 2006, 2112–2147.

[36] G.D. Gounaris and C.A. Papadopoulos, Crack Identification in Rotating Shafts by Coupled Response Measurements, Engineering Fracture Mechanics, 69, 2002, 339–352.

[37] Shaft defects. https://media.licdn.com/mpr/mpr. (Retrieved October 24, 2017).

[38] P.D. McFadden, Detecting fatigue cracks in gears by amplitude and phase demodulation of the meshing vibration, Journal of Vibration, Acoustics, Stress, and Reliability in Design, 108, 1986, 165–170.

[39] H. Hashemian, State-of-the-art predictive maintenance techniques, IEEE Transactions on Instrumentation and Measurements, 60, 2011, 226–236.

[40] Shaft defect frequency response. Alignment Training Course PPT Presentation and Machine. http://www.lifetime-reliability.com (Retrieved November 24, 2016).

[41] R.B. Randall and Antoni, Rolling element bearing diagnostics—a tutorial. Mechanical Systems and Signal Processing, 25(2), 2011, 485-520.

[42] A. Choudhury and N. Tandon, Vibration response of ball bearings in a rotor bearing system to a local defect under radial load, Tribology, 128, 2006, 252-261.

[43] F. Cong, J. Chen, G. Dong, and M. Pecht, Vibration model of rolling element bearings in a rotor-bearing system for fault diagnosis, Journal of Sound and Vibration, 332(8), 2013, 2081-2097.

[44] Rolling element bearing picture. http://en.wikipedia.org/wiki/Rollingelementbearing. (Retrieved October 21, 2014).

[45] N. Tandon, A comparison of some vibration parameters for the condition monitoring of rolling element bearings, Measurement, 12, 1994, 285-289.

[46] R.B. Randall, J. Antoni, and S. Chobsaard, The relationship between Spectral Correlation and Envelope Analysis in the Diagnostics of Bearing Faults and Other Cyclostationary Machine Signals, Mechanical Systems and Signal Processing, 15, 2001, 945-962.

[47] P. Borghesani, P. Pennacchi, S. Chatterton, The relationship between kurtosis and envelope-based indexes for the diagnostic of rolling element bearings, Mechanical Systems and Signal Processing, 43(1–2), 2014, 25–43.

[48] Geometry of as typical ball bearing. http://ars.els-cdn.com/content/image/1-2.0S0094114X06000516gr1.jpg. (Retrieved December 21, 2014).

[49] P. Borghesani, P. Pennacchi, R.B. Randall, N. Sawalhib, and R. Riccia, Application of cepstrum pre-whitening for the diagnosis of bearing faults under variable speed conditions, Mechanical Systems and Signal Processing, 36(2), 2013, 370–384.

[50] D. Ho and R.B. Randall, Optimization of Bearing Diagnostic Techniques using Simulated and Actual Bearing Fault Signals, Mechanical Systems and Signal Processing, 14, 2000, 763 -788.

[51] M. Timusk, M. Lipsett, and C.K. Mechefske, Fault detection using transient machine signals. Mechanical Systems and Signal Processing, 22(7), 2008, 1724-1749.

[52] H. Gao, L. Liang, X. Chen, and G. Xu, Feature extraction and recognition for rolling element bearing fault utilizing short-time Fourier transform and non-negative matrix factorization, Chinese Journal of Mechanical Engineering, 28(1), 2015, 96-105.

[53] M. Cocconcelli, R. Zimroz, R. Rubini, and W. Bartelmus, Kurtosis over Energy Distribution Approach for STFT Enhancement in Ball Bearing Diagnostics, Condition Monitoring of Machinery in Non-Stationary Operations, 2012, 51-59.

[54] Y. Zhou, J. Chen, G.M. Dong, W.B. Xiao, and Z.Y. Wang, Wigner–Ville distribution based on cyclic spectral density and the application in rolling element bearings diagnosis, Institution of Mechanical Engineers ,Journal of Mechanical Engineering Science, 225 (C), 2011, 2831-2847.

[55] Z.K. Peng and F.L. Chu, Application of the Wavelet transform in machine condition monitoring and fault diagnostics: a review with bibliography, Mechanical Systems and Signal Processing, 18(2), 2004, 199-221.

[56] J. Liu, W. Wang, and F. Ma, Bearing system health condition monitoring using a Wavelet cross-spectrum analysis technique, Journal of Vibration and Control, 18(7), 2011, 953–963.

[57] X.F. Fan and M.J. Zuo, Machine fault feature extraction based on intrinsic mode functions, Measurement Science and Technology, 19, 2008, 1–12.

[58] L. Qu and F. Wu, An improved method for restraining the end effect in empirical mode decomposition and its applications to the fault diagnosis of large rotating machinery, Journal of Sound and Vibration, 314, 2008, 586-602.

[59] R. Yan and R.X. Gao, Hilbert-Huang Transform-Based Vibration Signal Analysis for Machine Health Monitoring, IEEE Transaction on Instrumentation and Measurement, 55(6), 2006, 2320-2329.

[60] V.K. Rai and A.R. Mohanty, Bearing fault diagnosis using FFT of intrinsic mode functions in Hilbert–Huang transform, Mechanical Systems and Signal Processing, 21(6), 2007, 2607–2615.

[61] Z.K. Peng, P.W. Tse, and F.L. Chu, A comparison study of improved Hilbert–Huang transform and Wavelet transform: application to fault diagnosis for rolling bearing, Mechanical Systems and Signal Processing, 19, 2005, 974–988.

[62] Y. Yang, D. Yu, and J. Cheng, A fault diagnosis approach for roller bearing based on IMF envelope spectrum and SVM, Measurement, 40, 2007, 943-350.

[63] S. Osman and W. Wang, A normalized Hilbert-Huang transform technique for bearing fault detection, Journal of Vibration and Control, 22(11), 272014, 71-2787.

[64] S. Osman and W. Wang, An enhanced Hilbert-Huang transform technique for bearing condition monitoring, Measurement Science and Technology, 24(8), 2013, 1-13.

[65] J. Antoni and R.B. Randall, Unsupervised noise cancellation for vibration signals: part I—evaluation of adaptive algorithms, Mechanical Systems and Signal Processing, 18(1), 2004, 89-101.

[66] J. Antoni and R.B. Randall, Unsupervised noise cancellation for vibration signals: part II—a novel frequency-domain algorithm, Mechanical Systems and Signal Processing, 18(1), 2004, 103-117.

[67] D. Abboud, J. Antoni, S. Sieg-Zieba, and M. Eltabach, Deterministic-random separation in non-stationary regime, Journal of Sound and Vibration, 362, 2016, 305-326.

[68] J. McBain and M. Timusk, Fault detection in variable speed machinery: Statistical parameterization, Journal of Sound and Vibration, 327(3), 2009, 623-646.

[69] W. Bartelmus and R. Zimroz, A new feature for monitoring the condition of gearboxes in non-stationary operating conditions, Mechanical Systems and Signal Processing, 23(5), 2009, 1528-1534.

[70] J. Antoni and R.B. Randall, Differential diagnosis of gear and bearing faults, Transactions-American Society of Mechanical Engineers Journal of Vibrations and Acoustics, 124(2), 2002, 165-171.

[71] P. Borghesani, R. Ricci, S. Chatterton, and P. Pennacchi, A new procedure for using envelope analysis for rolling element bearing diagnostics in variable operating conditions, Mechanical Systems and Signal Processing, 38(1), 2013, 23-35.

[72] D. Abboud, J. Antoni, S. Sieg-Zieba, and M. Eltabach, Envelope analysis of rotating machine vibrations in variable speed conditions: a comprehensive treatment, Mechanical Systems and Signal Processing, 84, 2017, 200-226.

[73] A.P. Ompusunggu, Automated cepstral editing procedure (ACEP) as a signal pre-processing in vibration-based bearing fault diagnostics, International Conference of Surveillance, 8, 2015, 1-11.

[74] P. Borghesani, P. Pennacchi, R.B. Randall, N. Sawalhi, and R. Ricci, Application of cepstrum pre-whitening for the diagnosis of bearing faults under variable speed conditions, Mechanical Systems and Signal Processing, 36(2), 2013, 370-384.

[75] C. Peeters, P. Guillaume, and J. Helsen, A comparison of cepstral editing methods as signal pre-processing techniques for vibration-based bearing fault detection, Mechanical Systems and Signal Processing, 91, 2017, 354-381.

[76] J. Antoni, Fast computation of the kurtogram for the detection of transient faults, Mechanical Systems and Signal Processing, 21(1), 2007, 108-124.

[77] L. Saidi, J.B. Ali, E. Bechhoefer, and M. Benbouzid, Wind turbine high-speed shaft bearings health prognosis through a spectral Kurtosis-derived indices and SVR, Applied Acoustics, 120, 2017, 1-8.

[78] J. Tian, C. Morillo, M.H. Azarian, and M. Pecht, Motor bearing fault detection using spectral kurtosis-based feature extraction coupled with K-nearest neighbor distance analysis, IEEE Transactions on Industrial Electronics, 63(3), 2016, 1793-1803.

[79] R. Li, D. Yu, X. Chen, J. Liu, A compound fault diagnosis method for gearboxes based on chirplet path pursuit and EEMD, Journal of Vibration and Shock, 33, 2014, 51–56.

[80] Y. Lei, Z. He, Y. Zi, EEMD method and WNN for fault diagnosis of locomotive roller bearings, Expert Systems with Applications, 38, 2011, 7334–7341.

[81] J. Wang, R. Gao, R. Yan, Integration of EEMD and ICA for wind turbine gearbox diagnosis, Wind Energy, 17, 2014, 757– 773.

[82] J. Chen, J. Pan, Z. Li, Y. Zi, and X. Chen, Generator bearing fault diagnosis for wind turbine via empirical Wavelet transform using measured vibration signals, Renewable Energy, 89, 2016, 80-92.

[83] C. Wang, M. Gan, C.A. and Zhu, Intelligent fault diagnosis of rolling element bearings using sparse Wavelet energy based on overcomplete DWT and basis pursuit, Journal of Intelligent Manufacturing, 28, 2017, 1377-1391.

[84] Y. Qin, J. Xin, Y. and Mao, Weak transient fault feature extraction based on an optimized Morlet Wavelet and kurtosis, Measurement Science and Technology, 27(8), 2016, p.085003.

[85] Y. Wang, R. Markert, J. Xiang, and W. Zheng, Research on variational mode decomposition and its application in detecting rub-impact fault of the rotor system, Mechanical Systems and Signal Processing, 60, 2015, 243-251.

[86] S. Zhang, Y. Wang, S. He, and Z. Jiang, Bearing fault diagnosis based on variational mode decomposition and total variation denoising, Measurement Science and Technology, 27(7), 2016, p.075101.

[87] Z.K. Zhu, R. Yan, L. Luo, Z.H. Feng, and F.R. Kong, Detection of signal transients based on Wavelet and statistics for machine fault diagnosis, Mechanical Systems and Signal Processing, 23(4), 2009, 1076-1097.

[88] Y. Wang, Z. He, and Y. Zi, Enhancement of signal denoising and multiple fault signatures detecting in rotating machinery using dual-tree complex Wavelet transform, Mechanical Systems and Signal Processing, 24(1), 2010, 119-137.

[89] I. Bayram and I.W. Selesnick, Frequency-domain design of overcomplete rational-dilation Wavelet transforms, IEEE Transactions on Signal Processing, 57(8), 2009, 2957-2972.

[90] I.W. Selesnick, Resonance-based signal decomposition: A new sparsity-enabled signal analysis method, Signal Processing, 91(12), 2011, 2793-2809.

[91] I.W. Selesnick, Wavelet transform with tunable Q-factor, IEEE transactions on signal processing, 59(8), 2011, 3560-3575.

[92] W. Huang, H. Sun, and W. Wang, Resonance-Based Sparse Signal Decomposition and its Application in Mechanical Fault Diagnosis: A Review, Sensors, 17, 2017, p.1279.

[93] W. He, Y. Zi, B. Chen, S. Wang, and Z. He, Tunable Q-factor Wavelet transform denoising with neighboring coefficients and its application to rotating machinery fault diagnosis, Science China Technological Sciences, 56(8), 2013, 1956-1965.

[94] J. Luo, D. Yu, and M. Liang, A kurtosis-guided adaptive demodulation technique for bearing fault detection based on tunable-Q Wavelet transform, Measurement Science and Technology, 24(5), 2013, p.055009.

[95] D. Zhang, D. Yu, and W. Zhang, Energy operator demodulating of optimal resonance components for the compound faults diagnosis of gearboxes, Measurement Science and Technology, 26(11), 2015, p.115003.

[96] H. Wang, J. Chen, and G. Dong, Feature extraction of rolling bearing's early weak fault based on EEMD and tunable Q-factor Wavelet transform, Mechanical Systems and Signal Processing, 48(1), 2014, 103-119.

[97] D. Zhang and D. Yu, Multi-fault diagnosis of gearbox based on resonance-based signal sparse decomposition and comb filter, Measurement, 103, 2017, 361-369.

[98] N. Sawalhi, R.B. Randall, and H. Endo, The enhancement of fault detection and diagnosis in rolling element bearings using minimum entropy deconvolution combined with spectral kurtosis, Mechanical Systems and Signal Processing, 21, 2007, 2616-2633.

[99] W. Sui, S. Osman and W. Wang, An adaptive envelope spectrum technique for bearing fault detection, Measurement Science and Technology, 25(9), 2014, (095004).

[100] P. Maragos and W. Schafer, Morphological filters—Part 1: Their set-theoretic analysis and relations to linear shift-invariant filters, IEEE Transactions on Acoustics, Speech and Signal Processing, 35(8), 1987, 1153–1169.

[101] G. Matheron and J. Serra, The birth of mathematical morphology, Proceedings of VIth International Symposium on Mathematical Morphology, 2002, 1-16.

[102] J. Wang, G. Xu, Q. Zhang, and L. Liang, Application of improved morphological filter to the extraction of impulsive attenuation signals, Mechanical Systems and Signal Processing, 23(1), 2009, 236–245.

[103] L. Zhang, J. Xu, J. Yang, D. Yang, and D. Wang, Multiscale morphology analysis and its application to fault diagnosis, Mechanical Systems and Signal Processing, 22(3), 2008, 597–610.

[104] C. Li, M. Liang, Y. Zhang, and S. Hou, Multi-scale autocorrelation via morphological Wavelet slices for rolling element bearing fault diagnosis, Mechanical Systems and Signal Processing, 31, 2012, 428–446.

[105] B. Li, P.L. Zhang, Z.J. Wang, S.S. Mi, and Y.T. Zhang, Gear fault detection using multi-scale morphological filters, Measurement, 44(10), 2011, 2078-2089.

[106] J. Wang, G. Xu, Q. Zhang, and L. Liang, Application of improved morphological filter to the extraction of impulsive attenuation signals, Mechanical System and Signal Processing, 23(1), 2009, 236–245.

[107] P. Zhang, B. Li, S. Mi, Y. Zhang, D. Liu, Bearing fault detection using multi-scale fractal dimensions based on morphological covers, Shock and Vibration, 19, 2012, 1373–1383.

[108] B. Li, P.L. Zhang, S.S. Mi, Y.T. Zhang, and D. S. Liu, Multi-scale fractal dimension based on morphological covering for gear fault diagnosis, Proceedings of Institution of Mechanical Engineers, Journal of Mechanical Engineering Science, Part C, 2011, 1-8.

[109] Q. Chen, Z. Chen, W. Sun, G. Yang, A. Palazoglu, Z. Ren, A new structuring element for multi-scale morphology analysis and its application in rolling element bearing fault diagnosis, Journal of Vibration and Control, 2013, 1–25.

[110] S. Dong, B. Tang, and Y. Zhang, A repeated single-channel mechanical signal blind separation method based on morphological filtering and singular value decomposition, Measurement, 45, 2012, 2052–2063.

[111] V.N. Patel, N. Tandon, and R.K. Pandey, Improving defect detection of rolling element bearings in the presence of external vibrations using adaptive noise cancellation and multiscale morphology, Proceedings of Institution of Mechanical Engineers, Journal of Engineering Tribology, Part J, 2011, 150-162.

[112] L. Meng, J. Xiang, Y. Wang, Y. Jiang, and H. Gao, A hybrid fault diagnosis method using morphological filter–translation invariant Wavelet and improved ensemble empirical mode decomposition, Mechanical Systems and Signal Processing, 50(51), 2015, 101–115.

[113] Z. Chen, N. Gao, W. Sun, Q. Chen, and F. Yan, X. Zhang, M. Iftikhar, S. Liu, and Z. Ren, A Signal-Based Triangular Structuring Element for Mathematical Morphological Analysis and Its Application in Rolling Element Bearing Fault Diagnosis, Shock and Vibration, 2014, 1-16.

[114] A. Hu and L. Xiang, Selection principle of mathematical morphological operators in vibration signal processing, Journal of Vibration and Control, 2014, 1–12.

[115] Y. Dong, M. Liao, X. Zhang, F. Wang, Fault diagnosis of rolling element bearings based on modified morphological method, Mechanical System and Signal Processing, 25(4), 2011, 1276–1286.

[116] D. Wang, P.W. Tse, and Y.L. Tse, A morphogram with the optimal selection of parameters used in morphological analysis for enhancing the ability in bearing fault diagnosis, Measurement Science and Technology, 23, 2012, 1-15.

[117] N. Murali, Early classification of bearing faults using morphological operators and fuzzy inference, IEEE Transaction on Industrial Electronics, 60 (2), 2013, 567-574.

[118] A. Renyi, On measures of information and entropy, Proceedings of the 4th Berkeley Symposium on Mathematics, Statistics and Probability, 1961, 547–561.

[119] A.G.E. Bashkirov, Renyi entropy as a statistical entropy for complex systems, Theoretical and Mathematical Physics, 149(2), 2006, 1559-1573.

[120] Y. Lei, J. Lin, Z. He, and M.J. Zuo, A review on empirical mode decomposition in fault diagnosis of rotating machinery, Mechanical Systems and Signal Processing, 35, 2013, 108–126.

[121] D. Mandic, N. Rehman, Z. Wu, N. Huang, Empirical mode decomposition based time-frequency analysis of multivariate signals, IEEE Signal Processing Magazine, 30, 2013, 74–86.

[122] Z. Li, Z Peng, A new non-linear blind source separation method with chaos indicators for decoupling diagnosis of hybrid failures: A marine propulsion gearbox case with a large speed variation, Chaos, Solitons and Fractals, 2015, http://dx.doi.org/10.1016/j.chaos.2015.09.023.

[123] Z. Wu and N.E. Huang, Ensemble empirical mode decomposition: A noise-assisted data analysis method, Advances in Adaptive Data Analysis, 1, 2009, 1-49.

[124] A.O. Andrate, P. Kyberd, and S.J. Nasuto, The application of the Hilbert spectrum to the analysis of electromyographic signals, Information Sciences, 9(178), 2008, 2176-2193.

[125] EMD and IMF sifting; showing the upper and lower envelopes and their corresponding mean picture. https://figshare.com/articles/_EMD_8211_IMF_sifting_process_/691485. (Retrieved November 21, 2015).

[126] H. Li, Y. Zhang, and H. Zheng, Hilbert-Huang transform and marginal spectrum for detection and diagnosis of localized defects in roller bearings, Journal of Mechanical Science and Technology, 23, 2009, 291-301.

[127] W.C. Tsao, Y.F. Li, D.D. Le, and M.C. Pan, An insight concept to select appropriate IMFs for envelope analysis of bearing fault diagnosis, Measurement, 45(6), 2012, 1489–1498.

[128] J. Yan and L. Lu, Improved Hilbert–Huang transform-based weak signal detection methodology and its application on incipient fault diagnosis and ECG signal analysis, Signal Processing, 98, 2014, 74–87.

[129] R.B. d'Agostino, A. Belanger, and R.B. d'Agostino Jr., A suggestion for using powerful and informative test of normality, The American Statistician, 44, 1990 316-321.

[130] G. Poitras, Economics Letters 90, 2006, 304–309.

[131] S. Osman and W. Wang, A Morphological HHT technique for bearing fault detection, IEEE Transactions on Instrumentation and Measurement (in press), 2016.

[132] C.M. Jarque and A.K. Bera, A test for normality of observations and regression residuals, International Statistical Review, 55, 1987, 163-172.

[133] T. Thadewald and H. Büning, Jarque–Bera test and its competitors for testing normality–a power comparison, Journal of Applied Statistics, 34(1), 2007, 87-105.

[134] C. Studholme, D.L.G. Hill, and D.J. Hawkes, An overlap invariant entropy measure of 3D medical image alignment, Pattern Recognition, 32, 1999, 71–86.

[135] K.K Ang, Z.Y. Chin, H. Zhang, and C. Guan, Mutual information-based selection of optimal spatial–temporal patterns for single-trial EEG-based BCIs, Pattern Recognition, 45(6), 2012, 2137-2144.

[136] S. Osman and W. Wang, Integrated Hilbert Huang Technique for Bearing Defects Detection, Proceedings of 2016 IEEE International Conference on Prognostics and Health Management, Ottawa, Canada, 2016, 1-6.

[137] Z.P. Feng and M.J. Zuo, Vibration signal models for fault diagnosis of planetary gearboxes, Journal of Vibration and Acoustics, 331, 2012, 4919–4939.

[138] X. Gu and P. Velex, A dynamic model to study the influence of planet position errors in planetary gears, Journal of Sound and Vibration, 331, 2012, 1–20.

[139] W. Bartelmus and R. Zimroz, Vibration condition monitoring of planetary gearbox under varying external load, Mechanical Systems and Signal Processing, 23, 2009, 246–257.

[140] W. Bartelmus and R. Zimroz, A new feature for monitoring the condition of gearboxes in non-stationary operating conditions, Mechanical Systems and Signal Processing, 23, 2009, 1528–1534.

[141] W. D. Mark, H. Lee, R. Patrick, and J.D. Coker, A simple frequency-domain algorithm for early detection of damaged gear teeth, Mechanical Systems and Signal Processing, 24(8), 2010, 2807-2823.

[142] H. Shah and H. Hirani, Online condition monitoring of spur gears, International Journal of Condition Monitoring, 4(1), 2014, 15-22.

[143] R. Zimroz, J. Urbanek, T. Barszcz, W. Bartelmus, F. Millioz, and N. Martin, Measurement of instantaneous shaft speed by advanced vibration signal processing-application to wind turbine gearbox, Metrology and Measurement Systems, 18(4), 2011, 701-712.

[144] N. Baydar, A. Ball, A comparative study of acoustic and vibration signals in detection of gear failures using Wigner–Ville distribution, Mechanical Systems and Signal Processing. 15(6) (2001) 1091–1107.

[145] R. Yan, R.X. Gao, X. Chen, Wavelets for fault diagnosis of rotary machines: a review with applications, Signal Processing, (2013) http://dx.doi.org/10.1016/j. sigpro.2013.1004.1015i.

[146] S. Wang, W. Huang, Z. Zhu, Transient modeling and parameter identification based on Wavelet and correlation filtering for rotating machine fault diagnosis, Mechanical Systems and Signal Processing, 25(4), 2011, 1299–1320.

[147] J. Lin, M. Zuo, Gearbox fault diagnosis using adaptive Wavelet filter, Mechanical Systems and Signal Processing. 17(6), 2003, 1259–1269.

[148] B. Chen, Z. Zhang, C. Sun, B. Li, Y. Zi, Z. He, Fault feature extraction of gearbox by using overcomplete rational dilation discrete Wavelet transform on signals measured from vibration sensors, Mechanical Systems and Signal Processing ,33, 2012, 275–298.

[149] G.F. Bin, J.J. Gao, X.J. Li, Early fault diagnosis of rotating machinery based on Wavelet packets-empirical mode decomposition feature extraction and neural network, Mechanical Systems and Signal Processing, 27, 2012, 696–711.

[150] N. Saravanan, K.I. Ramachandran, Incipient gearbox fault diagnosis using discrete Wavelet transform (DWT) for feature extraction and classification using artificial neural network (ANN), Expert System Application, 37, 2010, 4168–4181.

[151] H. Qiu, L. Jay, J. Lin, G. Yu, Wavelet filter-based weak signature detection method and its application on rolling element bearing prognostics, Journal of Sound and Vibration, 289, 2006, 1066–1090.

[152] X. Chen, D. Yu, R. Li, Analysis of gearbox compound fault vibration signal using morphological component analysis, Journal of Mechanical Engineering, 50, 2014, 108–115.

[153] X. Chen, D. Yu, R. Li, Compound fault diagnosis method for gearbox based on morphological component analysis and order tracking, Journal of Aerospace Power, 29, 2014, 225–32.

[154] J. Yang, H. Zeng, Z. Guan, Y. Wang, Compound fault diagnosis for gearbox based on kernel morphological component analysis, Journal of Vibration and Shock, 31, 2012, 97–101.

[155] H. Zhang, Z. Du, Z. Fang, S. Wang, X. Chen, Sparse decomposition based aero-engine's bearing fault diagnosis, Journal of Mechanical Engineering, 51, 2015, 97–105.

[156] M.V Afonso, J.M. Bioucas-Dias, and M.A. Figueiredo, Fast image recovery using variable splitting and constrained optimization, IEEE Transactions on Image Processing, 19(9), 2010, 2345-2356.

[157] S.S. Chen, D.L. Donoho, and M.A. Saunders, Atomic decomposition by basis pursuit. SIAM review, 43(1), 2001, 129-159.

[158] M. Elad, J.L. Starck, P. Querre, and D.L Donoho, Simultaneous cartoon and texture image in painting using morphological component analysis (MCA). Applied and Computational Harmonic Analysis, 19(3), 2005, 340-358.

[159] J.Bobin, J.L Starck, J.M. Fadili, Y. Moudden, and D.L. Donoho, Morphological component analysis: An adaptive thresholding strategy. IEEE Transactions on Image Processing, 16(11), 2007, 2675-2681.

[160] A. Beck and M. Teboulle, A fast iterative shrinkage-thresholding algorithm for linear inverse problems. SIAM Journal on imaging sciences, 2(1), 2009. 183-202.

[161] M.V. Afonso, J.M Bioucas-Dias, and M.A. Figueiredo, Fast image recovery using variable splitting and constrained optimization, IEEE Transactions on Image Processing, 19(9), 2010, 2345-2356.

[162] J. Ye, Cosine similarity measures for intuitionistic fuzzy sets and their applications, Mathematical and Computer Modelling, 53(1): 2011, 91-7.

[163] Z. Liu, X. Zhao, M,J. Zuo, H. Xu, Feature selection for fault level diagnosis of planetary gearboxes, Advances in Data Analysis and Classification, 8(4), 2014,377-401.

[164] W. Jiang, Z. Zhang, F. Li, L. Zhang, M. Zhao, X. Jin, Joint label consistent dictionary learning and adaptive label prediction for semisupervised machine fault classification, IEEE Transactions on Industrial Informatics, 12(1), 2016, 248-56.

[165] S. Boyd, N. Parikh, E. Chu, B. Peleato, and J. Eckstein, Distributed optimization and statistical learning via the alternating direction method of multipliers, Foundations and Trends® in Machine Learning, 3(1), 2011, 1-122.

[166] S. Nandi, H.A. Toliyat and X. Li, Condition monitoring and fault diagnosis of electrical motors-a review, IEEE Transactions on Energy Conversion, 20, 2005, 719-729.

[167] A. Mansfield and G.M. Lyons, The use of accelerometry to detect heel contact events for use as a sensor in FES assisted walking, Medical Engineering and Physics, 25, 2003, 879-885.

[168] T. Lindh, J. Ahola, J. Partanen, Communication Possibilities for Remote Control and Condition Monitoring of Small Scale Power Plant, NORDAC 2002, Copenhagen, Denmark, 2002.

[169] E. Kevin Speller and Y. Duli, A low-noise MEMS accelerometer for unattended ground sensor applications, In Proceedings of SPIE, 5417, 2004, 63-72.

[170] R. Bogue, Sensors for condition monitoring: A review of technologies and applications, Sensor Review, 33(4), 2013, 295-299.

[171] M. Tanaka, An industrial and applied review of new MEMS devices features, Microelectronic engineering, 84(5), 2007, 1341-1344.

[172] R. Bogue, MEMS sensors: past, present and future, Sensor Review, 27(1), 2007, 7-13.

[173] W. Wang and O. Jianu, A smart monitor for machinery fault detection, IEEE/ASME Transactions on Mechatronics, 15(1), 2010, 70-78.

[174] STMicroelectronics. UM0979 User manual for STEVAL-MKI109V2: eMotion motherboard for MEMS adapter boards. www.st.com. (Retrieved September 24, 2015).

[175] Schematics presentations of internal structures of vibration sensors. http://newsline.linearcollider.org (Retrieved October 20, 2015).